



ScuDo

Scuola di Dottorato ~ Doctoral School

WHAT YOU ARE, TAKES YOU FAR



A

Doctoral Dissertation

Doctoral Program in Electrical, Electronics and Communications Engineering
(32nd Cycle)

3D printable materials for CO₂ capture and separation technologies

Matteo Gillono

Supervisors

Prof. Candido Fabrizio Pirri

Prof. Maria Elena Tresso

Politecnico di Torino

March 9, 2020

This thesis is licensed under a Creative Commons License, Attribution - Noncommercial - NoDerivative Works 4.0 International: see www.creativecommons.org. The text may be reproduced for non-commercial purposes, provided that credit is given to the original author.

I hereby declare that, the contents and organisation of this dissertation constitute my own original work and does not compromise in any way the rights of third parties, including those relating to the security of personal data.

.....
Matteo Gillono
Turin, March 9, 2020

Summary

The increasing of the anthropogenic CO₂ emissions has brought, in the last century, to an unacceptable climate change due to the rise of the global temperature. The reduction of CO₂ concentration in the atmosphere has become a crucial aspect to contrast the global warming. In this context, different carbon capture (CC) technologies have been developed to directly absorb and separate CO₂ at the source. This thesis describes the study carried out on smart materials able to be processed through DLP 3D printing for CO₂ capture and management. In particular, photo-curable formulations, composed of a photo-crosslinkable monomer and different functional additives, will be described from the preparation to the characterization and application.

The first study describes the work carried out on the preparation of photo-curable resins containing light responsive azo-benzene-based dyes for the control of CO₂ permeability in 3D printed structures. CO₂ Permeability analysis related to light irradiation of membranes containing Poly (ethylene glycol) diacrylate (PEGDA) and two azobenzene dyes, namely Methyl Red (MR) and Disperse Red 1 Methacrylate (DR1M), will be shown. Analysis with oxygen, to evaluate CO₂/O₂ permselectivity, will be also described. Finally, the successful 3D printing of a specific designed device for the control of CO₂ flow by an external laser source will be presented.

The second study aims to investigate the influence of different ionic liquids (ILs) on the printability of photo-curable resins for 3D printing. The goal was to introduce CO₂-philic species (ILs) as additives in liquid formulations and demonstrate the possibility to create solid structures through digital light processing (DLP) technology. The polymerization ability and the comparison of physical and chemical properties of formulations containing PEGDA and ILs with different cations and anions, bearing reactive groups will be presented. Moreover, the successful 3D printing of high complexity structures will be shown.

In the last study, the synthesis of specifically functionalized imidazolium-based ILs able to be integrated in 3D printable photo-curable formulations and absorb CO₂ will be described. Chemical and physical properties of the liquid and photo-cured formulations containing PEGDA and ILs with CO₂-philic anions and cations will be shown. Finally, high pressure CO₂ absorption analysis of the 3D printed structures containing the active ILs will be presented.

Acknowledgment

And I would like to acknowledge all the people I had the privilege to work with and, above all, Dr. Ignazio Roppolo and Dr. Annalisa Chiappone for their help and patience throughout these three years of PhD, without whom this work would not have been possible. Moreover, I would like to thank Anna for her precious support and psychological help during the writing of this thesis.

Contents

List of Tables	5
List of Figures	6
Introduction.....	11
1.1 Global warming: causes, expectations and solutions.....	11
1.2 Carbon capture technology.....	15
1.2.1 Absorption processes	16
1.2.2 Adsorption processes	18
1.2.3 Membrane technology	20
1.2.3.1 Azobenzene compounds	22
1.3 Ionic liquids and poly ionic liquids.....	24
1.3.1 Ionic liquids characteristics.....	25
1.3.2 Ionic liquids and poly ionic liquids for CO ₂ capture.....	27
1.4 3D printing.....	28
1.4.1 Introduction to 3D printing	28
1.4.2 Introduction to photopolymerization	31
1.4.3 Digital light processing technology.....	32
1.4.4 DLP 3D printing with smart dyes.....	33
1.4.5 Ionic liquids and poly ionic liquids in DLP 3D printing	35
1.5 Goals of the research.....	37
CO ₂ permeability control in 3D printed light responsive structures	39
1.1 Introduction	39
1.2 Experimental and methods	40
1.2.1 Materials	40
1.2.2 Formulations and sample preparation.....	41
1.2.3 Material characterization	42
1.3 Results and discussion.....	45

1.3.1 Polymerization study	45
1.3.2 Chemical and physical characterizations	49
1.3.3 Permeability characterization.....	51
1.3.4 3D printed device for pH control	57
1.4 Conclusion.....	59
Study on the printability through DLP technique of ionic liquids for CO ₂ capture	61
1.1 Introduction	61
1.2 Experimental and methods	62
1.2.1 Materials	62
1.2.2 Formulations preparation and characterization	64
1.3 Results and discussion.....	66
1.4 Conclusion.....	73
3D printing of synthesized Poly Ionic Liquids for CO ₂ capture.....	76
1.1 Introduction	76
1.2 Experimental and methods	77
1.2.1 Materials	77
1.2.2 Ionic liquids synthesis.....	78
1.2.3 Formulations and sample fabrications.....	83
1.2.4 Material characterization	85
1.3 Results and discussion.....	86
1.3.1 Ionic liquids and formulations characterization	86
.....	95
1.3.1 Matrix porosity modifications.....	95
1.3.1.1 Long chain poly ionic liquid (PDADMA_TFSI)	95
1.3.1.2 Ionic complexation by multivalent benzoic acid.....	97
1.3.2 3D printing and CO ₂ uptake.....	100
1.4 Conclusion.....	102
1.5 Next steps	103
Ionic liquids' nomenclature.....	104
Conclusion	105
References.....	108
Appendix A.....	124
Appendix B	126
Appendix C	127

Appendix D.....	130
Appendix E	133
Appendix F	136
Appendix G.....	137

List of Tables

Table 1.1 Physical properties: T_m : melting temperature; T_b : boiling temperature; ρ : density; μ : viscosity; P^{sat} : vapor pressure; D : diffusion coefficient; γ_{LV} : interfacial tension of liquid-vapor; κ : conductivity; and C_p : specific heat capacity at constant pressure (153).....	p. 26
Table 2.1 Properties of the membranes containing MR and DR1M azo dye compared to the properties of neat PEGDA (Mw575)	p. 57
Table 3.1 molecular schematics and abbreviations of the ionic liquids used in the formulations.....	p. 63
Table 3.2. Irradiation times (s) for each layer for membranes printing (10 μm) and cubic structures printing (50 μm).....	p. 67
Table 3.3 Ionic liquid content in the samples in relation to the weight variation after solvent treatment.....	p. 68
Table 3.4 Glass transition temperature (T_g) values ($^{\circ}\text{C}$) calculated through DSC and DMTA.....	p. 69
Table 3.5 Calculated diffusivity (D), solubility (S) and permeability (P) values for 3D printed membranes containing different ionic liquids.	p. 71
Table 3.6 Weight percentage increase of samples exposed to CO_2 atmosphere at 1bar and 3bar.....	p. 73
Table 4.1 list of synthesized ionic liquids with molecular structure and abbreviations.....	p. 82

List of Figures

- Figure 1.1** Historical trend of world sectorial CO₂ emissions in billion tons from 1971 to 2011 (7)..... p. 11
- Figure 1.2** Global mean surface temperature (GMST). Historical values for the period 1850–2005 (gray lines), and RCP2.6 (orange lines) and RCP4.5 (red lines) simulation for the period 2006–2099. The black dashed lines show the periods of sampling for each warming level and the standard deviation of GMST from the long-term warming levels for pre-industrial and warming targets of 1.5 °C and 2 °C (8)..... p. 12
- Figure 1.3** Conceptual presentation of the health outcomes from climate change and the potential for reduction through adaptation p. 13
- Figure 1.4** Observed CO₂ gas amount and scenarios for the 21st century. Colored area delineates extreme IPCC (2001) scenarios. Forcings on right hand scales are adjusted forcings, Fa, relative to values in 2000 p. 14
- Figure 1.5** Diagram of main carbon separation/capture methods in the post-combustion category. [MOFs: metal-organic frameworks; PDMS: polydimethylsiloxane; PPO: polyphenyleneoxide; PP: polypropylene] p. 15
- Figure 1.6** Working principle of (a) gas separation membrane process and (b) gas adsorption membrane process p. 21
- Figure 1.7** schematic diagram rotation and inversion pathways of the trans to cis isomerization of azobenzenes p. 22
- Figure 1.8** representative UV-visible absorption spectra associated to an azobenzene compound in the trans-isomer state (blue line) and cis-isomer state p. 22
- Figure 1.9** (a) Hypothetical building unit of the Azo-DMOF-1 and (b) CO₂ adsorption of freshly activated Azo-DMOF-1 and its dynamic photo-switching at 298 K p. 23

Figure 1.10 Chemical structure of some representative cations and anions used in ionic liquids	p. 26
Figure 1.11 Existing 3D printing process and technologies	p. 29
Figure 1.12 Scheme of the free radical polymerization mechanism	p. 31
Figure 1.13 DLP 3D printing technology working principle	p. 32
Figure 1.14 3D printed microcantilevers containing light triggered azobenzene moieties able to modify the mechanical properties. In the plots on the right, variation of the resonance frequency under laser illumination	p. 33
Figure 1.15 (a) Transmittance through a branch of the Y-shaped waveguide versus aperture angle α . (b, c) Fluorescence pictures of the 3D printed waveguides illuminated at one end of the waveguide	p. 34
Figure 1.16 3D printed poly(PEGDMA-coTOPTf ₂ N) objects by mask projection micro-stereolithography	p. 35
Figure 1.17 (a) Sensor fabrication and (b) sensor's architecture made by 3D printing of [emim][BF ₄]/BACOEa composites	p. 36
Figure 1.18 (a) Formulation composition and photo-curing process. (b) Examples of PIL-based 3D printed complex geometry. (c) Multifunctional printing of hydrophilic and hydrophobic PILs	p. 36
Figure 2.1 DLP 3D printers employed for the samples printing, (a) Robot Factory and (b) Asiga and their parameters.	p. 41
Figure 2.2 Permeability measurement apparatus with LASER and optical setup.....	p. 44
Figure 2.3 Photo rheology analysis of formulation containing 0.1, 0.2, 0.3 and 0.4 %wt of (a) MR and (b) DR1M.	p. 46
Figure 2.4 Scheme of the DLP equipment used and printing parameters adopted for the membranes containing the two different dyes.	p. 47
Figure 2.5 ATR FT-IR spectra of (a) PEGDA/MR, (b) of PEGDA/DR1M and (c) of neat PEGDA both in liquid and solid form, highlighted the peak at 1635 cm ⁻¹	p. 48
Figure 2.6 UV-visible spectra of (a) PEGDA/MR and (b) PEGDA/DR1M both in solid and liquid form.	p. 49
Figure 2.7 DMTA analysis displaying the elastic modulus, the loss modulus and the tan delta of the 3D printed samples containing (a) PEGDA/MR and (b) PEGDA/DR1M and (c) neat PEGDA	p. 50
Figure 2.8 DSC analysis of (a) PEGDA/DR1M and (b) PEGDA/MR samples.	p. 51
Figure 2.9 Permeability analysis (curves normalized on thickness) in dark condition of PEGDA membrane containing (a) MR 0% relative humidity at 10, 25,	

50°C, (b) DR1M 0% relative humidity at 10, 25, 50°C, (c) MR at 25°C and 0%, 50%, 100% relative humidity, (d) DR1M at 25°C and 0%, 50%, 100% relative humidity and (e) neat PEGDA 0% relative humidity at 25 °C.....	p. 52
Figure 2.10 Transmission rate curves at plateau during LASER illumination of membranes containing (a) MR and (b) DR1M, (c) calculated permeability, diffusivity and solubility of neat PEGDA, PEGDA/MR and PEGDA/DR1M.	p. 53
Figure 2.11 Permeability increase vs LASER intensity of membrane containing MR and DR1M.....	p. 54
Figure 2.12 Temperature variation during LASER illumination at 5, 25, 50°C initial temperatures of membrane containing MR and DR1M.	p. 55
Figure 2.13 (a) Logarithmic plot of transmission rate of carbon dioxide and oxygen for membrane containing PEGDA/MR, in dark condition, (b) linear plot of oxygen transmission rate in the same membrane, during laser irradiation.	p. 56
Figure 2.14 (a) CAD file of the prototype top and bottom view, (b) exploded vision of the prototype, (c) 3D printed prototype top and bottom view.	p. 58
Figure 2.15 (a) prototype CAD and working principle and (b) solution pH variation in light and dark condition.	p. 58
Figure 3.1 experimental apparatus for CO ₂ capture	p. 65
Figure 3.2 G'(Pa) modulus vs time (s) during irradiation.	p. 66
Figure 3.3 picture of the 3D printed cubic structure.	p. 67
Figure 3.4 storage modulus at 20°C calculated from DMTA analysis.	p. 70
Figure 3.5 FTIR-ATR spectra between 2450 cm ⁻¹ and 2200cm ⁻¹ of (a)neat PEGDA before (black) and after (red) CO ₂ absorption and of (b) P_Bmim[BF ₄] after CO ₂ absorption (red), vacuum cleaning (green) and thermal treatment (blue).	p. 71
Figure 3.6 Diffusivity, solubility and permeability values of membranes containing increasing concentrations Bmim[BF ₄](red) e C ₄ N _{MA,11} [Tf ₂ N] (green). The black line indicates the value calculated for neat PEGDA.	p. 72
Figure 4.1 reaction scheme for 2-methyl-3-butylimidazole.....	p. 78
Figure 4.2 reaction scheme for C ₄ vbmim_Cl.	p. 79
Figure 4.3 reaction scheme for 2-methyl-3-3,3-dimethylbutylimidazole.....	p. 80
Figure 4.4 reaction schematic for (iPr)C ₂ vbmim_Cl.	p. 81
Figure 4.5 (a) UV lamp used for the photo-curing process and (b) prepared photo-cured membranes by UV polymerization.	p. 84
Figure 4.6 molecular structure of Orange G.....	p. 84

Figure 4.7 ^1H NMR (400 MHz) of 2-methyl-3-butylimidazole in Acetone- d_6	p. 87
Figure 4.8 ^1H NMR (400 MHz) of C4vbmim_Cl in DMSO- d_6	p. 87
Figure 4.9 ^1H , ^{13}C and ^{19}F NMR spectra of C4vbmim_TFSI in DMSO- d_6	p. 89
Figure 4.10 ^1H NMR (400 MHz) of 2-methyl-3-3,3-dimethylbutylimidazole in acetone- d_6	p. 90
Figure 4.11 ^1H NMR (400 MHz) of 2-methyl-3-3,3-dimethylbutylimidazole in acetone- d_6	p. 90
Figure 4.12 ^1H , ^{13}C and ^{19}F NMR spectra of (iPr)C2vbmim_TFSI in DMSO- d_6	p. 91
Figure 4.13 FTIR-ATR analysis of (iPr)C2vbmim_TFSI in different IL/PEGDA ratios: (a) 0/100 mol%, (b) 40/60 mol%, (b) 80/20 mol% and (c) 100/0 mol% on uv irradiation times from 0s to 120s.	p. 92
Figure 4.14 FTIR-ATR analysis of C4vbmim_TFSI with IL/PEGDA ratios: 80/20 mol% on UV irradiation times from 0s to 120s.	p. 93
Figure 4.15 C=C double bond conversion for polymerized samples containing C4vbmim_TFSI and (iPr)C2vbmim_TFSI with concentration 80/20 mol% IL/PEGDA.	p. 94
Figure 4.16 Photo-rheology analysis of C4vbmim_TFSI and (iPr)C2vbmim_TFSI. Light is tuned on after 1 minute.	p. 95
Figure 4.17 light absorbance of formulations containing (a) C4vbmim_TFSI and (b) (iPr)C2vbmim_TFSI at 0, 6 and 20 %wt of PDADMA.	p. 96
Figure 4.18 CO_2 transmission rate curves of membranes containing (a) C4vbmim_TFSI and (b) (iPr)C2vbmim_TFSI and 0%wt, 6%wt and 20%wt of PDADMA_TFSI.	p. 96
Figure 4.19 Schematic explanation of the electrostatic complexation process. (a) Chemical structure of PMA; (b) complexation process with neutralized PMA and a PIL (12).	p. 97
Figure 4.20 TGA curves from 25°C to 400°C of membranes containing (a) C4vbmim_TFSI, (b) C4vbmim_TFSI + 25%wt PMA and (c) (iPr)C2vbmim_TFSI + 25%wt PMA.	p. 98
Figure 4.21 DSC curves from -30°C to 200°C of membranes containing (a) C4vbmim_TFSI, (b) C4vbmim_TFSI + 25%wt PMA, (c) (iPr)C2vbmim_TFSI and (d) (iPr)C2vbmim_TFSI + 25%wt PMA.	p. 99
Figure 4.22 3D printing process flow depicting the (a) CAD sketch and the printed samples (b) before and (c) after resin and parameters optimization.	p. 100

Figure 4.23 High pressure CO ₂ uptake analysis for polymerized samples containing (iPr)C2vbmim_TFSI and C4vbmim_TFSI PILs compared to liquid counterpart 1-butyl-3-methylimidazolium bis(trifluoromethylsulfonyl)imide (bmim [TFSI]) (17), with applied pressure from 0 to 40 bar at 25°C. The points of bmim [TFSI] were fitted with a polynomial function of second order.	p. 101
Figure A1 FTIR spectra from 600 cm ⁻¹ to 4000 cm ⁻¹ of samples containing PEGDA/MR, PEGDA/DR1M and neat PEGDA before and after the 3D printing process.....	p. 124
Figure AB1 Experimental setup of the dynamic light-controlled CO ₂ permeability related to pH variation.....	p. 126
Figure C1 FTIR-ATR spectra of neat ILs and neat PEGDA.	p. 127
Figure D1 FTIR-ATR spectra of polymerized formulations before (red) and after (blue) solvent washing. The dashed bars indicate where the peaks of the ILs disappears after solvent washing.	p. 130
Figure E1 FTIR spectra from 600 cm ⁻¹ to 4000 cm ⁻¹ of samples containing mixtures of PEGDA and (iPr)C2vbmim_TFSI in ratios of 100/0, 60/40, 20/80 and 0/100 mol% respectively. The last graph shows the spectrum of the sample containing PEGDA and C4vbmim_TFSI 20/80 mol%.....	p. 133
Figure F1. Nitrogen absorption isotherms of membranes containing C4vbmim_TFSI + 0%wt, 6%wt and 25%wt of PMA.	p. 136
Figure G1. CO ₂ transmission rate curves for membranes containing (iPr)C2vbmim_TFSI and C4vbmim_TFSI + 6%wt of PMA.	p. 137

Chapter 1

Introduction

1.1 Global warming: causes, expectations and solutions

One of the main issues regarding the threatening of the life on earth is the increase of the global temperature, the so-called global warming. Since the beginning of the industrialization era, about two centuries ago, the world's population has increased exponentially and the technological advances have improved substantially (1). The earth system entered in a new epoch, the Anthropocene, in which human activities affected significantly the global environment (2). As a result of human industrial and agricultural activities, climate change has become an aspect of primary importance, leading to serious economic and social effects. The increase of earth temperature is mainly due to the so-called

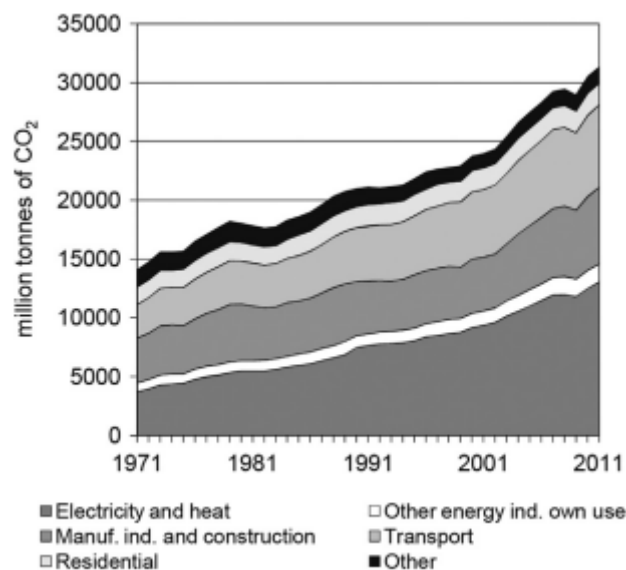


Figure 1.1 Historical trend of world sectorial CO₂ emissions in billion tons from 1971 to 2011 (7).

greenhouse effect. The Irish scientist John Tyndall first used this term, after his experiments regarding the properties of some gases and vapours, present in the atmosphere, to absorb light radiation. Tyndall established that these particular gases, later known as greenhouse gases (GHG), do absorb more energy than oxygen and nitrogen when radiant heat passes through them (3). Between these gases, carbon dioxide is believed to be responsible for approximately three-quarters of the total greenhouse gases emissions (4), 90% of which are generated by fossil fuel

combustion (5). Ten countries, which includes United States, China, India, Russia, Japan, Germany, Korea, Canada, Iran and UK are the major GHG emitters in the world. They are responsible of almost two-third of the total world emissions, proving their direct negative effect on the global environment (6). In the last four decades, CO₂ emissions growth annually more than 100%, surpassing 30 billion tons in 2011 (7). Figure 1.1 (7) shows the amount of CO₂ emitted in the atmosphere divided in sectors of energy consumption. This uncontrolled increase of the CO₂ emissions inevitably caused the increase of the global temperature. The global mean surface temperature (GMST), defined as the annually averaged near surface (2 m) air temperature anomaly, is constantly increasing from the beginning of XX

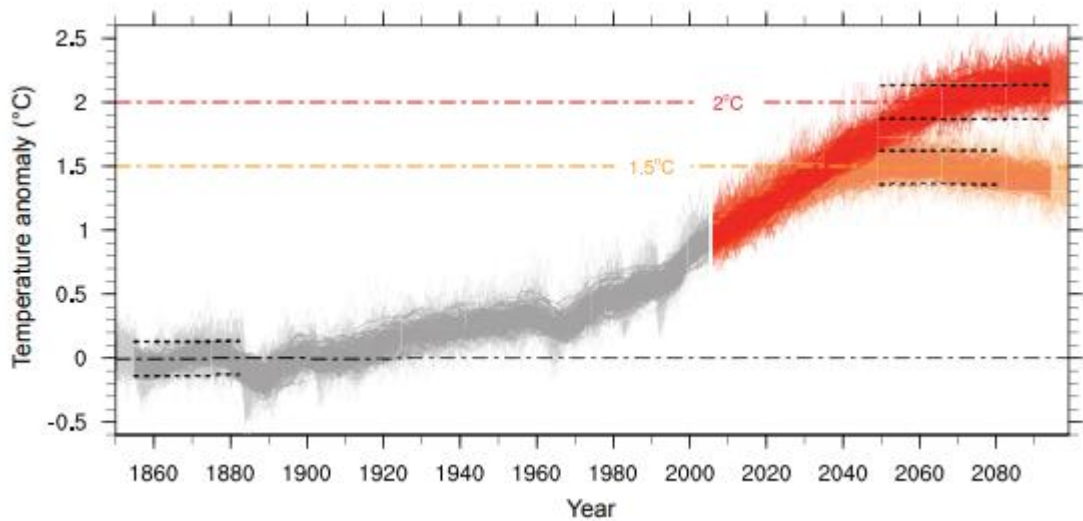


Figure 1.2 Global mean surface temperature (GMST). Historical values for the period 1850–2005 (gray lines), and RCP2.6 (orange lines) and RCP4.5 (red lines) simulation for the period 2006–2099. The black dashed lines show the periods of sampling for each warming level and the standard deviation of GMST from the long-term warming levels for pre-industrial and warming targets of 1.5 °C and 2 °C (8).

century, and has nowadays reached 1°C raise since 1850 (8). Figure 1.2 (8) shows the historical temperature anomaly from 1860 to 2005 and the projections up to 2090, following the Paris Agreement of limiting the global warming to 1.5 °C (hereafter 1.5 °C target) and to limiting warming to 2 °C (hereafter 2 °C target). Nevertheless, measures to mitigate the CO₂ emissions are of vital importance because if no precautions and effective actions will be undertaken, the GMTS could increase by 4 °C (under the scenario obtained from Intergovernmental Panel on Climate Change’s fourth assessment report (9)), with devastating consequences. In

March 31, 2014, the Intergovernmental Panel on Climate Change (IPCC) released its latest report on impacts, vulnerability and adaptation to climate change (10). It states that human health is very sensitive to shifts in weather patterns and these effects occur directly due to change in temperature and its consequences. In particular, it creates three scenarios (present, near future and long term) in which the increase of ill-health is related to climate change occurring through undernutrition, vector-borne diseases, occupational health, mental health and violence, extreme weather events, air quality, food and water-borne infections. Figure 1.3 (10) summarizes the health outcomes caused by climate change and their exacerbations in three different eras: present, 2030-40 and 2080-2100 with an expected temperature increase of 4 °C.

As already mentioned, CO₂ is the gas with the highest concentration in the

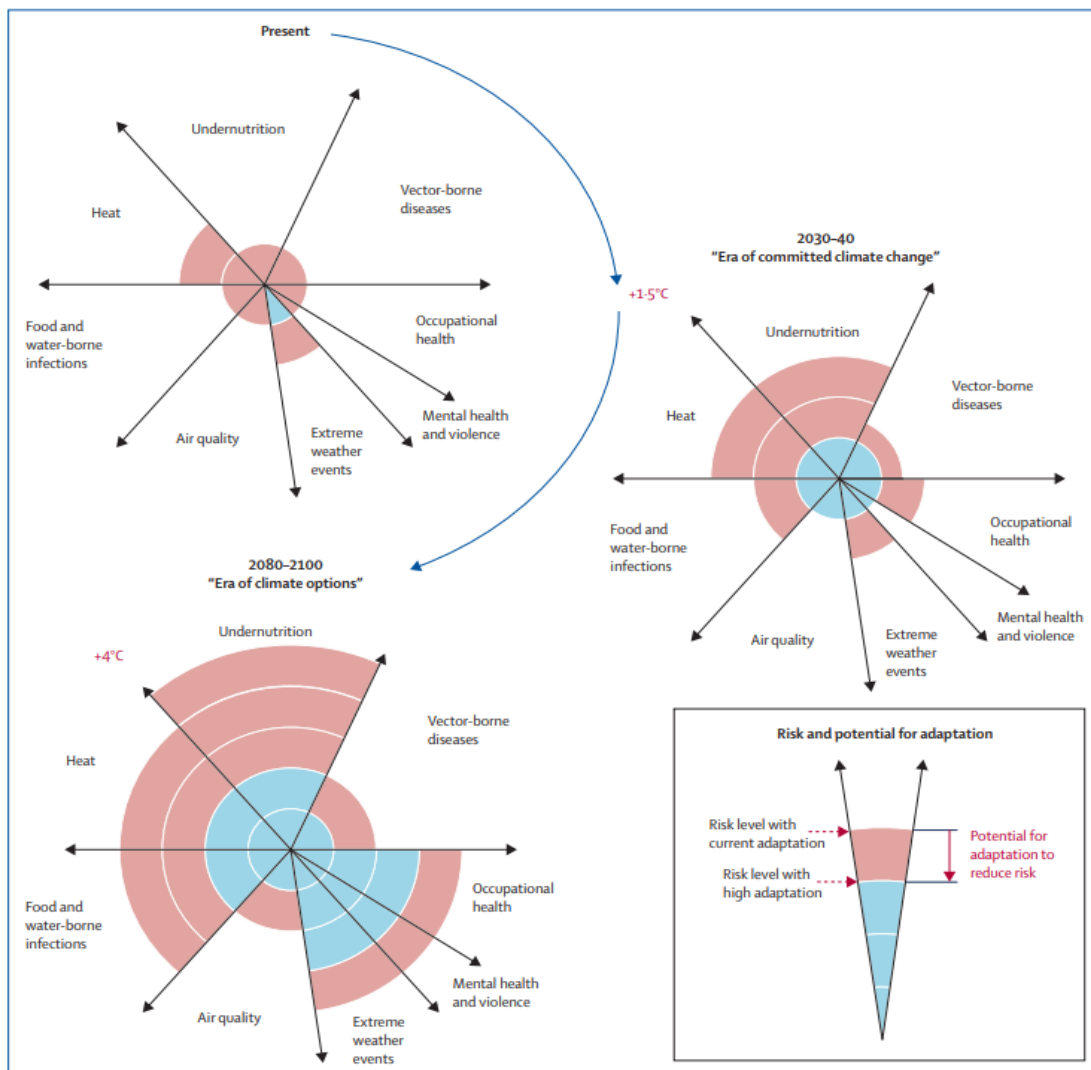


Figure 1.3 Conceptual presentation of the health outcomes from climate change and the potential for reduction through adaptation (10).

atmosphere among the other GHGs, such as methane, nitrous oxide and chlorofluorocarbons (CFCs). The concentration of CO₂ in the atmosphere, due to the anthropogenic emissions, is constantly increasing and it is now attested over

400 ppm. Figure 1.4 (11) shows the observed CO₂ concentration from the end of the 19th century to nowadays and scenarios for the 21th century. Extreme scenarios predict carbon dioxide concentration over 700 ppm before 2100 (12) with no regulations and uncontrolled emissions, but also an “alternative “ and “2 °C”

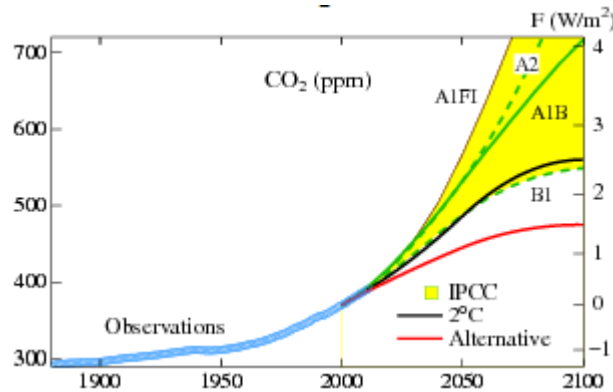


Figure 1.4 Observed CO₂ gas amount and scenarios for the 21st century. Colored area delineates extreme IPCC (2001) scenarios. Forcings on right hand scales are adjusted forcings, F_a , relative to values in 2000 (11).

scenarios (13) for more controlled emissions and efficient methods for CO₂ mitigation. There are two main CO₂ generation sources: combustion CO₂ and process CO₂. The first is generated by the combustion of carbonaceous fuels such as natural gas, petroleum and coal, while process emissions are generated from chemical reactions required to produce desired products such as iron and steel production, petrochemical production, ethylene, ethanol (fermentation), cement production, etc (14). The decrease of CO₂ emissions is becoming an urgent demand and, in particular, the possibility to capture and store it is of prime importance.

In this context, carbon capture and storage (CCS) is considered a critical part of many climate change mitigation plans, as it connects our current economy based on the use of fossil fuels and the future where only renewable energy will be used (15, 16). Different technologies may be adopted for CO₂ capture, and, among the most used, there are gas phase separation, absorption and adsorption (17-21). In the absorption process, CO₂ is absorbed by creating a chemical bond with the absorbing material; it usually requires a lot of energy to be broken (e.g. heating at high temperatures). The sorbents are often liquids and among the most used can be found amines (22-25), lithium based materials (22-25) and ionic liquids (26-29). Adsorption process, on the other hand, involves the selective uptake of CO₂ on a solid surface and it requires a lot less energy to release it, due to the weaker bonds. Among the most common used materials, there are zeolites, activated carbons, metal organic frameworks (MOFs (30-33)), and poly ionic liquids (PILs), which will be analyzed more in details in the section 1.3. For what regards membrane separation technology, which will be better explained in section 1.2.3, CO₂ is selectively separated from a stream of mixed gases through a membrane.

These CO₂ capture processes can be achieved in three main different ways: post-combustion, pre-combustion, and oxy-fuel capture (26, 34-37). The post-combustion capture regards essentially the CO₂ sequestration from the emission

stage of a combustion process, before the emissions are vented in the atmosphere. The most used method, because of its economical convenience, is the CO₂ separation by aqueous amine solution scrubbing (38). In the pre-combustion, instead, the CO₂ is captured before the combustion process. Fossil fuels are gasified with sub-stoichiometric amounts of oxygen and steam at high pressure to produce a mixture of mostly CO and H₂ (39), subsequently, this “synthetic gas” is mixed with water vapor to form CO₂ and H₂, through a catalytic reaction, following the reaction showed in Eq.1 (40). CO₂ is then separated to leave a hydrogen rich fuel gas ready to be combusted.



Finally, the oxyfuel combustion process consist in supplying only oxygen during the combustion. Differently from other forms of combustion in which air is used as combustion agent, in this case the side products are mainly CO₂ and water vapor that can be easily condensed, leaving only CO₂ to be stored (41).

1.2 Carbon capture technology

As already mentioned, the main Carbon capture (CC) technologies are based on absorption, adsorption and membrane separation processes. This kind of processes are mostly applied to post combustion CC technique because of its more easily implementation in the existing power plants, compared to pre-combustion and oxyfuel (42). Figure 1.5 (43) shows the subcategories of processes applied to post-combustion CO₂ capture and the materials used for each sorption process. In the next subsections, the main materials employed in the absorption, adsorption and membrane separation will be discussed.

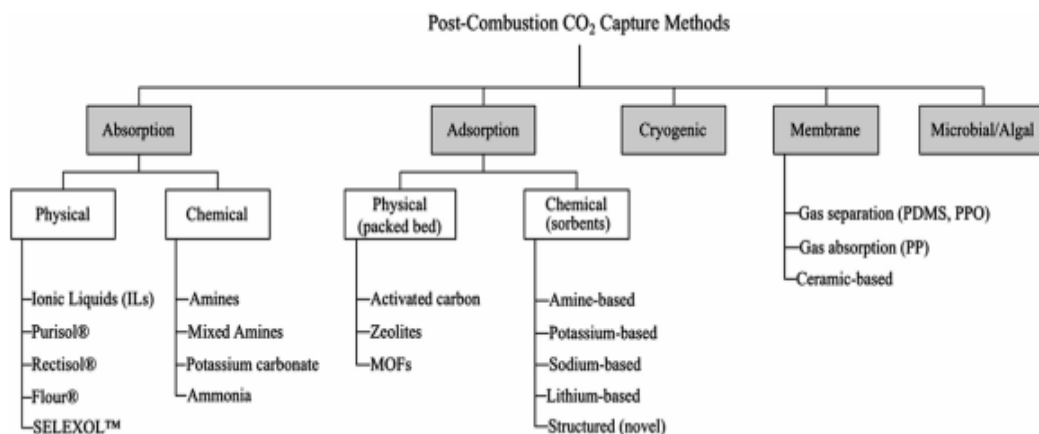


Figure 1.5 Diagram of main carbon separation/capture methods in the post-combustion category. [MOFs: metal-organic frameworks; PDMS: polydimethylsiloxane; PPO: polyphenyleneoxide; PP: polypropylene] (43).

1.2.1 Absorption processes

The adsorption mechanism is a technical option that can be used both in pre-combustion and post-combustion processes and has been already commercialized. This process is divided in two categories: physical absorption and chemical absorption.

In the physical absorption, where high pressures and low temperatures are applied (44), the separation occurs by physical methods with mass transfer at the gas-liquid interface. It is dependent on the solubility of the gas, interface surface area and operating conditions (45). Although it requires a high gas pressure to be competitive, the energy involved in the regeneration of the solvent is low (46). The main materials employed in this kind of process are Selexol, Rectisol and ionic liquids (ILs). Selexol process uses dimethylether of poly(ethylene glycol) (DMPEG) as a solvent and it is able to reduce the CO₂ levels by 85% (47). It is usually employed in pre-combustion processes because of its ability to absorb CO₂ and other acid gases from syngas. The typical operating temperature range is 5-40 °C and the pressure is usually maintained at 2 MPa and 12 MPa (48). Rectisol process uses cold methanol as solvent. The typical operating temperature range is between -29 °C and -60 °C (48), at a partial pressure of about 1 MPa (49). It is used in pre-combustion process for its optimal ability to remove acid gases such as hydrogen sulfide, carbonyl sulfide, and carbon dioxide from syngas, and for its high selectivity (50). Ionic liquids (ILs), which will be further discussed in section 1.3, have gained a lot of attention as applications in CCS technologies (26-29), due to their outstanding chemical and physical properties, such as low melting point and very low vapor pressure. Moreover, their chemical composition can be tuned by interchanging different anionic and cationic species, with the possibility to obtain a remarkably high number of combinations. In particular, they can be manipulated in such a way that their CO₂ solubility can be optimized. ILs have been widely employed in form of absorbing liquid blends, nevertheless, this method caused problems related to their high viscosity and instability of the systems (51).

Since the concentration levels of CO₂ in flue gases of coal-fired power plants are not more than 15% of the total flue gas (52, 53), chemical absorption is preferred because it requires lower working pressures compared to physical absorption. This allows chemical absorption to possess higher CO₂ uptake capacity at low CO₂ partial pressure (54). Chemical absorption requires three components i.e. solvent, absorber and stripper. The flue gas from a coal-fired plant, containing CO₂, come in contact with the lean solvent in counter-current mode. CO₂ is absorbed by the solution leaving a mix of gas poor in CO₂. The CO₂ rich solvent is then regenerated by the stripper (45). Between the most used materials employed in chemical absorption, there are aqueous alkanolamines, which are the most commercially successful nowadays (45). Monoethanolamine (MEA) was one of the earliest amine-based materials used in carbon dioxide capture, because of its low cost, high

absorption capacity and good reaction rate. Unfortunately, it has major drawbacks characterized by degradation in oxidizing environments, high corrosion rate and high regeneration energy (20, 55-57). Diethanolamine (DEA) was also used as chemical absorber in CO₂ capture but with the same limitations. Combinations of MEA and DEA, like methyldiethanolamine (MDEA), were studied with successful results, improving loading capacity, corrosion resistance and reduction of regeneration energy (58-60). Sterically hindered amines, like 2-amino-2-methyl-1-propanol (AMP), were employed with good CO₂ absorption results, high selectivity and low regeneration energy (61-63). Piperazine (PZ) cyclic diamines were also used for their good CO₂ uptake, corrosion resistance and low energy cost for regeneration (64). Ionic liquids with functional groups like amino acids, were studied for CO₂ capture, exhibiting good CO₂ absorption ability, lower energy penalties for regeneration, higher selectivity and higher thermal and chemical stabilities (65, 66).

The absorption of CO₂ on amine sorbents consists mainly in three mechanisms (67):

Zwitterion mechanism: CO₂ and solvent form a zwitterion (Eq. 2), which is then deprotonated by a base to form carbamate (68) (Eq. 3). The main reaction occurs, applied to primary, secondary and sterically hindered amines, as follow.



Ter-molecular mechanism: the formation of the zwitterion and deprotonation occur at the same time (Eq. 4).



Base-catalyzed hydration mechanism: tertiary alkanolamines have a base-catalytic effect on the process of hydration of CO₂, leading to amine dissociation (see Eq. 5).



Other research proposed that the O⁻ and OH groups of promoters, used to enhance the performance of the absorbent, could act as Lewis bases with CO₂ (69, 70). Besides the utilization of alkanolamines, use of aqueous potassium carbonate (K₂CO₃) promoted with inorganic salts was reported as effective CO₂ absorber due to reduced enthalpy, degradation and cost (70-74). An additional material used as a chemical absorber is aqueous ammonia, characterized by a high CO₂ capture efficiency and ability to remove SO₂, NO_x as well as easy availability and low regeneration costs (68, 75-77).

1.2.2 Adsorption processes

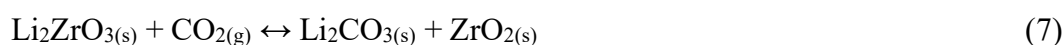
In adsorption processes, differently as described in absorption processes, one or more components of a mixture of gases (containing CO₂) are removed with the help of a solid surface. In fact, in this case the uptake is achieved exploiting the intermolecular forces between the gas and the surface of the solid sorbent. Usually, an adsorption process requires the use of a packed column filled with spherical adsorbent and a stream of mixed gases flowing through the column. The CO₂ contained in the gas is adsorbed on the beads surface until the thermodynamic equilibrium is reached. Once the process has reached the equilibrium, the solid sorbent can be regenerated by stopping the feed mixture flow, reducing the pressure and cleaning the sorbent by fluxing a low adsorptivity gas (78). The adsorption process can be achieved by exploiting three main technologies i.e. pressure swing adsorption (PSA), temperature swing adsorption (TSA) and electrical swing adsorption (ESA). In PSA, the feed gas is pressurized in the bead column at a pressure of about 6 bar and temperature of 35°C. Water vapor is preventively removed from flue gas by molecular sieves. After the adsorption process, the sorbent is regenerated by depressurization at 1 bar (79). For the temperature swing adsorption process, the selective adsorption of CO₂ takes place on the adsorbent until the equilibrium is reached. The desorption is carried out, in this case, by supplying additional heat by purging the bed with a preheated gas. This heating process makes this technology less cost effective than PSA (80). In the electrical swing adsorption method, the process is similar to TSA process with the difference that instead of heating the beads, a low voltage electric current is applied through the column to regenerate it (81).

In addition, also for what regards adsorption processes, a distinction between physical adsorption and chemical adsorption is made. In physical adsorption, the most important characteristic of the sorbents is their high porosity that enables the gas to highly interact with the material. The physical characteristics that play a role in the process are the pore volume, pore size distribution and surface area. Between the most employed sorbent materials used in physical adsorption there are activated carbon, zeolites, and MOFs. Activated carbon is a material base on carbonaceous matter that is activated by carbonization at 400°C – 500°C and gasified at 800°C – 1000 °C to develop the porosity and high surface area. It is characterized by a slightly polar surface that gives the following advantages: hinders the absorption of water, avoiding separation and purification processes, make it adsorbing more nonpolar and weakly polar organic molecules than other adsorbents and lowers its heat of adsorption, resulting in lower energy requirements for sorbent regeneration. Zeolites, on the other hand, are crystalline aluminosilicates of alkali earth elements such as sodium, potassium and calcium, represented by the stoichiometry:



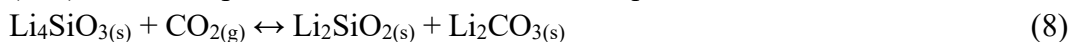
Where x and y are integers with $y/x \geq 1$, n is the valence of cation and z is the number of water molecules in each unit cell. Zeolites are divided in types, from 1 to 5 depending on their aperture size. Different gases can be adsorbed in the zeolites pores according to their molecular dimensions. Zeolites applied in CO_2 adsorption are in form of pellets and are typically of type 4A with a normal aperture size of 4 Å (80). Nevertheless, zeolite 13X is widely used as adsorbent for CO_2 , with an uptake capacity of 4.7 mmol g^{-1} at 1 bar and 298 K (82). For what regards metal-organic frameworks (MOFs), they are a class of crystalline nanoporous materials that combine metal organic centres with organic ligands to create large three dimensional crystals with permanent porosity. MOFs have potential applications in gas storage, ion exchange, molecular separation and heterogeneous catalysis (83-85). They are characterized by a remarkably high surface area, greater than $4000 \text{ m}^2 \text{ g}^{-1}$, pore diameters typically in the range 3 to 20 Å (86-89), high void volumes and low densities (from 0.21 to 1 g cm^{-3}), which can be maintained upon CO_2 evacuation (90). The high surface-to-volume ratio of MOFs allows to obtain enhanced CO_2 adsorption capacity compared to zeolites (91). They also possess great gas selectivity with application in CO_2/N_2 (post-combustion), CO_2/H_2 (pre-combustion) or CO_2/CH_4 (natural gas sweetening) separations. Outstanding results in CO_2 capture were reported in MOFs with high surface areas and pore diameters greater than 15 Å. The framework $[\text{Zn}_4\text{O}(\text{btb})_2]$ (MOF-177, $\text{btb}^3 = 1,3,5$ -benzenetribenzoate) with a surface area of $4500 \text{ m}^2 \text{ g}^{-1}$ exhibited the highest capacity for CO_2 , with an uptake of 33.5 mmol g^{-1} at 32 bar (92).

As already mentioned, adsorption process can be chemically based. The incorporation of organic amines into a porous support was studied as promising approach for CO_2 chemical adsorption, combining good uptake capacity and selectivity at a moderate temperature. Studies were done on porous supports impregnated with liquid amines, however, loss of amine components due to evaporation was a major drawback (93-96). Grafting the amine functional groups directly on the physical sorbents eliminated the problem and improved the overall thermal stability of the system. For instance, amine-modified silica gels (e.g. alkylamine on silica (97, 98) or amino-silane liquids (99)) and polymers (e.g. polystyrene-based copolymers with covalently bonded diamine functional groups (100)), were demonstrated to reversibly chemically adsorb CO_2 (101). Another class of materials employed in CO_2 capture is lithium based oxide materials, like lithium based zirconate (Li_2ZrO_3) and lithium based silicate (Li_4SiO_4) (102). The absorption mechanisms of both sorbents are reported in Eq. 7 and Eq. 8 respectively.



The reaction in Eq.7 is reversible at 450-590 °C and forms eutectics carbonate compounds that can accelerate the adsorption reaction (103). Lithium silicate,

instead, possesses higher CO₂ adsorption capacity (104) and is reversible at 720 °C (105). The adsorption mechanism is shown in Eq. 8.



1.2.3 Membrane technology

Membrane technology has been explored for CO₂ capture from flue gas emissions because of its fundamental engineering and economic advantages over other separation technologies (106). Membranes for CO₂ capture are often listed as good candidates in applications in post-combustion processes for their low cost. However, the main issues related to these processes can be the reduced pressure and the low CO₂ concentration in the flue gas, which require membranes with high CO₂selectivity (107). Furthermore, a membrane, to be suitable for CO₂ capture, should possess some properties, reported below (108) :

- High CO₂ permeability
- High CO₂/N₂ selectivity
- Thermal and chemical resistance
- Aging resistance
- Cost effective

The main engineering considerations on membranes for CO₂ capture are the operating flexibility, which depends on the CO₂ concentration in the flue gas stream (it must be high as possible); the good turndown, which is the capability of the system to operate at reduced capacity; the high reliability, which accounts the good response to unscheduled shutdowns; and the ease of expansion, which contemplate the future expansion possibilities after the design phase (106).

Membrane technology for carbon capture is mainly classified in two types: gas separation and gas adsorption membranes. For what regards gas separation membranes (see Figure 1.6a (109)), the process consists in applying the stream of mixed gases at a high pressure into the membrane separator and selectively permeate the CO₂ through the membrane on the other side at reduced pressure. The main parameters that play a role in the separation process are the permeability and permselectivity of the membrane. In fact, in order to have a high flow rate of the permeating CO₂ through the membrane, permeability must be sufficiently high; moreover, permselectivity, defined as the ratio between the permeant gas and the not permeant one, must be as high as possible to have a good efficiency of separation (78, 106). The most used materials in gas separation membrane include polymeric, ceramic, a combination of both or mixed matrix membranes (110). Poly ionic liquids (PILs)-based membrane, which will be further discussed in section 1.3.2, were studied and fabricated. For example, PILs membranes were prepared with 1-ethyl-3-methylimidazolium bis(trifluoromethanesulfonyl)imide ([C₂mim][Tf₂N]) giving high CO₂/N₂ and CO₂/CH₄ permselectivity of 39 and 27 respectively, the addition of 20 mol% of free [C₂mim][Tf₂N] into the polymer enlarged the effects on CO₂ permeability with an increase of 400% (111).

Commercially available Pebax[®] MH 1657 and its blends with low molecular weight poly(ethylene glycol) PEG membranes were produced showing CO₂/H₂ and CO₂/N₂ selectivity of ~ 11 and ~ 47 respectively (112). Fluorinated poly (ether imide) membranes were also created displaying good CO₂/CH₄ permselectivity between 28.59 and 38.86 (113). PDMS coated hollow fiber membranes with 27 or 30 wt.% PVDF in DMAc (N,N-Dimethylacetamide) or NMP (Nimethyl-2-pyrrolidone) were fabricated showing CO₂/N₂ permselectivity of ~ 24.11 (114). Further studies were conducted on polymeric and organic/inorganic hybrid membranes (postcombustion: CO₂/N₂ separation), ceramic microporous membranes (pre-combustion: H₂/CO₂ separation) and dense ceramic mixed oxygen ionic-electronic conducting membranes (oxyfuel combustion: O₂/N₂ separation). These studies resulted in an improvement in CO₂ separation compared to conventional physical absorption techniques in pre-combustion process and an

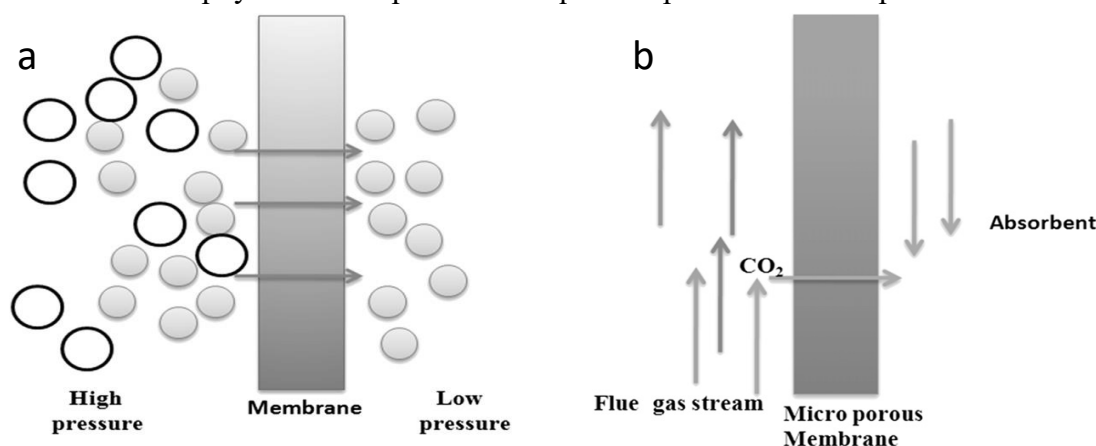


Figure 1.6 Working principle of (a) gas separation membrane process and (b) gas adsorption membrane process (109).

innovative use of polymer membranes as competitive technology for CO₂/N₂ separation (115).

Gas adsorption membranes, on the other hand, consists of micro porous solid membrane that is used as contacting medium between the gas and a liquid adsorbent, as shown in Figure 1.6b (109). The CO₂ from the flue gas diffuses through the membrane and is recovered from the adsorbent. This process gives high separation rates due to the continuous re-change of the adsorbent liquid (116). This process is considered highly flexible for concentration higher than 20%, concentrations lower than 20% can produce reduction of the driving force leading to a decreasing of the CO₂ recovery (106). Examples of materials used for this kind of membranes and the liquids employed as adsorbent are reported here. Polypropylene (PP) hollow fiber membranes with a pore size of 0.05 μm and 60% of porosity, in parallel with single amino-acid salt solution (glycin salt) and composite amino-acid-based solution (glycin salt + piperazine) were produced, showing a good mass transfer (117). Asymmetric hollow polyvinylidene fluoride (PVDF) membranes with pore size: 2.33 ± 0.51 nm and porosity (%) 0.83 ± 2.49 with water and NaOH-water solution as adsorption liquids were created, displaying high CO₂ flux, given by the high CO₂ solubility (118). PP, polytetrafluoroethylene

(PTFE), polymethylpentene (PMP) and a Teflon AF dense skin coated on a PP hollow fiber were also tested with MEA-water solution in CO₂/N₂ mixture (15% vol CO₂), showing high CO₂ flux and mass transfer (119).

1.2.3.1 Azobenzene compounds

An important class of materials employed in gas transport control and separation, are azobenzene derivatives. Azobenzene compounds are aromatic molecules characterized by two benzene rings connected by an N-N double bond (C₆H₅N=NC₆H₅) that can be opened by an external source of energy such as photons or heat. In this way, the molecule can isomerize, passing from a thermodynamically stable *trans* state (E) to a metastable excited *cis* state (Z) (120), both by in plane and out of plane transition pathways (121) (see Figure 1.7 (121)).

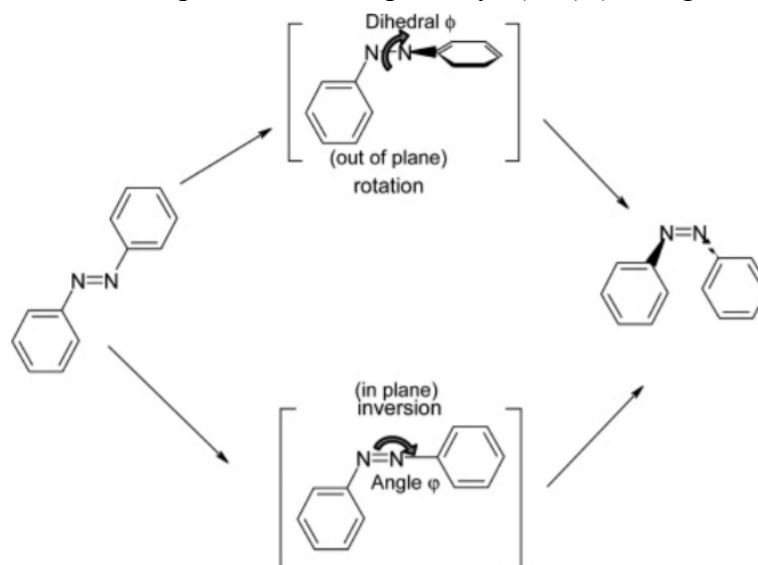


Figure 1.7 schematic diagram rotation and inversion pathways of the *trans* to *cis* isomerization of azobenzenes (121).

The isomerization process can be investigated by means of UV-visible spectroscopy, since the molecule, switching from one state to the other, changes its absorption band due electronic transitions at different energies (120). Figure 1.8 (120) depicts a representative absorption spectrum of an azobenzene compound in the *trans* and *cis* states.

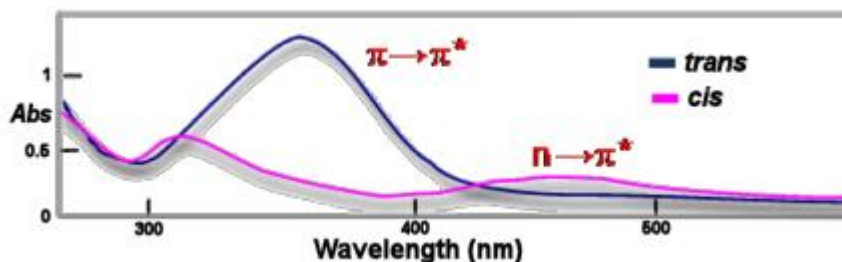


Figure 1.8 representative UV-visible absorption spectra associated to an azobenzene compound in the *trans*-isomer state (blue line) and *cis*-isomer state (120).

The ability of the derivatives of azobenzene compounds to isomerize under light irradiation has attracted a lot of researchers to use them as efficient molecular photo-switches, that allow to control an extended number of properties of the material (122, 123). Because of the conformational transitions of the azobenzene molecules between an extended (trans) and a compact (cis) geometrical conformation (124, 125), the research have been mainly focused on opto-mechanical transducers based on azo-benzene materials (126). In 2006, Henzl et al. (127) directly saw through scanning tunneling microscopy (STM) a single molecule of azobenzene (Disperse Orange 3) on Au(111), triggered by tunneling electrons. They could see the molecule successfully switching more than 70 times, by transferring electrons energy, between three configurations: two bent forms and one elongated form. Furthermore, many studies have been carried out in the use of polymeric membranes containing azobenzene derivatives for gas transport control (128-131). In fact, the photo-induced change in the bulk characteristic of the azopolymers, such as the increase of the free volume in the polymer matrix brought by the cyclic photo-isomerization of the azobenzene chromophores, can be reflected in the change of the intrinsic permeability (128). In this context, Kameda et al.(128) conducted a study on thin films of a copolymer of methyl methacrylate and 2-(ethyl-[4-(4-nitrophenylazo)phenyl]amino)ethyl methacrylate (PMD77) in the glassy state. They irradiated the membranes with blue light and recorded the change in helium permeability due to the photo-isomerization of the azo-chromophores. Recently, Bujak et al.(129) produced membranes based on polyimides containing azo-benzene chromophores linked to the main chain and recorded an increase of the permeability to different gases (i.e. N₂, O₂, He and CO₂) upon light irradiation in relation to the reference neat polyimide. In 2018, Prasetya et al. (130)

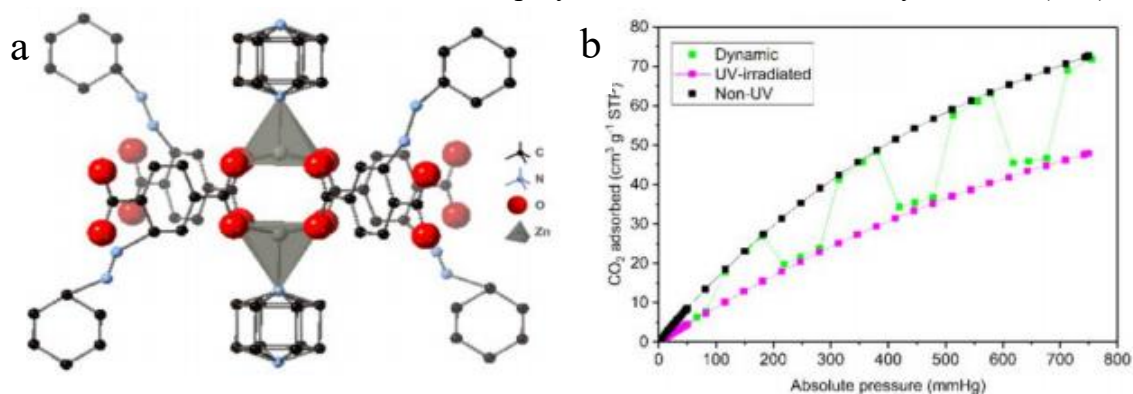


Figure 1.9 (a) Hypothetical building unit of the Azo-DMOF-1 and (b) CO₂ adsorption of freshly activated Azo-DMOF-1 and its dynamic photo-switching at 298 K (131).

synthesized a light-responsive MOF with an azo-UiO-66 topology, using zirconium as the metal source and 2-phenyldiazenyl -terephthalic acid as the light-responsive ligand. The Azo-UiO-66 was found to have a satisfactory performance for CO₂/N₂ separation and exhibited a very efficient CO₂ dynamic photoswitching, which was beneficial for low-energy CO₂ capture. Azo-UiO-66 was also robust and could maintain its porosity and photoresponsivity even after two cycles of immersion in

water. This study confirmed these kinds of materials to be good candidates for low energy post combustion CO₂ capture that utilizes UV light to trigger the CO₂ release. They also did a similar work using Zn as the metal source and both 2-phenyldiazenyl terephthalic acid and 1,4-diazabicyclo[2.2.2]octane (DABCO) as the ligands (131). Figure 1.9 (131) shows the structure of the Azo-DMOF-1 and a CO₂ adsorption/desorption in dynamic UV irradiation photoswitching. In Chapter 2, a study on light-controlled permeability in polymeric membranes containing azobenzene chromophores will be presented.

1.3 Ionic liquids and poly ionic liquids

In recent years, ionic liquids (ILs) have gained a lot of attention as alternative solution to amine based adsorbents in CO₂ capture processes (132). ILs are essentially salts characterized by a strong ion-ion interaction, compared to other intermolecular forces such as London forces in inorganic solvents, leading to a negligible volatility at ambient pressure (133). Furthermore, they possess high thermal stability, large electrochemical range and the ability to dissolve compounds with different polarities (134). From the environmental point of view, ILs are non-flammable, non-volatile and recyclable compared to other solvents (135, 136). Moreover, their physical and chemical properties can be modified by choosing the cation and anion, becoming suitable for specific applications (137). ILs have been largely employed in gas capture and particularly in carbon capture technology, due to their elevated CO₂ solubility (135, 138, 139). The major drawback of ILs used for CO₂ capture, is their elevated viscosity due to their complex synthesis and purification processes (140). Nevertheless, their viscosity can be tuned by using a proper combination of cation and anion, for example, by increasing the alkyl chain length in the cation. Furthermore, also the CO₂ solubility can be enhanced by modifying efficiently the cation and the anion, even if, compared to commercially available technologies such as amine-based systems, their CO₂ capture capacity is still lower (141). ILs can also be functionalized by adding a reactive group able to polymerize or co-polymerize to form chains with high repetitive order and to produce a polymer structure, the so-called poly ionic liquids (PILs) (142-146). This kind of materials are usually synthesized from ILs monomers, showing improved processability, enhanced stability, durability and better control over their meso- to nano-structures (142). PILs based compounds have been exploited to produce materials as novel promising solutions in the area of electrochemistry, analytical chemistry, bioscience, catalysis, sensors and energy environment (147-150). Moreover, studies have been conducted to explore the CO₂ uptake capacity of these materials, thanks to their superior CO₂ solubility (151, 152).

1.3.1 Ionic liquids characteristics

Physical and chemical properties of ionic liquids vary on the types of anions and cations present in the molecule. Ionic liquids structures and, therefore, the variety of their ions is in constant expansion, since the possible combinations are nearly infinite. Nevertheless, a little part of cations and anions mostly employed in research and commercial applications exists. Figure 1.10 (153) shows the structure of some of the representative cations and anions used in protic, aprotic, dicationic, polymeric, magnetic and solvate ionic liquids (153). From left to right, the cations (top row) include: ammonium, pyrrolidinium, 1-methyl-3-alkylimidazolium, 1,3-bis[3-methylimidazolium-1-yl]alkane; (second row) phosphonium, pyridinium, poly(diallyldimethylammonium), metal (M^+) tetraglyme. The anions include (third row) halides, formate, nitrate, hydrogen sulfate, heptafluorobutyrates, bis(perfluoromethylsulfonyl)imide, tetrafluoroborate, (bottom row) thiocyanate, hexafluorophosphate, tris(pentafluoroethyl)trifluorophosphate, dicyanamide, poly(phosphonic acid), and tetrachloroferrate. Common physical properties considered to evaluate ILs for CO_2 capture and the design of the absorption process are density, viscosity, surface tension, vapor pressure, criticalities and all the thermodynamic properties like interfacial tension of liquid-vapor, conductivity and specific heat capacity. The density of ionic liquids is higher than water, except for pyrrolidinium dicyano-diamide and guanidinium. Moreover, ILs density declines with the increase of carbons in the alky chain, differently from viscosity that increases with increasing of the number of carbons in the alky group (134). High viscosity is an issue in ionic liquids used for CO_2 adsorption, due to problems

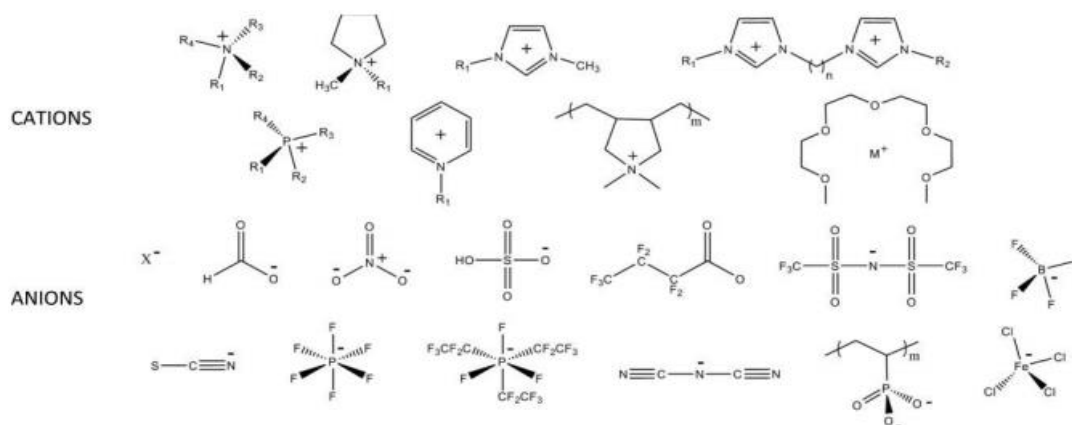


Figure 1.10 Chemical structure of some representative cations and anions used in ionic liquids (153).

related to liquid flux and reduced solubility. Nevertheless, temperature and chemical additives strongly affect the viscosity. In fact, increasing temperature and/or adding organic solvents lead to a reduction of the viscosity (43). Surface tension of ILs is rarely found in literature, but it has been reported that ionic liquids surface tension is higher than in other conventional solvents. Vapor pressure of chemical components is a requirement in applications such as gas separation and, according to the literature, many ILs possess negligible vapor pressure (43), which is an extremely appealing property for what regards, for example, membrane

Table 1.1 Physical properties: T_m : melting temperature; T_b : boiling temperature; ρ : density; μ : viscosity; P^{sat} : vapor pressure; D : diffusion coefficient; γ_{LV} : interfacial tension of liquid-vapor; κ : conductivity; and C_p : specific heat capacity at constant pressure (153).

Parameter ^a	Solvent type				
	Atomic	Molecular	Molten salt	Ionic liquid	
	Hg	H ₂ O	NaCl	PL [CH ₃ CH ₂ NH ₃] ⁺ [NO ₃] ⁻	AIL [C ₆ mim] ⁺ [PF ₆] ⁻
T_m (°C)	-38.8	0	801	12	10
T_b (°C)	356.7	100	1413	255	409
ρ (g/cm ³)	13.53	0.997	1.539	1.21	1.366
μ (Pa.s)	1.526×10^{-3}	8.95×10^{-4}	12.5×10^{-4}	35.9×10^{-4}	36.9×10^{-4}
P^{sat} (Pa)	2.67	3173	12700	0.49	$< 10^{-2}$
$D \times 10^{-6}$ (cm ² /s)	85	22.99	Na ⁺ : 80.1 Cl ⁻ : 63.5	[CH ₃ CH ₂ NH ₃ ⁺]: 0.158 [NO ₃ ⁻]: 0.151	[C ₆ mim ⁺]: 1.5 [PF ₆ ⁻]: 1.8
γ_{LV} (mN/m)	486.5	72.8	111.7	47.3	43.8
κ (S/cm)	10^5	5.5×10^{-4}	0.256	2.69×10^{-2}	1.4×10^{-3}
C_p (J/mol.K)	27.98	75.3	66.9	206	406

impregnation for CO₂ separation. In Table 1.1 (153) a comparison of the physical properties between four different solvents and IL 1-butyl-3-methylimidazolium hexafluorophosphate ([C₄mim] [PF₆]) and PIL ethylammonium nitrate([CH₃CH₂NH₃] [NO₃]) is reported (153).

1.3.2 Ionic liquids and poly ionic liquids for CO₂ capture

As already mentioned before, ILs have been employed as materials for CO₂ capture, mainly in post-combustion and pre-combustion technology. They have been used mostly in physical processes, for conventional ILs, and in chemical absorption processes, for functionalized ILs. It was found that ILs possess a high CO₂ solubility and, in particular, that anions have a higher impact on it compared to cations (154). Aki et al. (155) conducted a study on ten different imidazolium-based ILs and calculated the CO₂ solubility changing the anions. They discovered that between the fluorinated anions, the one with the highest solubility was bis(trifluoromethanesulfonyl)imide [TFSI]⁻, while for the non-fluorinated anions, was [NO₃]⁻. The cation also plays a role in CO₂ capture, in fact, it was demonstrated that CO₂ solubility can be affected by modifying the cation alkyl chain. In particular, an increase of the number of carbon of the alkyl groups corresponds to an increase of CO₂ solubility (155). Moreover, it was reported that imidazolium-based ionic liquids have better performances in CO₂ capture than ILs with different cations, such as phosphonium-based ILs (156).

Ionic liquids can also be functionalized to add particular chemical reactive groups to the molecules and increase their solubility, the so-called task-specific ionic liquids [TSIL]. These kind of ionic liquids usually possess greater capture capacity than conventional ionic liquids, due to their specific modifications to absorb more CO₂ (43). Most of the studies refers to the use of amino-acid groups as functionalities attached both to the cation and to the anion. Goodrich et al. measured the CO₂ solubility of phosphonium-based ILs with different amino-acids functionalizations on the anion, such as trihexyl(tetradecyl)phosphonium glycinate ([P66614][Gly]), alanate ([P66614][Ala]), sarcosinate ([P66614][Sar]), valinate ([P66614][Val]), leucinate ([P66614][Leu]), and isoleucinate ([P66614][Ile]) with solubilities of about 0.5 mol/mol at 1.5 bar. ILs with amine functionalizations on the cations were studied as well on imidazolium based ILs. CO₂ solubility was calculated on 1-aminopropyl-3-methylimidazolium-based ILs with dicyanamide [DCA]⁻, tetrafluoroborate [BF₄]⁻ and bis(trifluoromethanesulfonyl)imide [TFSI]⁻ anions, with solubility values around 0.2 - 0.3 mol/mol at 10 bar (43). Another important aspect to take into account in CO₂ capture is the selectivity of ILs towards the gas. In fact, in most of the CO₂ capture processes (e.g. post combustion) the flue-gas contains a lot of impurities and other gases (157). Conventional ILs have higher CO₂ selectivity than to other gases, such as CO, H₂ and O₂, thanks to the large quadrupole moment of CO₂ (158). Nevertheless, ILs anions and cations can be modified to further increase this value. The promising ILs in terms of selectivity

of CO₂ over other gases (e.g., methane) include BF₄, NO₃, and CH₃SO₄ anions and cations such as Tetrabutylammonium (N4111), Pentamethylguanidinium (pmg), and Tetramethylguanidinium (tmg) (159).

As already mentioned, the use of ILs can have problems related to their high viscosity in systems in which the solvent must flow in pipes. For that reason, supported ionic liquids membranes (SILM) were studied to obtain better absorption efficiency. SILMs are made using liquid phase ILs on a solid membrane. Properties like high viscosity and low vapor pressure, are in this kind of technology an advantage because can stop the membrane solvent flowing out or evaporate, prolonging the SILM's life. Key properties of these membranes are the permeability and selectivity to CO₂. Porous hydrophilic polyethersulfone (PES) membranes containing ILs with bis(trifluoromethanesulfonyl) imide [Tf2N]⁻, trifluoromethanesulfone [CF₃SO₃⁻, chloride [Cl]⁻, and dicyanamide [Dca]⁻ anions (160), 1-butyl-3-methylimidazolium [TFSI]⁻ fixed to porous Al₂O₃ (161), 1-butyl-3-methylimidazolium [PF₆]⁻ to a porous (ceramic or zeolite) membrane (162) and 1-butyl-3-methylimidazolium [BF₄]⁻ supported on the PVDF (poly-vinylidene fluorolide) membrane (163) are few examples of SILMs applications, which gave good results in CO₂ permeability and selectivity. Other research affirmed that CO₂/CH₄ selectivity can be further increased by increase the gas pressure, leaving mechanical stability unchanged (164). Many studies were carried out also on SILMs with functionalized ILs by adding amine groups to the anion or cation (165-167).

One of the main problems related to SILM technology is the leakage of the IL from the membrane, when the pressure drop surpasses the liquid stabilizing forces within the matrix (164). To overcome this issue, PILs were used for CO₂ capture purposes, showing a significant increase of the CO₂ uptake capacity compared to the analogue conventional ILs (145, 168). Moreover, PILs showed reduced time of absorption/desorption and selective CO₂ absorption in mixed atmosphere of N₂/O₂/CO₂ (143, 168). Further studies were conducted on grafting of polyethylene glycol (PEG) onto PILs to create CO₂ selective membranes with improved thermal, chemical and mechanical properties (169). Bara et al. (145) reported a study on synthesized photo-curable room temperature ionic liquids (RTILs) that could be converted into PILs films. They tested the membranes for their performance in separation, involving CO₂, N₂ and CH₄ with good results both in selectivity and CO₂ absorption capacity.

1.4 3D printing

1.4.1 Introduction to 3D printing

3D printing finds its bases in what is called additive manufactory (AM), which definition is the “process of joining materials to make object from three-dimensional (3D) model data, usually layer upon layer, as opposed to subtractive manufacturing methodologies” (170). One of the earliest AM processes, firstly

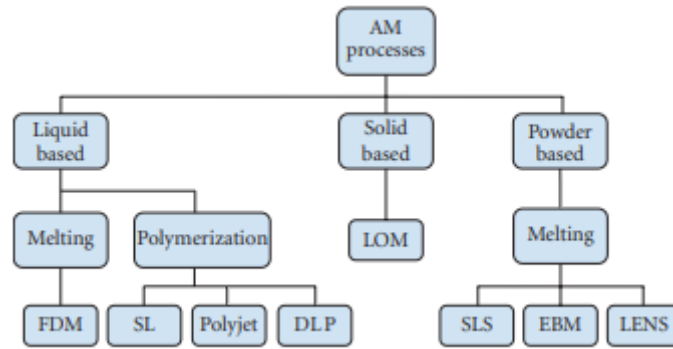


Figure 1.11 Existing 3D printing process and technologies (173).

developed in the 1980's, is rapid prototyping, which is the first form of creating layer by layer a 3D object starting from a computer-aided design (CAD) (171). Rapid prototyping technology was developed to have the possibility to create models faster, saving a lot of time with the possibility to test different prototypes, the same technology that today is called 3D printing (172). Additive manufactory processes can be divided in three categories that depends on the state of the material that is employed: it can be liquid, solid or powder based (173). From these three categories of the type of material used in the process, there are other sub-categories of 3D printing technologies (see Figure 1.11 (173)). These 3D printing technologies can be divided in fused deposition modeling (FDM), stereolithography (SL), polyjet, digital light processing (DLP), laminated object manufacturing (LOM), selective laser sintering (SLS), electron beam melting (EBM) and laminate engineering net shaping (LENS). The 3D printing process for almost all the cited technologies starts with a model in a CAD software, which is translated to a STL file, then the object is “cut in slices” containing the information for each layer. The thickness of each layer as well as the resolution and printing times depend on the equipment used.

Fused deposition modelling (FDM), is a liquid-based additive manufacturing process in which a thin polymeric filament is melted through a print head and extruded, on a building platform, with a thickness typically of 250 μm . The most common used materials for this kind of technology are thermoplastic polymer such as polycarbonate (PC), acrylonitrile butadiene styrene (ABS), polyphenylsulfone (PPSF), PC-ABS blends, and PC-ISO (171). The main advantages are that no post-processing is required and the low cost of machines and materials (172, 174). Drawbacks are the poor definition along the z axis (250 μm) and the long times required to print complex structures (175).

Stereolithography (SL), is a liquid-based process that consists in the photo-curing of a photosensible resin by means of a scanning laser. The laser can be in the UV or visible range depending on the type of photoinitiator used in the photosensible resin. The resin is loaded in a tray containing a moving platform, then the laser scans the resin solidifying specific locations each layer. When a layer is done, the platform is lowered and a new layer is scanned until the last one (172-174). The basic principle of this process is photo-polymerization, which is the

process where a monomer containing reactive groups can react through a polymerization process when irradiated with a light with a specific wavelength (176). This process will be explained in detail in the next section.

Polyjet, is an AM technique that uses an inkjet head moving in the x-y direction and depositing a photopolymer that is cured by an ultraviolet lamp. The z resolution of this technique is around 16 μm , which allows the production of parts with a good quality (177).

Digital light processing (DLP) technology, which will be discussed more in detail in section 1.4.3, uses a process that is similar to SL, with the main difference that, instead of using a laser with a galvanometric head to cure point-by-point the resin, it projects the x-y section of the object on the resin layer by layer. This method allows a faster printing because of the simultaneous polymerization of the resin on each layer. Moreover, the building platform and the growing object are moving upwards, out of the resin bath, resulting in a cleaner process and allowing for the building of larger objects (178).

Laminated object manufacturing (LOM), is a process in which the starting material is a laminated solid that is cut by a laser that is able to move in three dimensions. The advantages are the low cost, no post processing, no deformation or phase change during the process and the possibility to build large parts. The disadvantages are that the excess material is wasted, the low surface definition, the material is directional and complex internal cavities are very difficult to be built. This process can be used for models with papers, composites, and metals (179).

Selective laser sintering (SLS), is a technology that employs a powder that is sintered or fused by a laser beam. The chamber is heated at a temperature close to the melting point of the powder to increase the efficiency of the process and reduce the printing times. This technique is very similar to SL for what regards the equipment, but in this case, instead of polymerizing the resin, the laser partly melts few powder particles point-by-point attaching them to form a solid structure. This process offers a great variety of materials that could be used: plastics, metals, combination of metals, combinations of metals and polymers, and combinations of metals and ceramics. The disadvantages of this process are that the accuracy is limited by the size of the powder's particles, the process is executed in an inert gas atmosphere to avoid particle oxidation and continue heating is required, with high energy expenditure (180).

Electro-beam melting (EBM), is a technology similar to SLS, but in this case, the powder is melted by a high voltage electron beam, usually 30 to 60 kV. The process is very complex since it needs high vacuum to actually allow having an electron beam path of the order of tens of cm (181).

Laser engineered net shaping (LENS), is an additive manufacturing process where a metal powder is injected in a desirable location and is melted by a high-power laser beam. The process is carried out in an inert atmosphere to avoid oxidation processes. A high variety of metals and combination of them can be used with this technique, such as stainless steel, nickel based alloys, titanium-6 aluminium-4 vanadium, tooling steel and copper alloys (182).

1.4.2 Introduction to photopolymerization

In the following chapters, DLP technology will be employed for the 3D printing processes. For this kind of technique, photosensitive-polymer-based liquid formulations that respond to an external light stimulus by changing their physical, chemical and mechanical properties are studied. Photopolymerization is exploited to create covalently crosslinked solid structures by exposing a photosensitive system composed of a monomer, a photoinitiator and other additives like dyes or functional reagents to ultraviolet, visible or even infrared radiation (183, 184). Photopolymerization takes place when the radiation interacts with the light-sensitive photoinitiator that generates free radicals, highly reactive species, able to promote polymerization of reactive monomers to form crosslinked networks (185). Photopolymerization has several advantages, which include spatial and temporal control over polymerization, fast curing rates (few seconds) and minimal heat production (186). Disadvantages include relatively poor control over the crosslinking kinetic, oxygen inhibition, presence of unreacted monomer in the final polymer and generation of heterogeneities within the polymer network, due to random chain polymerization (187-189). Figure 1.12 (190) represent schematically the free radical reaction, starting from two unreacted monomers that bind together through a chain reaction with the free radical species generated by the photoinitiator. Different types of photoinitiators exist depending on the mechanism

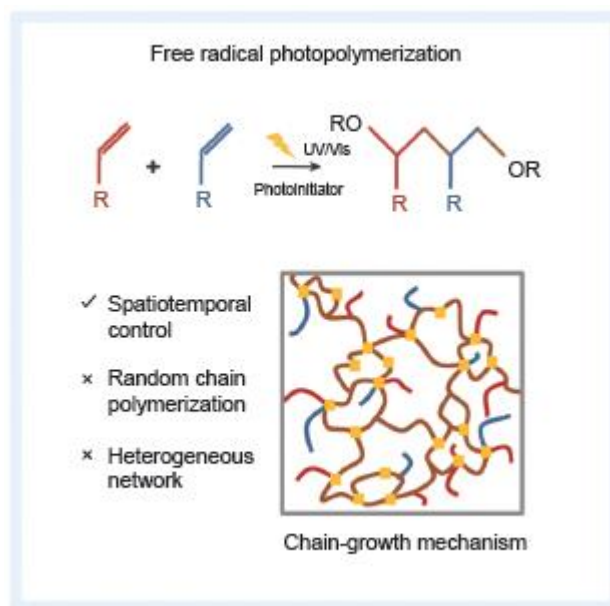


Figure 1.12 Scheme of the free radical polymerization mechanism (190).

involved in photolysis, including radical photopolymerization through photocleavage, hydrogen abstraction and cationic photopolymerization (185, 186, 191). Radical photopolymerization by photocleavage is a process in which the photoinitiator undergoes cleavage at C-C, C-Cl, C-O or C-S bonds to form radicals when irradiated with light. These photoinitiators include aromatic carbonyl compounds such as benzoin derivatives, benziketals, acetophenone derivatives, and

hydroxyalkylphenones (192-194). Radical photopolymerization by hydrogen abstraction, instead, uses photoinitiators that undergo hydrogen abstraction from an H-donor molecule, generating a ketyl radical and a donor radical (195).

1.4.3 Digital light processing technology

Digital light processing (DLP) technology, as mentioned in section 1.4.1, is a type of additive manufacturing that uses photosensible liquid formulations as starting materials to build three-dimensional solid structure through photopolymerization. Figure 1.13 (196) shows the sketch of the section of the DLP apparatus. The most important features of the machine, which characterize this

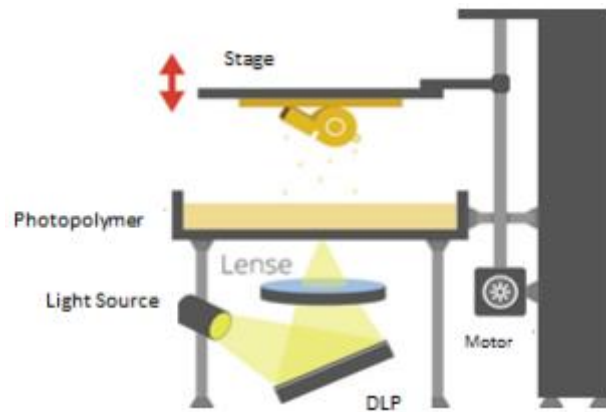


Figure 1.13 DLP 3D printing technology working principle (196).

technology, are the projector, the vat, the moving stage and the photosensible resin. In fact, the printing is carried out by irradiating the resin with a projector that photopolymerize it layer by layer, through a transparent vat on an upwards-moving platform, until the total construction of the object is done.

The whole process consists of three phases: CAD and STL files creation, printing and post printing. First, the ideal object is designed with a specific CAD software to give the desired 3D shapes, then the CAD is converted in a STL file, that is sent to the 3D printer. Now, the 3D printer software slices the STL three-dimensional file in a number of layers that is equal to the total height of the object divided by the desired thickness of each layer. At this moment, the user can enter the values of the printing parameters that usually are the time of exposure of the first layers, the time of exposure of the remaining layers and the velocity of approaching and leaving of the building platform. Once the process parameters are set, the printing can start and the lamp projects the exact image of the cross-section of the object at each layer. The bottom of the vat is transparent so that the light can pass through and polymerizes the resin only where is illuminated. The projector illuminates the resin for the time set and, subsequently, the platform moves up ready to polymerize the next layer. The process continues until all the layers of the object are polymerized. When the printing process is finished, the object is usually washed with a solvent, which is compatible with the material used for the printing and a post-curing is performed to further polymerize the object if needed.

The photosensitive resin is one of the most important part of this process, it is made of different ingredients that play a role in the printing process. A monomer is used to generate the body of the formulation and it consists in a simple molecule provided with functional groups able to create a crosslinked polymer. A photoinitiator is added to react with the light and start the free-radical reaction. A dye is mixed in the formulation to confine the light penetration, reducing light scattering, over-polymerization of the resin and increasing the x-y printing resolution. Finally, different additives can be inserted in the resin to give it specific functionalities, paying attention to choose the materials to be compatible with the other elements present in the formulation.

This technique has many advantages compared to other technologies that uses photopolymerization, such as SL and polyjet. In fact, the process is simple and clean, it gives high resolution objects, the printing is very fast due to the simultaneous polymerization of each layer and the cost of the equipment is contained. The drawback is the necessity of a post-processing of the final object.

1.4.4 DLP 3D printing with smart dyes

DLP 3D printing technology, as already mentioned, uses polymer-based resins that usually contain a dye to improve the light spatial confinement and avoid undesired over-curing effects during the printing process (197). The dye has the principal role to give a final coloring to the resin and, generally, no additional features are required. Nevertheless, some studies proposed an alternative approach, where functionalities (in most of the cases, light-responsive) are provided to the dye. With this method the dye assumes a bivalent role, it is still useful for the light confinement, but also acts as a functional filler for specific applications.

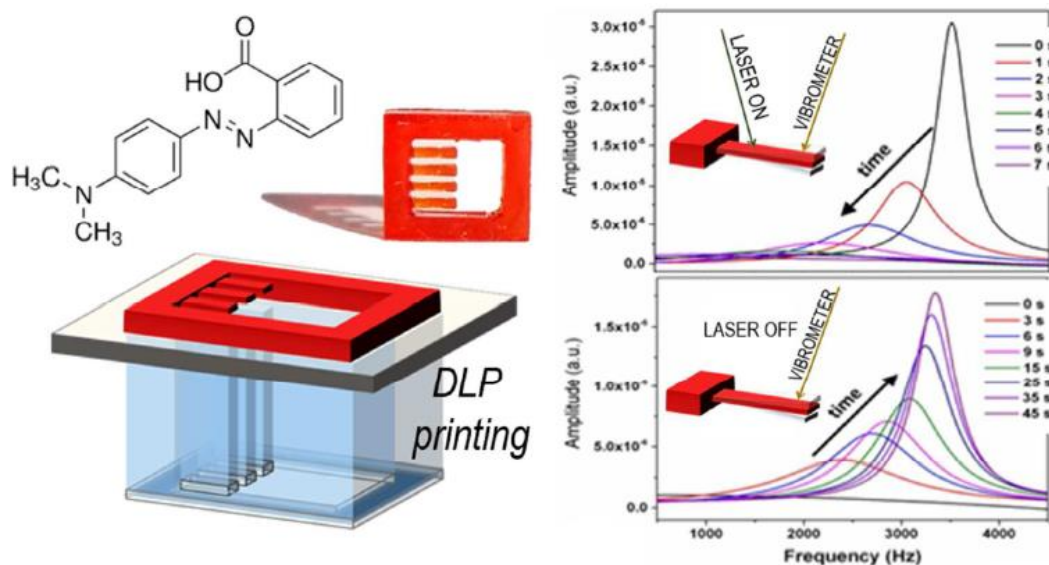


Figure 1.14 3D printed microcantilevers containing light triggered azobenzene moieties able to modify the mechanical properties. In the plots on the right, variation of the resonance frequency under laser illumination (178).

To this regard, Roppolo et al. (178) provided a study on photo-curable polymers for 3D printing containing azobenzene moieties providing photo-mechanical responsivity. In particular two monomers were chosen as bulk material, such as Bisphenol A ethoxylate diacrylate (BEDA) and Bisphenol A ethoxylate dimethacrylate (BEMA), consisting mainly in a rigid and more rubbery materials respectively, while Methly Red and disperse red methacrylate were used as azobenzene moieties. Flat specimens were 3D printed and their mechanical properties were analyzed by means of tensile stress tests during light irradiation exposure. The results showed an expansion of the sample and the decrease of the elastic constant under laser irradiation and a recovery of both properties as the laser was switched off. Moreover, microcantilevers were 3D printed and their resonance frequency calculated under laser irradiation. Results showed a reversible adjustment of the peak of resonance frequency as the cantilevers were irradiated, brought by modified the mechanical properties (see Figure 1.14).

Another study was conducted by Frascella et al. (198) on DLP 3D printing of formulations containing smart dyes. In particular, they 3D printed a photo-curable

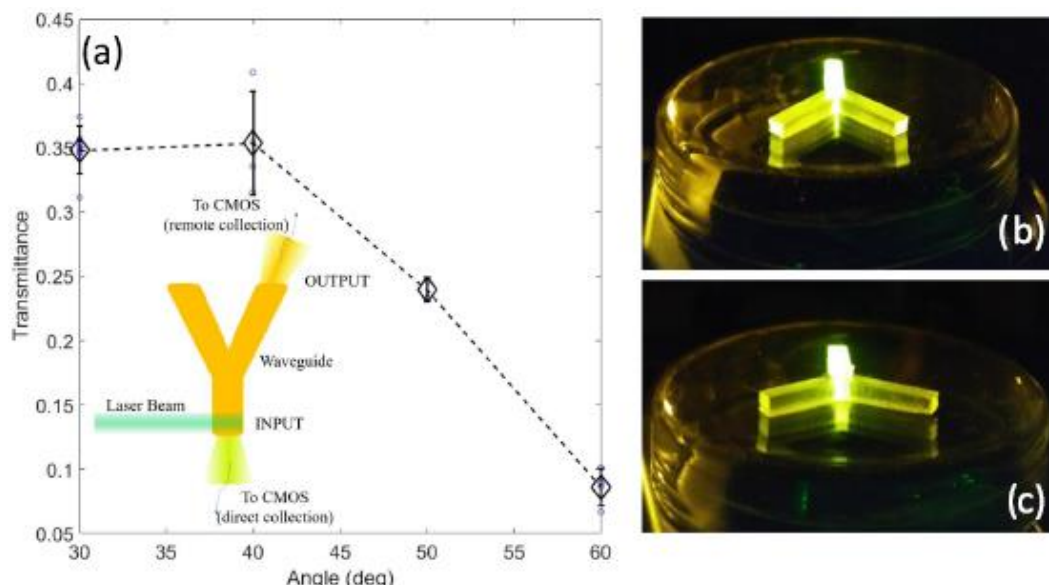


Figure 1.15 (a) Transmittance through a branch of the Y-shaped waveguide versus aperture angle α . (b, c) Fluorescence pictures of the 3D printed waveguides illuminated at one end of the waveguide (198).

polymer containing a photoluminescent dye enabling the creation of waveguides. Bisphenol A ethoxylate (2 EO/phenol) diacrylate (M_w 572, BEDA) was used as constitutive monomer, while the dye employed was an amino derivative of 7-nitrobenz-2-oxa-1,3-diazole (NBD), which has been functionalized with a methacrylic double bond. The dye possesses very adequate absorption and emission properties, with a charge transfer (CT) intense absorption band in the red region ($\lambda_{abs} = 440-475$ nm) and an intense fluorescence emission in the yellow-green region ($\lambda_{em} = 497-526$ nm). Furthermore, it was used for its methacrylic group, which is fundamental as it can copolymerize with the bulk monomer becoming a perfect material for DLP 3D printing process. They successfully 3D printed

different waveguide-like structures and tested them to the fluorescence microscope to characterize the optical performances. Results showed that the 3D printed optical devices were able to guide the luminescence of the dye up to an angle of 40° (see Figure 1.15).

In this context, Chapter 2 will describe in detail the study published in Gillono et al. on CO_2 permeability control in light-triggered 3D printable structures, where azobenzene moieties were incorporated in photo-curable resins to create a 3D printed device able to photo-control the CO_2 transmission rate.

1.4.5 Ionic liquids and poly ionic liquids in DLP 3D printing

PILs have been employed in numerous research as additive or primary functional active material in 3D printing. Due to the near-infinite choice of anion and cation, the reciprocal behaviour between PILs and other additives can be tuned. In fact, the high potential of PILs in 3D printing is the possibility to incorporate a wide spectrum of different physical and chemical properties in a solid structure that can be previously designed. PILs can be synthetically created and the incorporation of the cationic and ionic species in the polymer backbones results in the construction of different polyionic structures. Furthermore, DLP 3D printing offers the

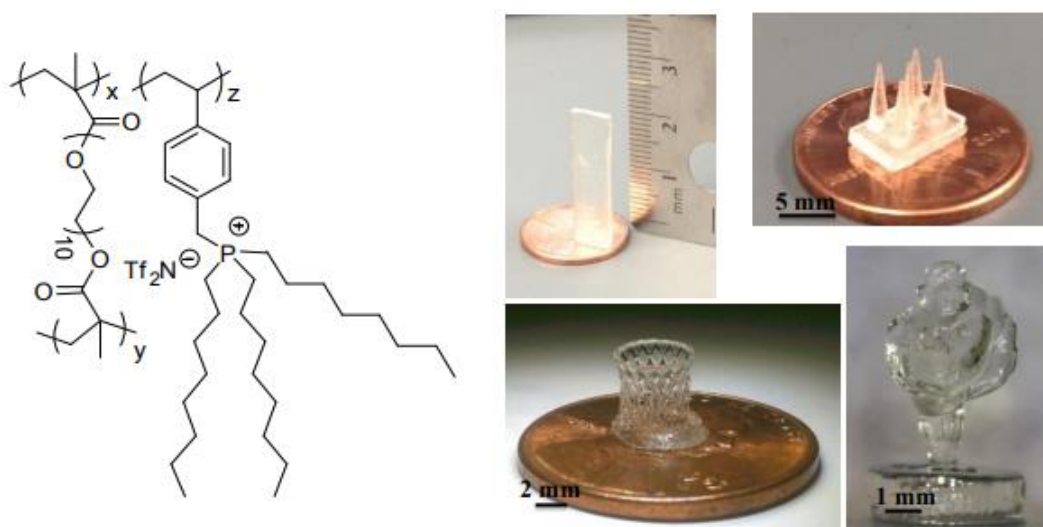


Figure 1.16 3D printed poly(PEGDMA-coTOPTf₂N) objects by mask projection micro-stereolithography (199).

possibility to start from a liquid formulation as a blend of monomers and additives and create a crosslinked polymer, which incorporates specific functionalities. The first example of 3D printed PILs comes in 2014 from Schultz et al (199), where they 3D printed phosphonium-based PILs with poly(ethylene glycol) dimethacrylate (PEGDMA) as crosslinker by mask projection micro-stereolithography (see Figure 1.16). They obtained object with high resolution possessing high thermal stability, tunable glass transition temperature (by modifying the ILs contents ratio), optical clarity and ion conductivity.

In another study, Lee et al (200). reported the successful 3D printing of IL/polymer (1-ethyl-3-methyl-imidazolium tetrafluoroborate, [emim][BF4]/2-[[butylamino)carbonyl]oxy]ethyl acrylate, BACOE) composites with different degrees of crosslinking and polymerization as materials for piezoresistive tactile sensors. The degree of crosslinking and polymerization was controlled by the

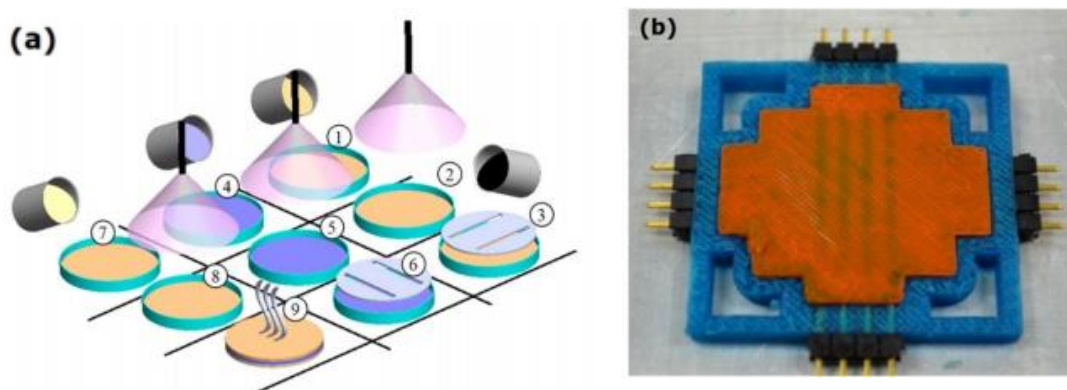


Figure 1.17 (a) Sensor fabrication and (b) sensor's architecture made by 3D printing of [emim][BF4]/BACOE) composites (200).

acrylic-based crosslinking agent concentration and the UV exposure time. Figure 1.17 shows the printing process and the sensors architecture.

Recently, Wales et al (201). conducted a study on vinyl-substituted imidazolium-based PILs used to stabilize novel photoactive hybrids organic-inorganic polyoxometalates (POMs). The POM/PIL mixtures were then 3D printed by DLP technique. Two IL monomers were employed in the study based on 1-butyl-3-methylimidazolium cation (C4vim) and bis(trifluoromethane sulfonyl)imide

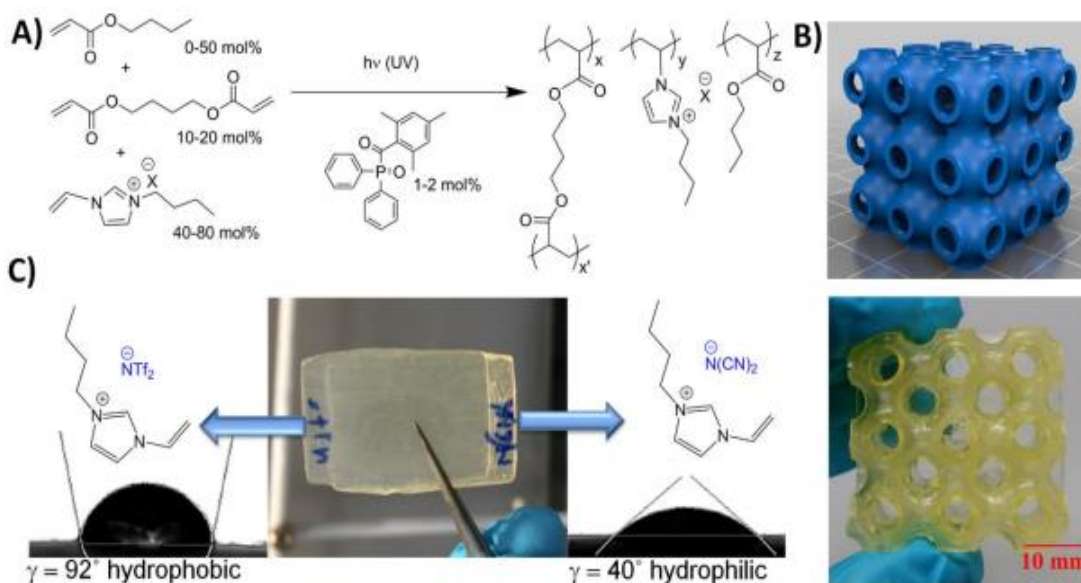


Figure 1.18 (a) Formulation composition and photo-curing process. (b) Examples of PIL-based 3D printed complex geometry. (c) Multifunctional printing of hydrophilic and hydrophobic PILs (201).

(TFSI) and dicyanamide ($\text{N}(\text{CN})_2$) to give hydrophobic and hydrophilic nature to the PILs. A complex 3D hollow cube composed by repeating Schwarz P minimal surfaces was successfully 3D printed (see figure 1.18), demonstrating the high potential of DLP 3D printing with this kind of materials.

1.5 Goals of the research

Considering the importance of CO_2 management (as introduced in the previous paragraphs) and of the materials able to interact with CO_2 for the world of the future, this thesis aims to develop polymeric materials for this specific purpose. Furthermore, the goal is to synthesize materials which could be processable with 3D printing, since this technology allows for a high degree of complexity and automatization.

In this context, we explored different type of material for CO_2 interaction, in particular:

- The stimuli-controlled permeability of polymeric membranes (chapter 2).
- The development of materials for CO_2 capture (Chapter 3 and 4).

To achieve our goals, different strategies were followed, in detail:

- The examination of a possible and interesting stimulus for permeability control (in our case light).
- The study of light-sensitive molecules which can lead to photo-triggered permeability.
- The development of 3D printable materials with these features and characterize them
- The realization and fabrication of a suitable device which can exploit photocontrollable CO_2 permeation.

Regarding CO_2 capture:

- The investigation of suitable strategies for CO_2 capture (in our case introduction of ionic liquids).
- The study and optimization of the 3D printing process in presence of commercially available ionic liquids and polymerizable ionic liquids.
- The study of the interaction of CO_2 with these materials.
- The synthesis of more efficient ionic liquids for CO_2 capture.
- The 3D printing and characterization of these materials.

Chapter 2

CO₂ permeability control in 3D printed light responsive structures

1.1 Introduction

Stimuli-responsive materials have become of great interest due to their multiple possible applications. These materials can change their intrinsic properties reversibly or irreversibly by an external excitation. The stimulus can come from a special chemical environment, like a different pH (202, 203), the presence of a solvent (204, 205), guest molecules (206) or from a change in temperature (207, 208), pressure (209), magnetic field (210) and light excitation (211). In the view of gas separation's technology, smart membranes with controllable permeability are among the most demanding technology in many fields (212-215) and light-responsive polymer membranes are of increasing importance (130, 216). In this background, as already described in Chapter 1, polymers functionalized with azo-benzene chromophores are among the most considered in many research related to photo-functional materials, due to their adaptable applications in many fields such as biotechnology (217, 218), optics (219) and nanotechnology (178, 220).

This chapter, that in part describes the work early published in Gillono et al. (221), presents a study on polymeric materials containing light-triggered azo-chromophores, allowing the control of CO₂ permeability, following the work carried out by Kameda et al. (128) and Bujak et al. (129), attempting to respond the increasing request of technologies for carbon capture and storage (CCS). Poly(ethylene glycol)diacrylate (PEGDA) was chosen as constituent bulk monomer as it is a well-known material for DLP 3D printing technology. Furthermore, it is a good material related to the use of carbon dioxide gas, because of its affinity to the CO₂ molecule due to the presence of polar backbones (222, 223). Formulations containing PEGDA, a photo-initiator (BAPO) and two different azo-benzene chromophores, acting as well as a dye, were prepared and photo-crosslinked to create a thin membrane. The chromophore chosen are a typical azo-benzene dye with a monocarboxylic acid with a tertiary amine substitution (Methly Red, MR) and an azo-benzene with a methacrylate group (Disperse Red 1 Methacrylate, DR1M) capable of participating in the polymerization reaction and linking to the polymer matrix. These formulations containing chromophores, able to respond to external light excitation, were prepared precisely to be photo-curable and 3D printable. Thus, it was possible to extend the application not only to the fabrication

of simple membranes by casting, but also to more complex structures with a precise design that can be exploited to achieve specific targets. In fact, with 3D printing technology it is possible to obtain object with a customized design starting from a computer aid design (CAD) file. This cost-effective and timesaving approach, merged with the use of smart materials, can be a powerful tool that allows the direct production of devices for specific applications(224, 225). For this work, a DLP 3D printer was used because of its suitable technology, which was already described in Chapter 1, which allows to create solid structures starting from a liquid formulation that can contain basic ingredients like the photoinitiator and a dye, but also specific functional additives. Nevertheless, in this case, the photochromic azo molecules have a double purpose, acting as a dye due to their light absorption capability and as a functional additive due to their photo-switching properties. In fact, it will be shown how the azo chromophores were exploited as photo-functional agent to control the intrinsic permeability of the polymer membranes. Furthermore, a series of characterizations were done in order to study the materials in their multiple aspects. First, a polymerization study on the prepared formulations will be presented, to fully understand their reactivity upon irradiation. Secondly, it will be shown the chemical/physical characterization, aiming to investigate mainly the optical and thermal properties of the photo-cured formulations. Then, results on CO₂ permeability tests will be given to analyze the effect of the nanoscale-photo-switching on the macroscale, by investigating the gas transmission rate through the photo-polymerized membranes during irradiation. Finally, a 3D printed working device for the photo-control of pH in a water solution will be shown, as a proof of concept of the described effect, to demonstrate the integration of those materials in smart devices.

1.2 Experimental and methods

1.2.1 Materials

The monomer used as bulk material for the membranes and the 3D printed structures was Poly(ethylene glycol) diacrylate (PEGDA) with average molecular weight 575. Phenylbis(2,4,6-trimethylbenzoyl)phosphine oxide (OMNIRAD 819) powder with 97% purity was used as photo-initiator. Two chromophores were adopted in the experiments, 2-[[4-(dimethylamino)phenyl]diazenyl]benzoic acid (Methyl Red, MR), 2-[N-ethyl-4-[(4-nitrophenyl)diazenyl]anilino]ethyl 2-methylprop-2-enoate (Disperse Red 1 Methacrylate, DR1M). PEGDA, MR and DR1M were purchased from Merck. The photoinitiator OMNIRAD 819 was purchased from IGM Resin. Brilliant green, dye content ~ 90% was purchased from Sigma Aldrich.

1.2.2 Formulations and sample preparation

The formulations were prepared with the aim to be processed in a DLP 3D printer; therefore, mixtures containing PEGDA, the photo-initiator and a chromophore dye were created. The different additives were added per hundred resin (%wt) with respect the total amount of PEGDA used, with the following ratio:

- MR and DR1M: 0.2 %wt
- Photo-initiator: 2 %wt

The photoinitiator was solubilized in acetone ~ 2.5 ml/g and sonicated for 5 minutes. In the meantime, the photochromic dye was mixed with PEGDA in a dark coated vial and sonicated for 30 minutes. Subsequently, the solubilized photoinitiator was poured in the vial and sonicated for further 15 minutes. The first analysis on the photo-cured formulations were carried out on polymerized membranes directly produced by 3D printing. The 3D printer used was a 3DLPrinterHD 2.0 (Robot Factory) (see Figure 2.1a), equipped with a projector with a resolution of $50 \mu\text{m}$

	3DLPrinter-HD 2.0	Pico Plus 39
	a 	b 
Brand	Robot Factory	Asiga
Wavelength	400-780 nm	405 nm
Intensity	12 mW/cm^2	22 mW/cm^2
Resolution	$50 \mu\text{m}$	$39 \mu\text{m}$
Layers thickness	$100\text{-}10 \mu\text{m}$	$100\text{-}1 \mu\text{m}$
Building tray	Fluorurated polymer	Siligel

Figure 2.1 DLP 3D printers employed for the samples printing, (a) Robot Factory and (b) Asiga and their main working parameters.

(1920×480 1080 pixels). The building area of the moving platform is 100×56.25

x 150 mm with a vertical resolution of 10 μm , the layer thickness can be adjustable up to a maximum of 100 μm . In this case, it was decided to set it to 25 μm and multiple print tests were done in order to find the right exposure times. The parameters were chosen in order to have a good tradeoff between fragility and complete polymerization of the membrane. In the end, the optimal exposure times for the formulations containing MR and DR1M were 7 s and 5 s respectively. It was found out that membranes were self-standing and suitable to handle with a thickness greater than 150 μm , that means more than six layers of printing. The obtained membranes were carefully washed in ethanol and a post curing process was performed with an ultraviolet medium-pressure mercury lamp also provided by Robot Factory. The post curing process was carried out for a time duration of 1 minute in order to reduce the photo bleaching of the chromophore. In the next subsection it will be explained the methods and instrumentations used for the membrane's characterizations.

The second part related to 3D printing, was the creation of a prototype integrating the photo-functional azobenzene-based polymer in form of a membrane for the control of CO_2 permeability. The prototype's structure was 3D printed, with a DLP Asiga Freeform 3D printer with native XY pixel resolutions down to 27 μm and 250 nm Z-axis servo resolution (see figure 2.1 b), using two different formulations: one containing the photo-sensible dye (MR) and the other containing a semi laser-transparent green dye (Brilliant Green), which at 532 nm has an absorbance of 8.8% of the maximum peak of absorbance at 625 nm. In order to build the structure in one single shot using simultaneously the two formulations, the 3D printing process was made in two stages by pausing the printing and changing formulation. The final object was a structure made by two different functional resins, 3D printed in one process.

1.2.3 Material characterization

Real-time rheological measurements were performed using an Anton Paar rheometer (Physica MCR 302) in parallel plate mode with a Hamamatsu LC8 visible lamp with power intensity of 10 mW/cm^2 (10% of maximum) and a cut-off filter below 400 nm equipped with 8 mm light guide. The gap between the rotating plates was set to 100 μm ; for all the measurements, the temperature was fixed at 25 $^\circ\text{C}$, at constant shear frequency of 3.18 rad/s at 1% of amplitude, which was set based on the amplitude sweep test indicating, at a certain frequency, the linear viscoelastic region. The lamp was turned on after a waiting time of one minute in order to leave enough time to have a stable signal. The outcome data consist in a plot of the elastic (G') and loss (G'') modulus and their ratio versus time. Another method used to study the reactivity of a photo-curable formulations is infrared spectroscopy. This technique allows to follow the conversion of the reactive groups of the monomer, in this case the acrylic group of PEGDA, by evaluating the extent of decrease of the peak relative to C=C bond due to the free radical polymerization reaction. For these measurements, ATR spectra were generated using a Tensor 27

FTIR Spectrometer (Bruker) equipped with ATR tool, 32 scans were collected with a resolution of 4 cm^{-1} from 4000 to 400 cm^{-1} . Light absorption of the samples was evaluated by means of UV-visible spectroscopy. The UV-visible spectra were collected with a Varian Cary-500 spectrophotometer in the range between 300 nm and 800 nm , with a resolution of 1 nm , monitored with a scan rate of 480 nm/min . Afterwards, DMTA analysis were performed on a Triton Technology TTDMA to investigate the thermo-mechanical properties of the polymerized formulations containing the two azo chromophores. With this analysis it was possible to follow the elastic modulus and the loss modulus of the sample at different temperatures in order to identify phase transitions of the material, in this case the glass transition temperature (T_g). The samples were 3D printed in a rectangular shape ($30 \times 5 \times 0.15\text{ mm}$). The oscillation was set with a displacement of $20\text{ }\mu\text{m}$ at a constant frequency of 1 Hz . For the same purpose, DSC analysis were executed with a Netzsch DSC 204 F1 Phoenix instrument on the polymerized samples to investigate the thermodynamic transition of the materials by varying the temperature. In this case, rather than mechanically, the phase transitions are identified by measuring the calorimetric profile of the samples. As final characterization, contact angle measurements were carried out on the 3D printed membranes containing the two azo molecules. Contact angle measurements were performed with a Krüss DSA10 instrument, equipped with a video camera. After the physical/chemical characterizations, the membranes were tested to analyze their barrier properties to CO_2 and other gases (O_2). This was done to verify what was the permeability behavior of the membranes using different gases having different properties, such as kinetic diameter and polarity. The transmission rate of CO_2 through the membranes containing the two different chromophores in dark condition (with LASER turned off) and different temperatures and relative humidity will be presented. The measurements were carried out with a Multiperm Extrasolution analyzer. The instrument is composed of an upper chamber where the CO_2 is injected and a lower chamber where a gas carrier (nitrogen) flows and transports the permeated gas to an infrared sensor, the two chambers are separated by the membrane sample. Both in the upper chamber and lower chamber the two gases flow at a constant rate and, throughout all the process, their concentrations are 100% CO_2 in the upper chamber and 100% N_2 in the lower chamber. The concentration gradient of CO_2 between the two chambers leads to an osmotic pressure and a diffusion flow from the upper to the lower chamber. The permeability of the membrane, which is an intrinsic property of the material, is proportional to the transmission rate of the gas in the lower chamber, which is strictly linked to the membrane thickness. The calculation of the gas transport parameters is reported below.

Moreover, the same instrument was used to perform dynamic permeability analyses under illumination, to investigate the effect of chromophore photo switching on the gas transport properties of the printed membranes. Together with these measurements, analysis on the influence of LASER beam on the increase of the membrane temperature were carried out. In particular, photo-DSC and infrared

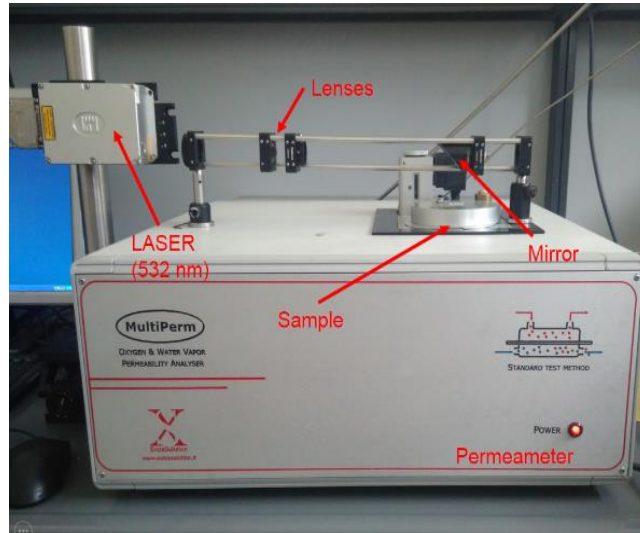


Figure 2.2 Permeability measurement apparatus with LASER and optical setup.

thermometer measurements during LASER irradiation were performed. Furthermore, a study on the permeability variation related to different LASER intensities was done to better understand the permeability behavior of the membrane in response of a lower or higher excitation of the chromophores. The measurements performed under illumination required a LASER apparatus able to focalize the light beam on the sample, through the lid, inside the measurement chamber. Figure 2.2 shows the permeability analyzer and the laser apparatus used to measure the gas permeability during illumination. The laser used was a collimated, CW doubled Nd:Yag laser ($\lambda = 532 \text{ nm}$) with tunable power from 0 to 250 mW. The optic equipment consists of two lenses to defocus and collimate the LASER beam and a mirror to deflect it by 90° onto the membrane. The laser path irradiates the sample crossing the chamber lid through a quartz window with a consequent attenuation of about 25% of the initial power. The membranes, before the measurement, were tightly inserted in an aluminum reduction mask in order to easily adapt them to the dimension of the measurement chamber. The area of the final membrane exposed to the gas was 2.01 cm^2 and the lenses were adjusted in order to have the LASER spot at that exact dimension. The instrument, during the measurement, generates a transmission rate plot, and finally stops when the curve reaches a plateau, indicating the value of maximum transmission rate. From the transmission rate curve, it is possible to obtain three more relevant gas transport parameters, such as permeability, diffusivity and solubility. In gas and vapor systems, the rate of diffusing molecule transfer indicates the quantity of gas that crosses the membrane per unit area and time and it is expressed in terms of vapor pressures, ρ_1 and ρ_2 , at steady state, by the following equation:

$$J_{ss} = \frac{P(\rho_1 - \rho_2)}{l} \quad (1)$$

Where P is the permeability and l the membrane thickness.
The permeability can therefore be evaluated as follows:

$$P = \frac{J_{ss}l}{\Delta p} \quad (2)$$

The diffusion coefficient were calculated with the time lag method assuming a constant diffusion coefficient. From second Fick's law of diffusion it is possible to extrapolate the amount of diffusing molecules (Q_t) which passes through the membrane at time t , as shown in the following equation:

$$\frac{Q_t}{lC_1} = \frac{Dt}{l^2} - \frac{1}{6} - \frac{2}{\pi^2} \sum_{n=1}^{\infty} \frac{(-1)^n}{n^2} \exp\left(\frac{-Dn^2\pi^2t}{l^2}\right) \quad (3)$$

Where C_1 is the concentration of gas in the upstream chamber and D is the diffusion coefficient.

As steady state is approached ($t \rightarrow \infty$), the exponential term becomes negligibly small, allowing for extrapolating Q_t versus t :

$$Q_t = \frac{DC_1}{l} \cdot \left(t - \frac{l^2}{6D}\right) \quad (4)$$

The intercept τ on the t -axis is given by:

$$\tau = \frac{l^2}{6D} \quad (5)$$

Thus, the diffusion coefficient can be calculated from equation (5):

$$D = \frac{l^2}{6\tau} \quad (6)$$

The solubility of the gas in the membrane can be finally evaluated, from P and D , as follow:

$$S = \frac{P}{D} \quad (7)$$

Once the transport parameters were calculated in each condition of temperature, relative humidity and light excitation, it was decided to find an application, involving 3D printing, by creating a working device (equipment and process description can be find in section 1.2.2) based on the effect explained in this chapter, as a proof of concept.

1.3 Results and discussion

1.3.1 Polymerization study

The first characterization of the prepared formulations regards the study of their photo-polymerization properties. In particular, reaction time and kinetic of polymerization were investigated. The formulations, as already mentioned, are composed by a reactive monomer, which constitute the bulk of the mixture, the photo-initiator and the chromophore dye (either MR or DR1M). The amount of the photo-initiator (2 %wt) was chosen based upon past studies on photo-polymerization (226), whereas, for what regards the dyes, the right concentration was found to obtain the formulation with the optimal polymerization properties. In fact, in a 3D printing process, the dye is necessary in the formulation to achieve good resolution along the x-y axis due to reduced light scattering and along z-axis as well to reduced light penetration during illumination (and so the extent of polymerization) (178). Nevertheless, the amount of dye present in the formulation must be smartly decided, because high concentrations might increase too much the light adsorption reducing to critical limits the polymerization performances. To overcome this problem, formulations with four different concentrations of

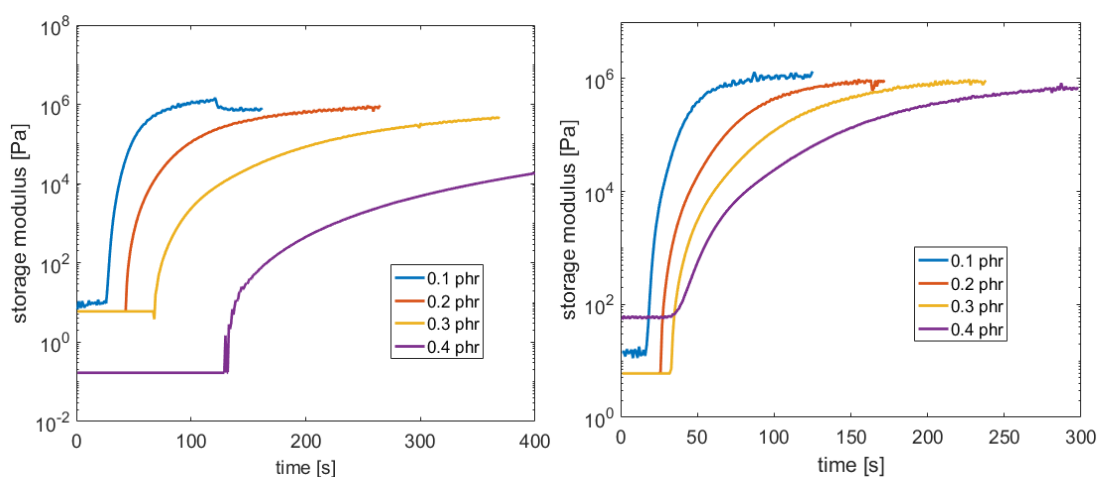


Figure 2.3 Photo rheology analysis of formulation containing 0.1, 0.2, 0.3 and 0.4 %wt of (a) MR and (b) DR1M.

photochromic dyes from 0.1 %wt to 0.4 %wt were tested to observe their different behaviors. Photo-rheology measurements were carried out on the different formulations to both understand the curing process and optimize the printing parameters. The expectations of the results are the following: an initial phase, when the formulation is liquid, where G'' is higher than G' , followed by an increase of the elastic modulus until it equals G'' , the so called gel point, and a continuous increase of G' until a plateau is reached, when the polymerization reaction finishes. The time elapsed from the start of the reaction until the formation of a plateau is related to the reaction kinetic of the formulations. Figure 2.3 shows the photo-rheology curves for MR and DR1M with concentrations from 0.1 to 0.4 %wt. As expected, for both the dyes, the polymerization process slows down as the concentration increases. This can be explained by the fact that the dye absorbs light, competing with the photo-initiator and, as the dye concentration increases, less light is absorbed from the photo-initiator, slowing down the reaction (197). This effect

can be seen by looking at the curves related to 0.2 and 0.3 %wt, where the abrupt increase of G' is delayed and the overall reaction is slower. On

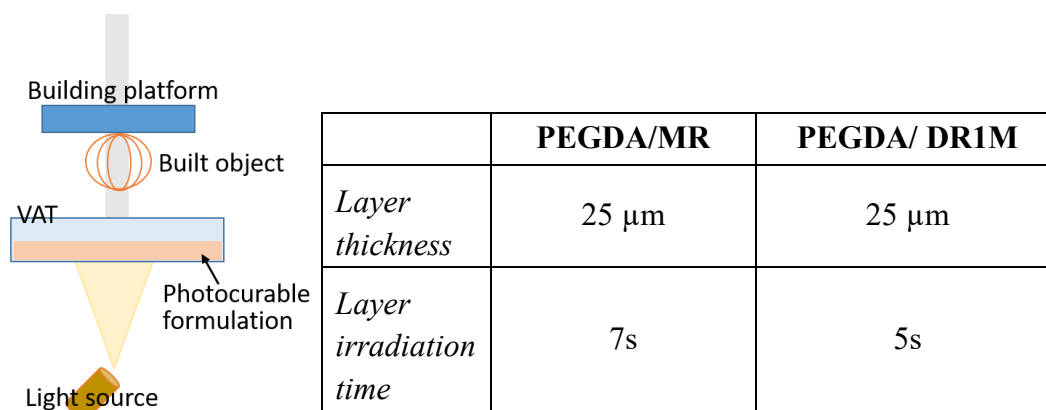


Figure 2.4 Scheme of the DLP equipment used and printing parameters adopted for the membranes containing the two different dyes.

the other hand, low concentrations of the dyes (0.1 %wt) bring to a very fast reaction, which can cause an over-polymerization of the resin and a consequent low printing definition. Therefore, a good tradeoff concentration value of 0.2 %wt was chosen for both dyes. In the rest of the chapter the samples containing both dyes with an amount of 0.2 %wt will be referred to as PEGDA/MR and PEGDA/DR1M. Once the right amount of the dye to be added to the formulations was decided, preliminary 3D printing tests were performed to find the optimal process parameters. Membranes with thickness ranging from 100 μm to 200 μm made of PEGDA/MR and PEGDA/DR1M were 3D printed using a DLP equipment. The printing parameters were adjusted to obtain self-standing and easy to handle samples (see process and printing parameters in figure 2.4).

Although photo-rheological measurement already gave a clear view of the kinetic of the polymerization reaction, it was decided to carry out further analysis on the reactivity of the two formulations. Fourier transform infrared (FTIR) spectroscopy analysis in attenuated total reflection (ATR) mode were performed on the liquid formulations and on the 3D printed membranes containing both dyes.

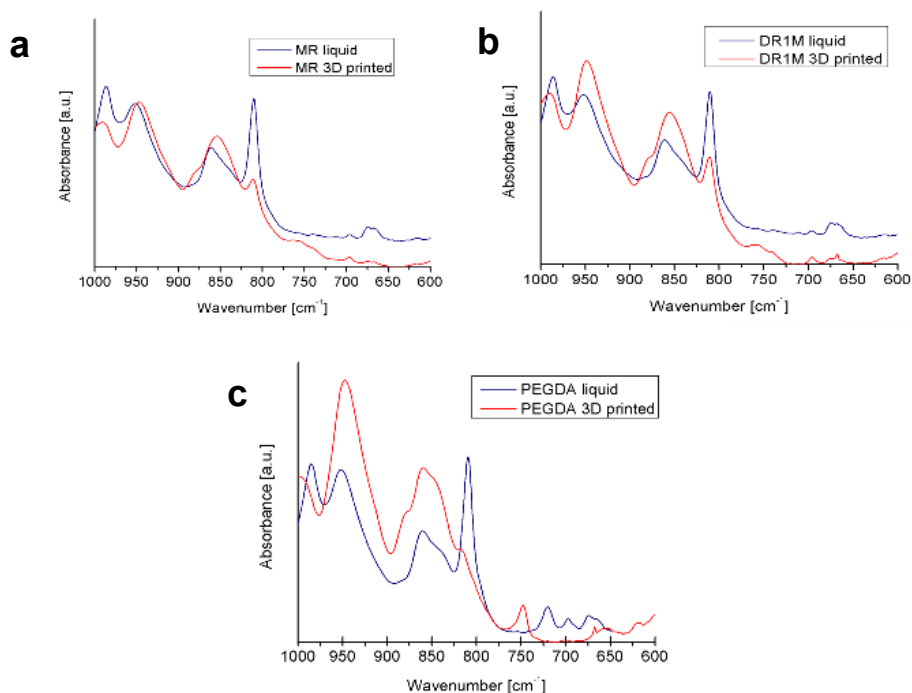


Figure 2.5 ATR FT-IR spectra of (a) PEGDA/MR, (b) of PEGDA/DR1M and (c) of neat PEGDA both in liquid and solid form, following the evolution of the peak at 810 cm^{-1} .

Particular attention was given to the C=C carbon double bond conversion of the acrylate group after photo-polymerization. Figure 2.5 shows the spectra of PEGDA/MR, PEGDA/DR1M and neat PEGDA before and after photo-polymerization. As shown in the figure, the peak in the band of 810 cm^{-1} , corresponding to the C=C carbon double bond of the acrylic group, was followed. In all the three cases, the peaks are still present in the liquid formulations, instead, the peaks lower down in the polymerized samples, indicating the conversion of the double bond in a single bond and the creation of covalent bonds in the polymer network. The full IR spectra from 4000 cm^{-1} to 600 cm^{-1} are reported in Figure A1 in Appendix A. The degree of conversion of the acrylic double bonds was calculated by evaluating the absorbance increment of the peak at 810 cm^{-1} normalized on the ester band at 1722 cm^{-1} of the samples before and after photopolymerization, using the following equation (227):

$$\text{Degree of conversion} = \frac{A(810)_0 - A(810)_t}{A(810)_0} \cdot 100 \quad (8)$$

Where $A(810)_0$ is the area of the peak at 810 cm^{-1} at time zero and $A(810)_t$ is the area of the peak at 810 cm^{-1} at time t. The degree of conversion of PEGDA/MR, PEGDA/DR1M and neat PEGDA was 91%, 92% and 97% respectively (All the main material properties are summarized in Table 2.1). From these results, it is possible to say that the presence of the dyes, still competing with the photo-

initiator, allows for a high double bond conversion, even if lower than the neat PEGDA.

1.3.2 Chemical and physical characterizations

The 3D printed samples of PEGDA/MR and PEGDA/DR1M were further characterized by means of UV-visible, DMTA, DSC and contact angle. UV-visible analysis was performed to check the photo-stability of the azo membranes after photo-polymerization. In fact, the dyes present in the formulations, during the printing process, are subject to direct light and can undergo photo bleaching. Figure 2.6 shows the absorption spectra of the sample PEGDA/MR and PEGDA/DR1M

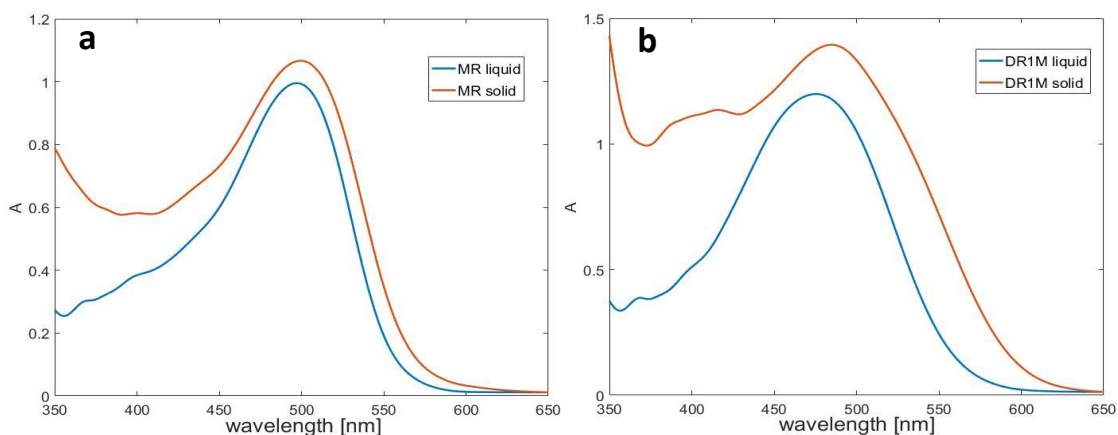


Figure 2.6 UV-visible spectra of (a) PEGDA/MR and (b) PEGDA/DR1M both in solid and liquid form.

in liquid and solid form from 350 nm to 650 nm. As shown in the spectra, both samples in liquid form present a peak centered at 475 nm, while, for the polymerized samples, the peaks broaden and slightly shift to higher wavelength. This effect can be due to the changing of the surrounding polymer chain structure after the photo-curing process. In case of DR1M, the shift is more remarked because the azo molecules are chemically bonded to the polymer chains, enhancing the effect. Besides that, the photochromic dyes did not experience degradation during light exposure. Finally, the shoulder around 400 nm was imputable to the presence of the photo-initiator. This analysis was also useful to know the absorption spectra of the polymerized samples in order to choose the proper emission wavelength of the laser that will be used to irradiate the membranes. For this reason, a laser with $\lambda = 532$ nm was adopted, that lies in the absorption peak of both dyes. After the study on the photo-stability of the membranes DMTA analysis were performed to investigate their thermo-mechanical properties. The 3D printed rectangular samples were tested in a temperature range from -70 °C to 10 °C with a heating rate of 3 °C/min. The curves of the elastic modulus (E'), loss modulus (E'') and tan delta for PEGDA/MR and PEGDA/DR1M and neat PEGDA samples are shown in Figure

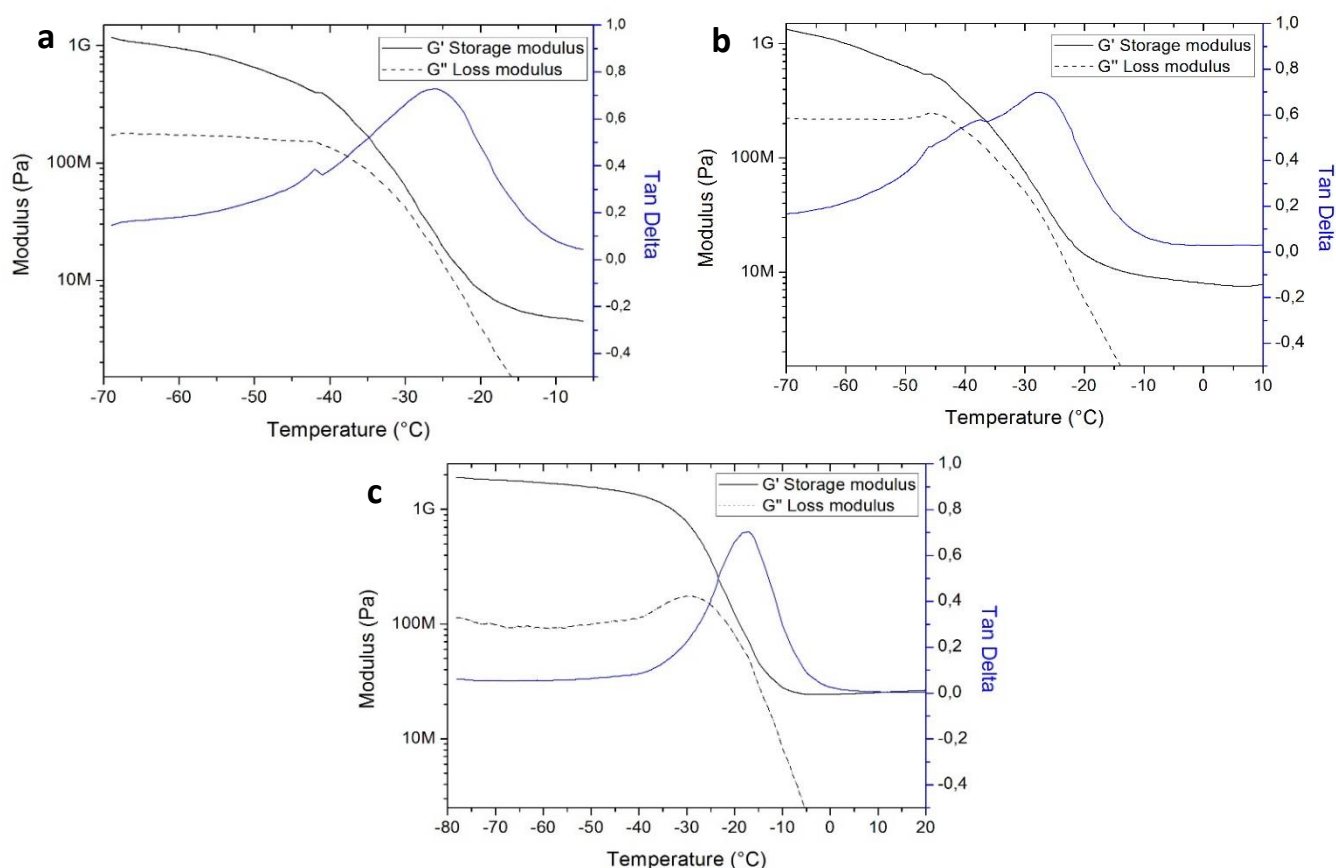


Figure 2.7 DMTA analysis displaying the elastic modulus, the loss modulus and the tan delta of the 3D printed samples containing (a) PEGDA/MR and (b) PEGDA/DR1M and (c) neat PEGDA.

2.7. The value of T_g was calculated by taking the temperature at the maximum of the tan delta, corresponding to the ratio between E'' and E' . As it can be seen from the curves, the T_g values for polymerized PEGDA/MR and PEGDA/DR1M lie around $-28\text{ }^\circ\text{C}$ and $-26\text{ }^\circ\text{C}$ respectively, while the value of T_g of neat PEGDA is about $-18\text{ }^\circ\text{C}$. All the main material properties are summarized in Table 2.1. This could be related to the lower double bond conversion with respect neat PEGDA, which induces a reduction of its glass transition temperature (228). This effect is more evident in PEGDA/MR rather than in PEGDA/DR1M, as expected, because the formation of a looser network leads to a lower crosslinking density. This result can be exploited, since the gas permeability is strictly linked to these properties, tending to increase as the crosslinking density decreases (229) (see Table 2.1). DSC analysis were also performed on the membranes containing both dyes, with heating rate of $10\text{ }^\circ\text{C}/\text{min}$ from $-70\text{ }^\circ\text{C}$ to $30\text{ }^\circ\text{C}$. From the curves (see fig. 2.8), T_g values were extrapolated as midpoint of the flexing point at around $-41.5\text{ }^\circ\text{C}$ and $-40\text{ }^\circ\text{C}$ for PEGDA/MR and PEGDA/DR1M respectively. These values are different with respect the ones obtained with DMTA because of the different measuring method, however the sample containing DR1M has a higher T_g than the one with MR, which is in accordance with the DMTA results. As last analysis, contact angle

measurements on the 3D printed membranes containing PEGDA/MR and PEGDA/DR1M were carried out to investigate their hydrophilicity. Membranes containing DR1M chromophore resulted more hydrophobic ($\theta_c = 110^\circ$) than the membrane containing MR ($\theta_c = 57^\circ$), this behavior could have implications when water is present in the CO₂ stream, affecting the membrane permeability.

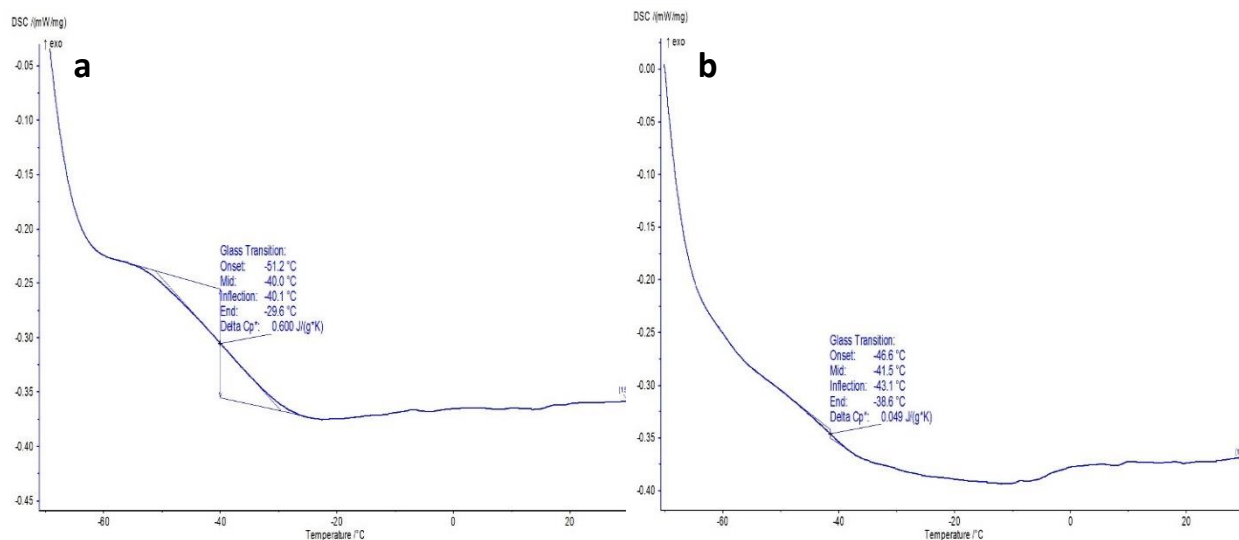


Figure 2.8 DSC analysis of (a) PEGDA/DR1M and (b) PEGDA/MR samples.

1.3.3 Permeability characterization

In this section, the membranes containing both the chromophore dyes were characterized in the permeometer to study their barrier properties to CO₂ in different condition of temperature, relative humidity and light irradiation, in comparison with membrane containing only PEGDA. Firstly, the permeability of the membranes was measured by varying the temperature and the relative humidity without light exposure. This was done to analyze how the gas transport through the polymer membranes containing the chromophore dyes could be modified by external factors such as temperature or the presence of a variable amount of water in the gas stream. Figure 2.9 shows the CO₂ transmission rate of the membranes containing PEGDA/MR and PEGDA/DR1M tested at 10°C, 25°C and 50°C at zero relative humidity (a) and (b) and at constant temperature (T= 25°C) and under different relative humidity (0%, 50% and 100%), (c) and (d), in dark conditions. In the first case, where the relative humidity was kept at zero and the temperature was varied from 10°C to 50°C, for both dyes, as expected permeability remarkably increased as the temperature was raised. The increase in permeability with temperature was due to the increase in CO₂ diffusivity and solubility in the polymer membrane. Transport of gas molecules depends on the available free volume in the polymer matrix, as well as sufficient energy of the molecules to overcome attractive forces

between chains. The thermal fluctuations generated by heat treatment, lead to a change in the polymer structure and an excess space that permits the passage of the gas molecules (230). At low temperatures, gas molecules in an amorphous polymer tend to spend most of their time bouncing inside the free volume pocket and only

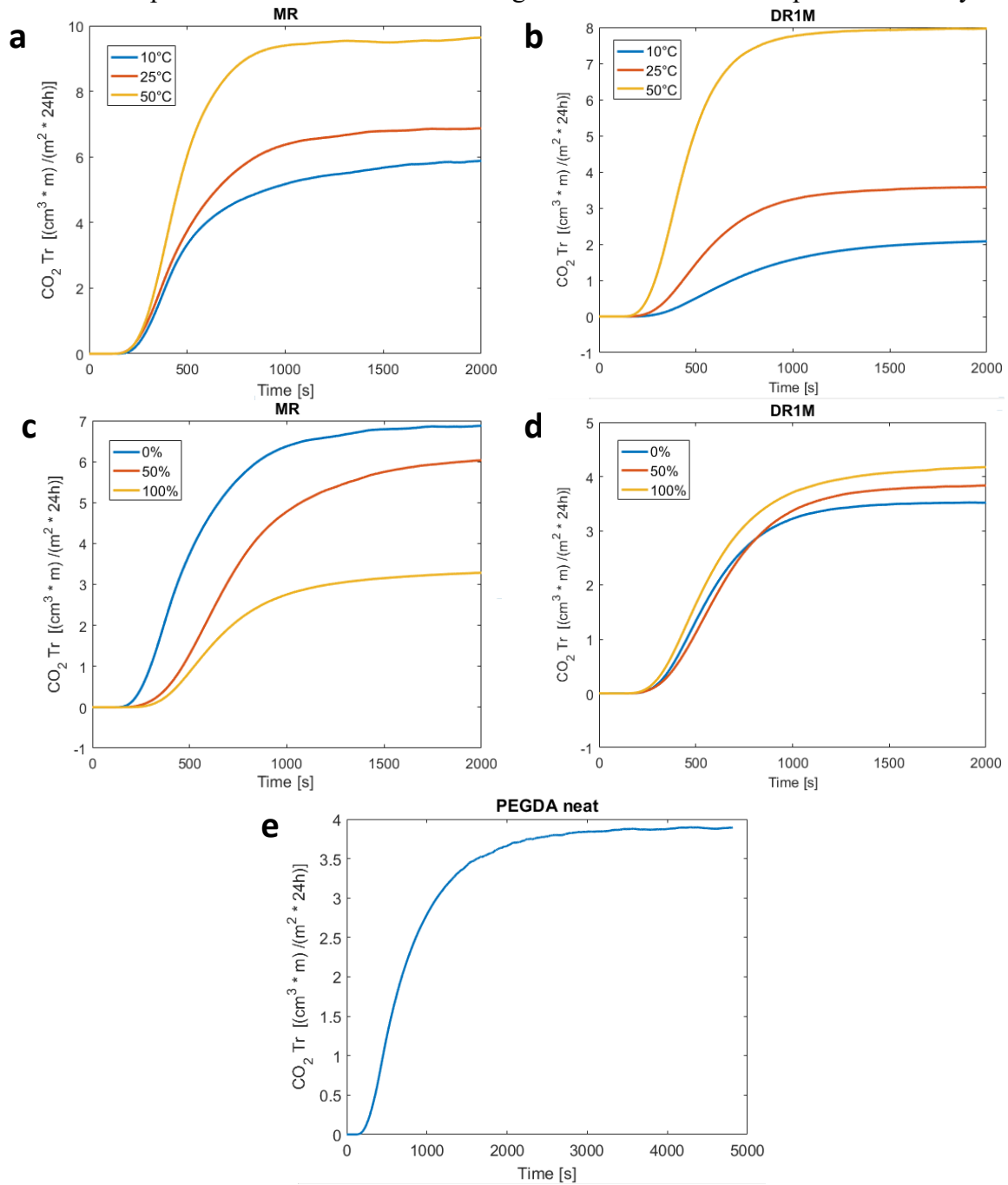


Figure 2.9 Permeability analysis (curves normalized on thickness) in dark condition of PEGDA membrane containing (a) MR 0% relative humidity at 10, 25, 50°C, (b) DR1M 0% relative humidity at 10, 25, 50°C, (c) MR at 25°C and 0%, 50%, 100% relative humidity, (d) DR1M at 25°C and 0%, 50%, 100% relative humidity and (e) neat PEGDA 0% relative humidity at 25 °C

rarely jumps to an adjacent pocket. At higher temperatures, random walk trajectories occur due to increased polymer dynamics and an increase in

permeability can be measured (231). In the second case, the temperature was kept at 25 °C and the relative humidity was varied from 0% to 100%. As it can be seen from the transmission rate outcomes, the presence of water molecules tends to decrease the CO₂ permeability through the membranes. This can be explained by the competition between the water and CO₂ molecules inside the polymer matrix; in fact, water seems to hinder the passage of the gas through the membrane. This behaviour is more evident in the PEGDA/MR membrane than in PEGDA/DR1M membrane, in accordance with the contact angle measurements, where DR1M containing membranes resulted being more hydrophobic than MR containing ones. The values of permeability in dark conditions are summarized in Table 2.1. After the complete evaluation of the transmission properties of PEGDA/MR and PEGDA/DR1M membranes in different conditions of temperature and relative humidity, CO₂ permeability analysis were performed on the azo-benzene membranes by laser irradiation, as described in section 1.2.3. The dynamic measurement in light condition was performed by irradiating the membrane when the transmission rate plateau was reached, that is when a steady state of the gas diffusion flux through the membrane was achieved. Figure 2.10 shows the transmission rate curve of CO₂ through PEGDA/MR (a) and PEGDA/DR1M (b) membranes (160 μm) at 25 °C and 0% relative humidity at saturation value. As it

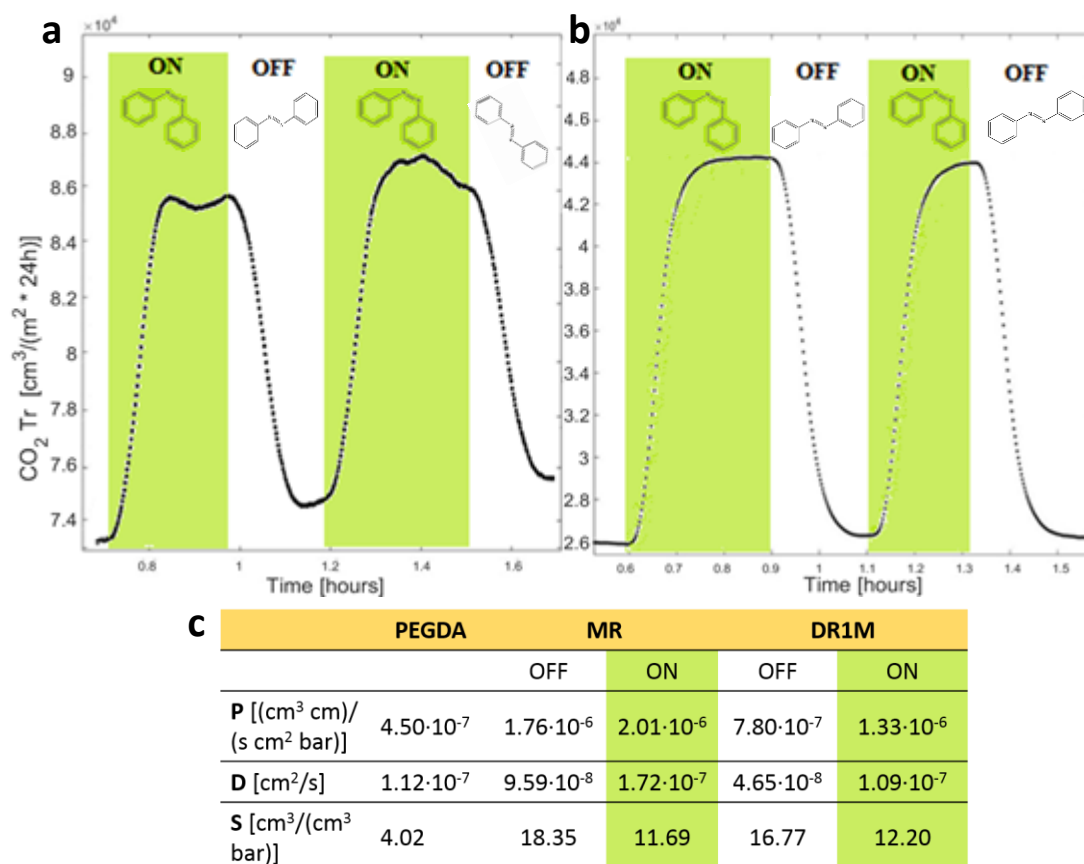


Figure 2.10 Transmission rate curves at plateau during LASER illumination of membranes containing (a) MR and (b) DR1M, (c) calculated permeability, diffusivity and solubility of neat PEGDA, PEGDA/MR and PEGDA/DR1M.

can be seen in the resulting plots, as the light is turned on, the transmission rate, together with the permeability, increases quickly, proportional to the diffusivity of the gas, to a saturation value. As the laser was turned off, the transmission rate decreased smoothly to the initial value, indicating that the chromophores thermally relaxed to the low energy state (trans) as no more light excitation was provided. Moreover, a delay of the response of the permeability change after laser switching on and off was noticeable, imputable to the time required to the gas molecules to permeate through the membrane, proportional to the membrane thickness. The measurement was run several times and the behaviour remained stable during the repetitions. Analysing the results, the membrane containing PEGDA/MR experienced an increase of permeability of around 15% during irradiation, with respect the initial value. Whereas for PEGDA/DR1M, the step of transmission rate after light excitation was wider than the one of PEGDA/MR, corresponding of a much greater increase of permeability (70%). In Figure 2.10c a table reports the calculated CO₂ transport parameters of PEGDA, PEGDA/MR and PEGDA/DR1M membranes. As can be seen, CO₂ permeability and diffusivity of PEGDA/MR have a greater value than the ones related to PEGDA/DR1M membrane, both in ON and OFF states. This tendency was already observed in the experiments carried out in dark conditions and explained with the lower crosslinking density calculated for the membranes containing MR. Moreover, in the ON state, the increase in permeability triggered by the light was less evident in the PEGDA/MR membrane than in the PEGDA/DR1M one. This effect could be due to the more rubbery polymer network structure surrounding the groups undergoing isomerization and to their distribution in the polymer matrix. The isomerization behavior of polymers containing cross-linked azo-moieties network (like PEGDA/DR1M) and that of unlinked azo-dyes added (like PEGDA/MR) was studied for several polymer matrices (232-235). In all cases, the chromophore photo-activity resulted being dependent on the viscous properties and on the free volume distribution of the surrounding network. Many studies also reported that the dispersion of non-covalently bonded chromophores in

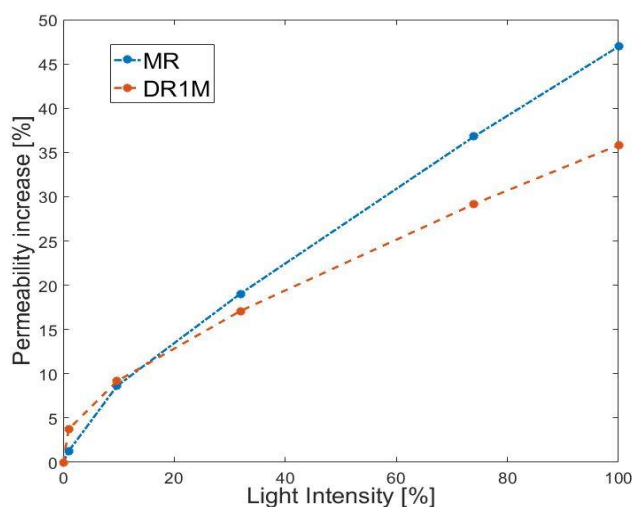


Figure 2.11 Permeability increase vs LASER intensity of membrane containing MR and DR1M.

a matrix can exhibit instabilities because of their mobility and tendency of the dipolar azo units to form aggregates(236) that could lead to a slower isomerization mechanism. Whilst the covalent bonding of side chains, bearing azo-benzene groups, can facilitate the cooperative movement of chain segments (232). Accordingly, the more evident PEGDA/DR1M permeability increase due to light irradiation could be the result of a better dispersion of the DR1M dye molecules together with the formation of a different network that could influence the free volume distribution and the chain mobility. In addition, it was demonstrated that the increase of the laser intensity is proportional to the increase of gas permeability (see Figure 2.11). In fact, an enlarged photon flow can trigger a greater number of azo-benzene chromophore with a consequent increase of the free volume in the polymer matrix. Besides, increasing the laser power has not only implication on the increment in the permeability, but also on the kinetic of the process because, by looking at the trend of the curve, the permeability increase gets slower. This could be explained by the fact that at a certain threshold, corresponding to a very high laser intensity, the permeability increase is expected to saturate to a constant value, since no more chromophore can be further isomerized (237). To completely characterize the membranes, a study was conducted on the influence of the laser on the temperature variation of the membrane surface. Since a lot of power is supplied from the laser, it was decided to investigate how much the temperature of the membranes could be affected by the laser beam. The temperature increase of the membranes containing PEGDA/MR, PEGDA/DR1M was measured with an

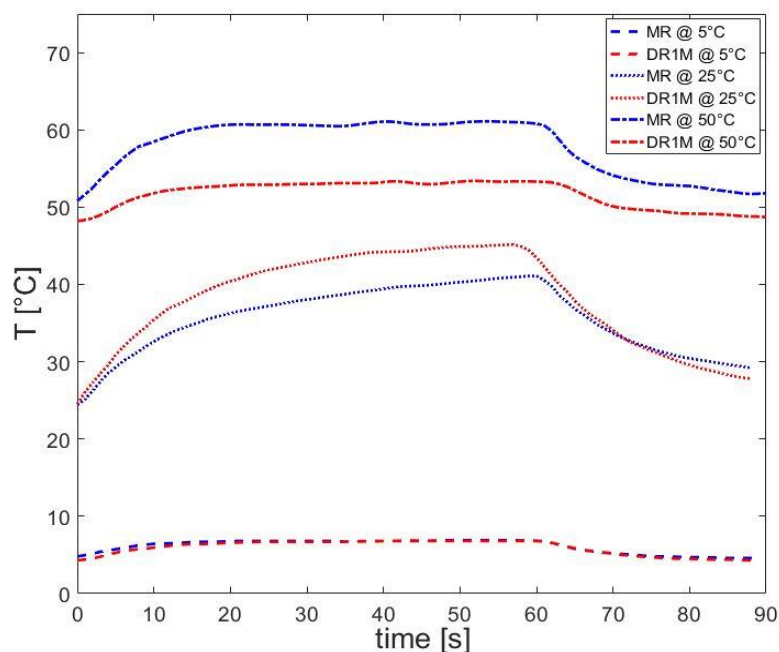


Figure 2.12 Temperature variation during LASER illumination at 5, 25, 50°C initial temperatures of membrane containing MR and DR1M.

infrared thermometer in three ranges of temperatures: 5 °C, 25 °C and 50 °C (see figure 2.12). Since the LASER radiation that hits the membrane is almost completely absorbed by the azo molecules contained inside the polymer matrix.

The absorbed energy can be then converted in movement of the molecules caused by isomerization that thermalize (i.e. dispersed as heat) to the low energy state. The reorganization of the azo molecules inside the polymer matrix combined with the

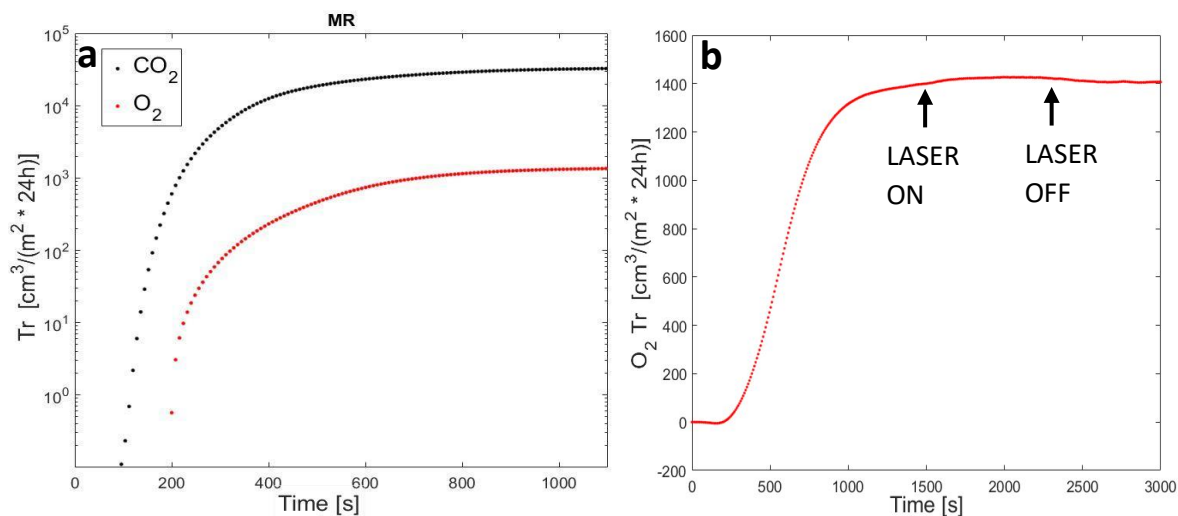


Figure 2.13 (a) Logarithmic plot of transmission rate of carbon dioxide and oxygen for membrane containing PEGDA/MR, in dark condition, (b) linear plot of oxygen transmission rate in the same membrane, during laser irradiation.

thermalization process, produces heat that can be measured during the LASER illumination. The temperature variation during irradiation was measured as described in section 1.2.3. The starting temperatures were chosen close to the ones used for the permeability measurements at different temperatures. Figure 2.12 shows the temperature variation during laser illumination for MR and DR1M at three different temperatures. The greatest temperature increase was registered at room temperature with a ΔT of about 15°C for MR and DR1M. At 5°C and 50°C the temperature increase was lower than at room temperature and the ΔT ranged from 2°C to 10°C at starting temperature of 5°C and 50°C respectively. The lower temperature increase at 5°C can be explained because the polymer chains are less mobile and there is less transfer of energy between them and dye molecules.

As the azo membranes were completely characterized in different conditions, to deeply understand the CO_2 permeability behavior, it was decided to test them towards oxygen, to further enhance the study of the permeability control of this photo-switching molecules to other gases. In fact, azo molecules could even be used for gas separation, exploiting the different permeability of gases with different properties. For instance, it was recently demonstrated that by coupling azobenzene molecules with MOFs, selective permeability between N_2 and CO_2 was achievable(130, 131). For that reason the azo containing membranes were tested with oxygen both in dark and light conditions. Figure 2.13a shows the O_2 transmission rate curves of the PEGDA/MR membrane at 25°C and 0% relative humidity in dark condition, compared to the one related to CO_2 . Results show that the O_2 permeability was remarkably lower than CO_2 permeability (almost of a factor 30), in line with literature data(222). Furthermore, the measure was repeated during laser irradiation and the photo-switching of the chromophore molecules did

not remarkably affect the oxygen permeability (figure 2.13b). This behavior was interpreted by considering the larger kinetic diameters of oxygen with respect carbon dioxide (O_2 3.46 Å vs CO_2 3.3 Å)(238), bringing to have a path with more obstacles for the O_2 molecule that for CO_2 one. This can explain the non-switching ability of the azo molecules in case of oxygen gas is used, since the increase of free volume due to the new polymer matrix arrangement could not be enough for the oxygen atoms to pass more freely. Additionally, PEGDA is a polar matrix thanks to the high number of polar ether oxygen atoms in its polymer backbone, so the polar CO_2 sees more affinity with it than the non-polar O_2 (239, 240), explaining the higher CO_2 permeability in dark conditions.

Table 2.1 Properties of the membranes containing MR and DR1M azo dye compared to the properties of neat PEGDA (Mw575).

	% Conversion	T_g (°C)	G' @10°C (°C)	Cross-linking point density (mmol/cm ³)	Permeability [(cm ³ cm)/(s cm ² bar)]
Neat PEGDA	97	-18	$2.24 \cdot 10^7$	9.8	$4.50 \cdot 10^{-7}$
PEGDA/MR	91	-28	$4.08 \cdot 10^6$	1.7	$1.76 \cdot 10^{-6}$
PEGDA/DR1M	92	-26	$8.4 \cdot 10^6$	3.7	$7.80 \cdot 10^{-7}$

1.3.4 3D printed device for pH control

Once it was able to control the permeability properties of the azo-containing membranes, it was decided to exploit the double functionality of the photo-switching chromophores acting also as a dye, to produce a photo-controllable 3D printed smart device. An object with a specific structure geometry was designed with a CAD software and produced by 3D printing using DLP technology (see figure 2.14). The design of the object was conceived as a joint where a flux of CO_2 could be controlled by an external light source. In detail, a photo-controllable membrane was printed in the bulk of the structure and controlled through a laser transparent window created on the opposite side of the structure. The whole object was built using PEGDA 575 as a constitutive monomer, while for the transparent window and the photo-functional membrane was added brilliant green (BG) dye (transparent at $\lambda = 532$ nm) and MR respectively. The 3D printing process was performed in such a way that it was possible to build the entire device in one single

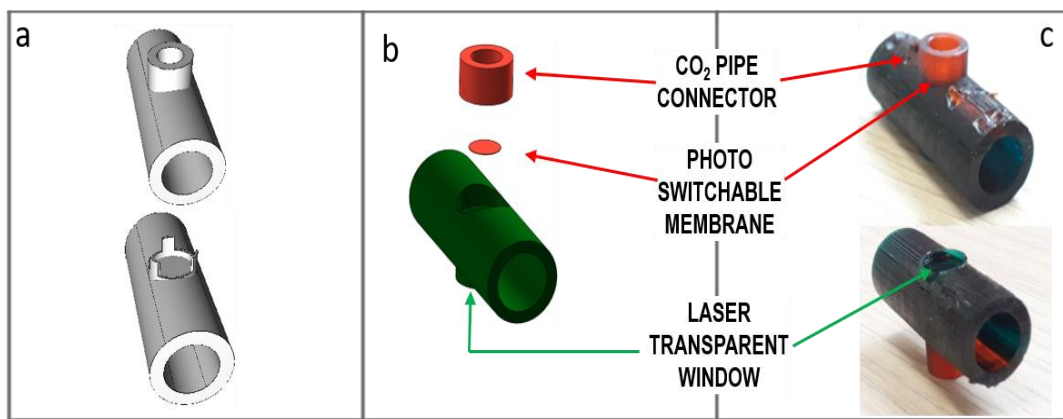


Figure 2.14 (a) CAD file of the prototype top and bottom view, (b) exploded vision of the prototype, (c) 3D printed prototype top and bottom view.

shot. In fact, two different formulations, one containing the photo-chromic dye (MR) and the one with the laser transparent dye (BG), were employed in the printing process. Firstly, the part of the object containing the azo membrane was printed, then, the process was paused and the resin changed to complete the whole structure. The working principle of the device, visually explained in figure 2.15a, consists in the control of the CO₂ flow by the azo membrane, which permeability was made vary by a laser beam ($\lambda = 532 \text{ nm}$) at different power intensities. The device was connected to an argon inlet acting as gas carrier and to the gas outlet bringing the permeated CO₂ to a water solution. The intrinsic permeability change of the azo membrane was used to control the transmission rate of CO₂ in the argon stream and finally in the solution. The mixture of gases was let bubble in the water

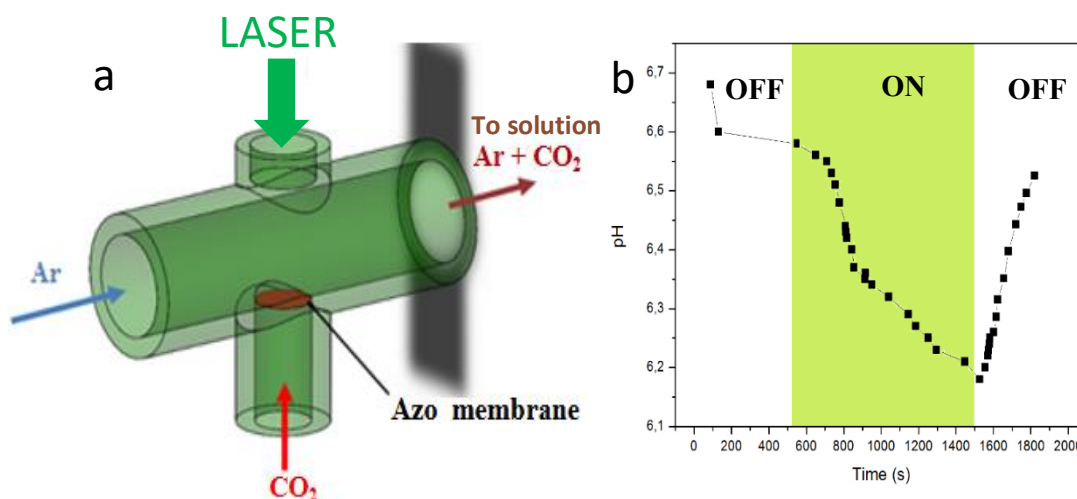


Figure 2.15 (a) prototype CAD and working principle and (b) solution pH variation in light and dark condition.

solution and the pH was monitored during the OFF/ON/OFF laser states (see experimental setup in Figure B1 in Appendix B). Figure 2.15b shows the pH variation in the solution due to carbonic acid formation as CO₂ solubilizes in the water. When the laser was ON, the CO₂ concentration started to increase, changing the pH from a value of 6.6 down to a value of 6.2, due to acidification of the

solution. As the laser was turned off, the CO₂ in the solution started to decrease and the pH returned back to its equilibrium value. This light-controlled valve is a proof of concept of the application of the azobenzene dyes in 3D printing giving smart functionalities. In particular, the azobenzene molecules can be used in the field of CO₂ separation by exploiting the infinite possibility in terms of shape and design that 3D printing can give.

1.4 Conclusion

In conclusion, formulations containing PEGDA and azo-chromophores (MR, DR1M) showed excellent polymerization reactivity and chemical stability after photo-polymerization, making them highly suitable for 3D printing. The 3D printed membranes were fully characterized to analyze how the materials properties behaved to the addition of the azo-dyes. As expected, both dyes brought to a decreasing of the T_g and of the crosslinking density making it more rubbery and suitable for gas interaction. Subsequently, the membranes, in which MR and DR1M were used both as dye and functional agent, were tested to permeability experiments and showed an increase of 70% of CO₂ permeability under laser irradiation due to the photo-isomerization of the azo molecules that brings a consequent free volume formation in the polymer matrix. Furthermore, laser intensity was found to directly influence the permeability variation, becoming an important parameter to take into account. 3D printing and permeability control were finally merged to build a 3D printed connector prototype able to control the CO₂ flow by a laser source. The variation in the concentration of CO₂ was monitored by measuring the pH variation of a water solution where the gas was let bubble. The results showed a decrease of the pH during the laser irradiation, caused by the formation of carbonic acid becoming more concentrated and an increase of the pH in dark condition. This gave the proof of concept of the possibility to apply specifically designed smart materials to produce customized 3D working devices. Furthermore, an interesting aspect was pointed out during the permeability experiments where remarkably different behaviors was noticed using different gases. In fact, oxygen displayed lower permeability values than CO₂ in dark conditions and no remarkably changes during laser irradiation. This peculiarity could be exploited in future studies on azo embedded polymeric membranes for CO₂ separation and release. The application of such 3D printable materials can be envisaged for the development of devices for detection and for small scale experiments (i.e. microfluidics for reaction testing, application for biology and microbial fuel cells) in which the three dimensional design can improve performances and possibilities.

Chapter 3

Study on the printability through DLP technique of ionic liquids for CO₂ capture

1.1 Introduction

As explained in Chapter 1, the problems related to uncontrolled CO₂ emissions and global warming, brought to find and study effective methods for carbon capture (CC). Ionic liquids (ILs) and poly ionic liquids (PILs) have been employed for this purpose in many forms and seem to have the right capability to be implemented in CC technology for both research and industry. In 2007 Bara et al. (145) presented a study on the use of polymerized room temperature ionic liquids (poly(RTILs)) membranes for CO₂ capture, obtaining outstanding results, way better than their liquid analogues. These astonishing results on the ability of the polymerized ionic liquids to capture CO₂ makes this kind of materials extremely attractive for the development of devices for CCS (241). Moreover, it is possible to produce smart filters by shaping the materials with complex geometries. In this context, 3D printing could be a great solution (242). In fact, 3D printing (see Chapter 1 section 1.4) enables the direct creation of three-dimensional object starting from a digital model (243).

This chapter, that in part describes the work early published in Gillono et al. (244), presents the study of DLP 3D printable polymeric formulation containing different ILs. The formulations were prepared in such a way that they can undergo photo-polymerization by visible light, to be suitable for DLP technology, and they can be cross-linked, with ILs species inside, avoiding separation and leakage. Finally, the DLP technique allows to create structures with high shape freedom and superior precision, which is necessary for more complex devices (245). In this work the 3D printed structures incorporate different ILs, that in some cases are just trapped in the polymer matrix, whereas, in other cases, are co-polymerized in the polymer network. The formulations were firstly characterized for what concern their ability to photo-polymerize. To do so, a polymerization study, similar to the one shown in chapter 2, was carried out by means of photo-rheology, to analyze their behavior when irradiated and see their reaction kinetic. In this case, the formulations contain a greater amount of fillers, with respect the formulation

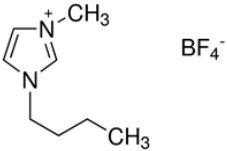
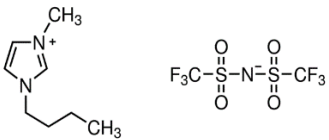
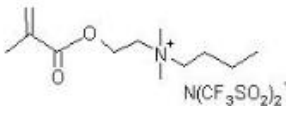
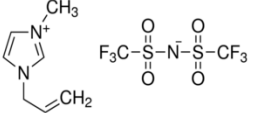
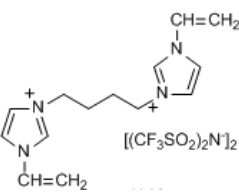
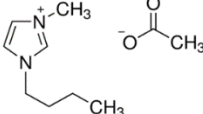
studied in chapter 2, which can largely affect the 3D printing results. Secondly, the formulations were loaded in the DLP apparatus and 3D printed to create filter-like hollow cubic structures. Since some of the studied ILs present reactive groups, FTIR-ATR analyses were carried out on the 3D printed samples to investigate the typology of bond present in the polymer between the ILs and the matrix. Afterwards, thermomechanical measurements were performed to investigate the materials properties of the 3D printed samples containing ILs. Finally, CO₂ permeability analysis were performed on polymerized membranes to study their gas transport properties for a possible application in SLM and CO₂, as well as CO₂ uptake measurements on the 3D printed cubic structure containing different IL species and concentrations.

1.2 Experimental and methods

1.2.1 Materials

Poly(ethyleneglycol)diacrylate (Mn. 575) (PEGDA) was used as constitutive monomer, for the same reasons described in chapter 2, (Bis(2,4,6-trimethylbenzoyl)-phenylphosphineoxide (BAPO) was chosen as photo-initiator because it suits perfectly for the lamp used in DLP 3D printing, reactive orange 16 was employed as a dye to have a good printing resolution. Finally, six different ionic liquids were chosen to be added to the formulations: 1-Butyl-3-Methylimidazolium tetrafluoroborate, 1-Butyl-3-Methylimidazolium bis(trifluoromethylsulfonyl)imide, 1-Allyl-3-Methylimidazolium bis(trifluoromethylsulfonyl)imide and 1-Butyl-3-Methylimidazolium acetate were purchased from Sigma Aldrich. N,N,N,N-ButyldimethylMethacryloyloxyethylammonium bis(trifluoromethylsulfonyl)imide and 1,4-Butandiy1-3,3'-bis-1-vinylimidazoliumbis(trifluoromethylsulfonyl)imide. The name, abbreviation and molecular schematics are shown in Table 3.1.

Table 3.1 molecular schematics and abbreviations of the ionic liquids used in the formulations.

IL	Abbreviation
<p>1-Butyl-3-Methylimidazolium tetrafluoroborate</p>  <p>Bmim[BF4]</p>	P_Bmim[BF4]
<p>1-Butyl-3-Methylimidazolium bis (trifluoromethylsulfonyl)imide</p>  <p>Bmim[Tf2N]</p>	P_Bmim[Tf2N]
<p>N,N,N,N-ButyldimethylMethacryloyloxyethyl ammonium bis(trifluoromethylsulfonyl)imide</p>  <p>C4N_{MA,11}[Tf2N]</p>	P_C4N _{MA,11} [Tf2N]
<p>1-Allyl-3-Methylimidazolium bis (trifluoromethylsulfonyl)imide</p>  <p>Amim[Tf2N]</p>	P_Amim[Tf2N]
<p>1,4-Butandiy1-3,3'-bis-1-vinylimidazoliumbis (trifluoromethylsulfonyl)imide</p>  <p>Bvim [Tf2N]</p>	P_Bvim[Tf2N]
<p>1-Butyl-3-Methylimidazolium acetate</p>  <p>Bmim [ac]</p>	P_Bmim[ac]

1.2.2 Formulations preparation and characterization

The formulations used to produce the 3D printed structures were prepared by mixing PEGDA as constitutive monomer with a dye (Reactive Orange), the photo-initiator (BAPO) and the different ionic liquids in the following concentrations (with respect PEGDA):

- Reactive Orange: 0.2 %wt
- BAPO: 2 %wt
- Ionic liquid: 0.44 mmol/g

Initially, the formulations were analysed to investigate their polymerization reactivity during light irradiation. For that reason, photo-rheology analysis were carried out on the formulations containing the different ionic liquids. The measurements were performed using an Anton Paar rheometer (Physica MCR 302) in parallel plate mode with a Hamamatsu LC8 lamp with visible bulb and a cut-off filter below 400 nm equipped with 8 mm light guide. Once the formulations were characterized from the polymerization point of view, 3D printing tests were done to create simple membranes first and more complex cubic structures after. For both the structures printed and for all the ILs employed, printing parameters will be reported. The 3D printing process was carried out with a digital light processing (DLP) Asiga Freeform and Robot Factory3D printers (see Chapter 1 section 1.4.3 for more details on DLP technology and Chapter 2 section 1.2.2 for the 3D printer characteristics). Secondly, Fourier transform infrared attenuated total reflection (FTIR-ATR) analysis were performed to investigate the properties of the ionic liquids inside the polymerized formulations. In fact, ionic liquids with different chemical groups were adopted in this work, able to react during photo-polymerization or not. With FTIR-ATR technique, it was possible to see the peaks related to the different ionic liquids and specific reactive groups in the formulation before and after photo-polymerization as well as after solvent washing. Solvent washing was done by immersing the samples for 24 h in acetone to see if the ILs present in the polymer network remain linked or diffuse in the solvent. FTIR-ATR spectra were collected using a Tensor 27 FTIR Spectrometer (Bruker) equipped with ATR tool, 32 scans were collected with a resolution of 4 cm⁻¹ from 4000 to 400 cm⁻¹. In relation to the FTIR-ATR measurements, weight analyses were performed on the 3D printed samples. Afterwards, Dynamic mechanical thermal analyses (DMTA) measurements were carried out on the 3D printed samples to see the variation on the mechanical properties by varying temperature, e.g. variation of the glass transition temperature and crosslinking density, influenced by the different ionic liquids present in the polymer matrix. The crosslinking density, corresponding to the number of moles of crosslinked chains per unit volume, also known as the strand density, was calculated as shown in Eq.1.

$$\nu = \frac{E'}{RT} \quad (1)$$

Where E' is the storage modulus, R is the ideal gas constant and T the absolute temperature. E' is chosen at a temperature T where the rubbery plateau is reached (246). The analyses were performed with a Triton Technology TTDMA. All of the experiments were conducted with a temperature ramp of $3\text{ }^{\circ}\text{C}/\text{min}$, applying a force with a frequency of 1 Hz and a displacement of $20\text{ }\mu\text{m}$ with temperature range between -80°C e 30°C . To further characterize the polymerized samples, TGA and DSC analysis were carried out. TGA measurements were performed with a Thermo Netzsch *TG 209 F1 Libra instrument* with a temperature ramp of $10\text{ }^{\circ}\text{C}/\text{min}$ in air. DSC analysis were conducted with a DSC 401 Phoenix with a temperature ramp of $10^{\circ}\text{C}/\text{min}$ and temperature range from $-70\text{ }^{\circ}\text{C}$ to 100°C . Further analysis on the contact angle with water were conducted on the surface of the membranes containing the ILs. The measurements were performed with water ($\gamma = 72.8\text{ mN}/\text{m}$) using the First Ten Angstroms (Portsmouth, VA) 1000 C instrument, equipped with a video camera and image analyzer, at room temperature, by the sessile drop technique. The 3D printed membranes were then tested in the permeometer apparatus to determine their permeability to CO_2 (see description of the apparatus and the experimental method in Chapter 2 section 1.2.3). Finally, CO_2 absorption analysis were performed on the 3D printed hollow cubic structures to investigate the capture capacity of the polymer samples containing different ionic liquids. The measurements were conducted with a gravimetric analysis system, by weighting the samples before and after the CO_2 exposure. The apparatus was composed by a pressurizing test chamber connected with a CO_2 cylinder and a vacuum pump, used to clean the chamber and regenerate the samples (see Figure 3.1). Before each

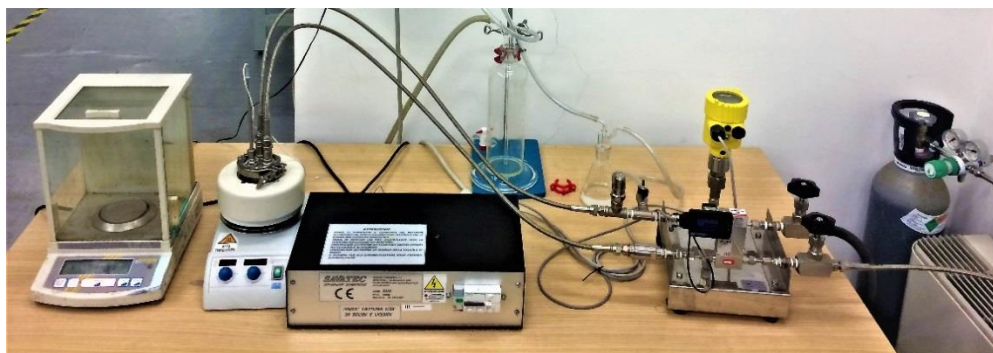


Figure 3.1 experimental apparatus for CO_2 capture.

experiment, the chamber was put under vacuum and filled with CO_2 at 1 bar for 3 times, to properly clean it from undesired contaminant gases and water. Afterwards, the samples were kept exposed to 1 bar or 3 bar of CO_2 for 6 h . To fully characterize the samples on the CO_2 uptake, FTIR_ATR analyses were carried out on the samples before and after CO_2 capture. The samples were obtained by depositing the formulation on a silicon support to create a thin layer, then, they were polymerized in inert atmosphere by UV light. The samples were degassed in vacuum for 2 hours to clean them from any trace of gas adsorbed on the surface before each test. The CO_2 uptake phase was carried out by inserting the samples in the CO_2 capture unit for 4 hours at a pressure of 4 bar . Furthermore, cleaning cycles were performed on

the tested samples after CO₂ exposure both with vacuum for 24 h and heating at 80°C for 4 h. The measurements were helpful to understand the amount of CO₂ captured and released by the samples after the cleaning cycle.

1.3 Results and discussion

The prepared formulations were firstly analysed for what concerns their polymerization reactivity. As already described in Chapter 2, the formulations were tested by means of photo-rheology to describe their photo-curing behaviour containing different ionic liquids, with respect neat PEGDA. Figure 3.2 shows the curves of photo-rheology measurements, where the storage modulus (G') evolution

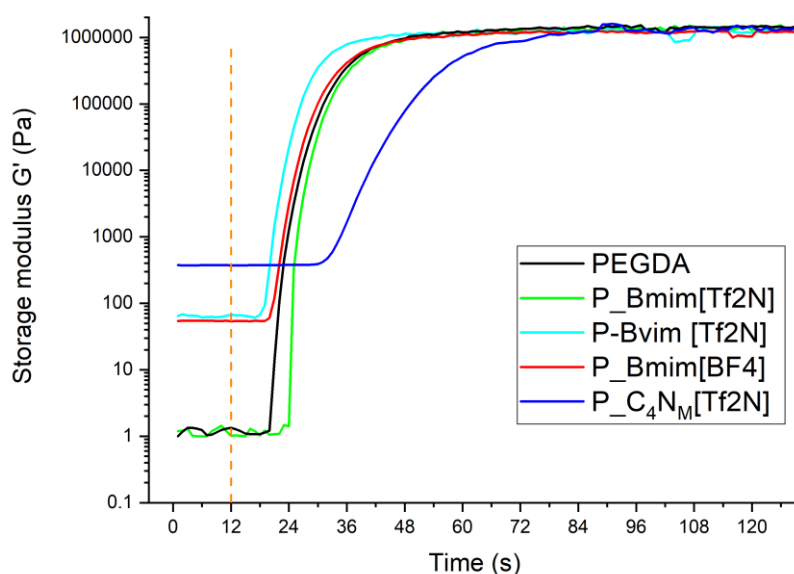


Figure 3.2 Smoothed curves representing G' (Pa) modulus vs time (s) during irradiation.

with time is displayed. As the formulation starts to polymerize, the crosslinking density is expected to increase together with G' . As it can be seen from the results, the presence of the ILs in the formulations tends to influence the value of G' in the initial part when the lamp is off. This can be interaction due to the between PEGDA's polymeric chains and the ILs. After the lamp is turned on at second 12, the reaction kinetics do not vary significantly from the one of neat PEGDA, with the exception of P_C₄N_{MA,11}[Tf₂N]. In fact, P_C₄N_{MA,11}[Tf₂N] displays a slower kinetic of polymerization with a response time that is almost double with respect the other formulations. This can be explained by the fact that, since P_C₄N_{MA,11}[Tf₂N] is ammonium based, amines tend to quench radical polymerization reactions (247). From this result, it can be observed that possible issues can emerge during the 3D printing process for formulations containing this IL. Furthermore, the IL P_Amim[Tf₂N] was not considered in the analysis because of its very low reactivity and the impossibility to be 3D printable. Consequently, the formulations were used to perform 3D printing tests to create three-dimensional

filter-like structures. Initially, it was decided to print simple membranes, to find the correct printing parameters for each formulation. The membranes were printed with the Asiga 3D printer using a layer thickness of 10 μm , the layers irradiation times for each formulation are reported in Table 3.2. The irradiation time values of most of the formulations are around 0.5 seconds and are the same of the one of neat PEGDA, the only exception is for P_ Amim[Tf2N] and P_ Bmim[ac], which require a higher time of irradiation during the printing process. For P_ Bmim[ac], in particular, irradiation times were too high also to create a free standing and easy to handle membrane. For that reason, it was not taken more into consideration. Once the printing times of all the formulation containing different ionic liquids were evaluated, it was possible to perform the first tests for the realization of the three-dimensional cubic structures as shown in Figure 3.3.

Table 3.2. Irradiation times (s) for each layer for membranes printing (10 μm) and cubic structures printing (50 μm).

Sample	Time (s) Membranes	Time (s) Cubic structures
PEGDA	0.5	2
P_ Bmim[BF4]	0.5	1.7
P_ Bmim[Tf2N]	0.5	2
P_ C ₄ NMA ₁₁ [Tf2N]	0.5	1.8
P_ Amim[Tf2N]	0.8	Not obtained
P_ Bvim[Tf2N]	0.5	1.7
P_ Bmim[ac]	2.1	Not obtained

The printing of this complex structures allows to understand the capability of these

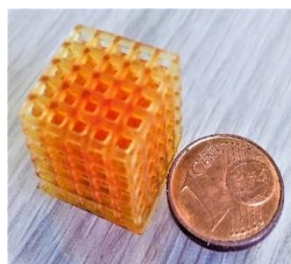


Figure 3.3 picture of the 3D printed cubic structure.

formulations containing ionic liquids to be 3D printed and is aimed to create a filter-like structure for an enhanced CO₂ absorption. For these larger structures it was decided to use the RobotFactory 3D printer because of its higher printing speed. Table 3.2 shows the exposure times used during the printing of the cubic structures

for a layer thickness of 50 μm . The irradiation times of all formulations are longer for the printing of the cubic structure than for the membranes because of the higher layer thickness (50 μm) used in the first case. The results show that not all the formulations (P_ Amim[Tf2N] and P_ Bmim[ac]) are suitable for the 3D printing of complex structures, even if they gave good results for simpler structures like membranes. In fact, more complex structures require a higher definition of the printing to build smaller features and therefore a higher control over the printability. For these reasons, the two ILs were excluded from the next steps of the work. The reactivity of the ionic liquids inside the PEGDA polymer matrix and their polymerization mechanisms were analyzed by carrying out FTIR-ATR measurements on the photo-polymerized formulations. First, the FTIR spectra of the neat ionic liquids and the one of neat PEGDA were collected to associate each peak to the related chemical group and recognize their ‘fingerprints’. Afterwards, the polymerized PEGDA/IL samples were analyzed as well before and after solvent washing.

Table 3.3 Ionic liquid content in the samples in relation to the weight variation after solvent treatment.

Sample	Ionic liquid concentration (%wt)	Weight variation (%wt)
P_Bmim[BF4]	9	8.5
P_Bmim[Tf2N]	15.1	13.9
P_C4N _{MA,11} [Tf2N]	17.5	0
P_Amim[Tf2N]	14.7	14.2
P_Bvim[Tf2N]	14.7	0

This procedure was done to understand the behavior of the different ILs inside the polymer matrix in terms of chemical bonding. In fact, as already mentioned, some ILs possess a reactive group able to copolymerize with the PEGDA polymer network creating covalent bonds, while others are simply dispersed in the matrix and free to move. Using this method, it was possible to confirm whether or not the ionic liquids were still present in the polymer matrix after the solvent washing. Figure C1 (see Appendix C) shows the spectra of the neat ionic liquids and neat PEGDA as reference, while, in Figure D1 (see Appendix D) the spectra of polymerized samples before and after washing in acetone are displayed. From the results, it can be confirmed that the spectra of the samples containing C₄N_{MA,11}[Tf2N] and Bvim [Tf2N] remain unvaried after solvent washing, proving that the ionic liquids formed a bond with the polymer chains during polymerization and remained linked. Instead, the other spectra (Bmim[BF4], Bmim[Tf2N] and Amim[Tf2N]) show the disappearing of the peaks related to each ionic liquid after the solvent washing, demonstrating that this kind of ionic liquids, bearing no

reactive groups, did not link to the polymer chains. These results were further confirmed by a weight analysis of the samples before and after the solvent washing. Table 3.3 reports the values of the initial ILs weight concentration and the weight variation after washing.

Table 3.4 Glass transition temperature (T_g) values calculated through DSC and DMTA and crosslinking density of the polymerized formulations.

Sample	T_g (DSC) °C	T_g (DMTA) °C	Crosslinking density ν (mmol/cm ³)
PEGDA	-19.9	-17	10,7
P_Bmim[BF4]	-22.6	-21.3	1,3
P_Bmim[Tf2N]	-22.5	-21.6	1,36
P_C4NMA,11[Tf2N]	-15.1	-12.8	3,0
P_Amim[Tf2N]	-44.8	-	-
P_Bvim[Tf2N]	-11.2	-10	10,9

As already discussed after the FTIR analysis, ILs presenting a reactive group created a bond with the polymer network, while the ILs with no reactive groups were removed by the solvent. It is shown in the table that the IL washing caused a weight loss almost equal to the initial IL concentration in the sample. After having assessed the reactivity of the ionic liquids within the polymer matrix, a thermo-mechanical study was performed to analyze how the presence of the ionic liquids in the polymerized sample influences the overall crosslinked structure. In fact, the chain movements of the polymer and the ability of a gas to move through the polymer matrix, thus its permeability, are closely correlated to the structure of the crosslinked network and its crosslinking density. Thus, DSC and DMTA analysis were conducted on all the polymerized samples and on PEGDA. From the analysis, the glass transition temperature and crosslinking density were calculated for each measurement (the values are reported in Table 3.4). As it can be noticed, the samples containing the copolymerized ionic liquids possess a higher T_g than PEGDA, indicating that the covalent incorporation of the ionic liquids allows a stronger interaction with the matrix, resulting in a more rigid material. On the other hand, the remaining ionic liquids, only dispersed in the polymer matrix, act as plasticizer, reducing the T_g . In the case of the P_Amim[Tf2N] sample, a very low value of T_g was calculated, probably given by the not completely crosslinked polymer network due to polymerization inhibition. From the DMTA analysis it was possible to estimate the storage modulus of each sample that is an important parameter for the understanding of their mechanical properties and its value in the rubbery plateau is directly proportional to the crosslinking density. Figure 3.4

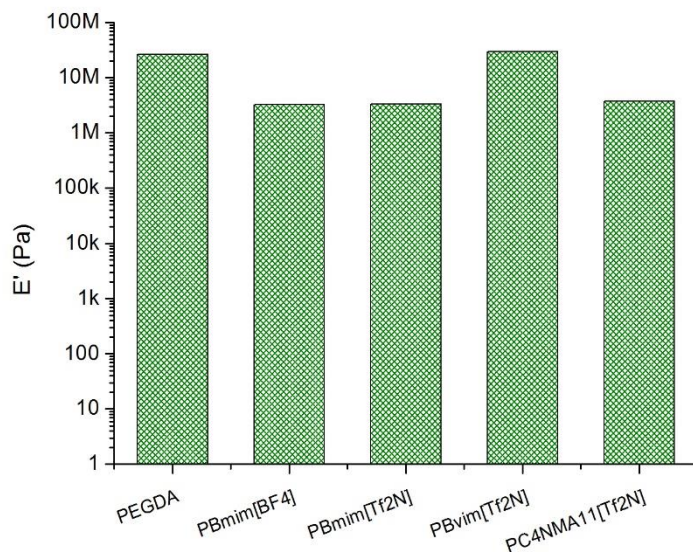


Figure 3.4 storage modulus at 20°C calculated from DMTA analysis.

displays the values of the storage modulus of the samples. As it can be seen, the samples containing the ionic liquids dispersed in the matrix have mechanical properties lower than the one of neat PEGDA, this because they act as a plasticizer in the matrix, that is also visible in the lowering of the crosslinking density (see Table 3.4). Whereas, for the ionic liquid having the bi-functional vinyl group (Bvim [Tf2N]), mechanical properties are enhanced by its higher crosslinking density, proved by the increased storage modulus. For what regards the sample containing P_ C₄N_{MA,11}[Tf2N], the mechanical properties did not increase too much because of the methacrylate monofunctional group that does not improve the polymer network.

After these analyses, carried out to study the polymerization kinetic, the printability and the chemical-mechanical properties of the formulations and solid samples, further experiments were performed to investigate the interaction with CO₂. In first place, the FTIR technique was employed to observe the CO₂ absorption mechanism of the polymerized samples, through the formation of new peaks in the IR spectrum after CO₂ exposure. The measure was carried out in three main phases, after the cleaning cycle in vacuum, after CO₂ uptake and after the final cleaning treatment. The final treatment was done to release the CO₂ captured during the uptake and was performed by both heating the samples and applying vacuum. Figure 3.5a shows the FTIR-ATR spectrum in the range between 2400 cm⁻¹ and 2300 cm⁻¹ of the neat cross-linked PEGDA sample after the cleaning cycle and after CO₂ uptake. The curves show the appearance of two new peaks centered at 2360 cm⁻¹ and 2330 cm⁻¹, ascribable to the vibrating modes of the CO₂ molecule. This result implies that after the exposure to the gas, CO₂ is physically absorbed in the PEGDA sample. The same measure was done on the other samples and a cleaning cycle was performed after CO₂ uptake. Figure 3.5b shows the FTIR-ATR spectrum in the same range of the P_ Bmim[BF₄] sample after CO₂ uptake, heating treatment

at 80 °C for 4 hours and vacuum for 24 hours. The same peaks related to CO₂ are clearly visible after the absorption, furthermore, a smooth decrease is noticeable after the release process, both with thermal and vacuum treatment, even if the two

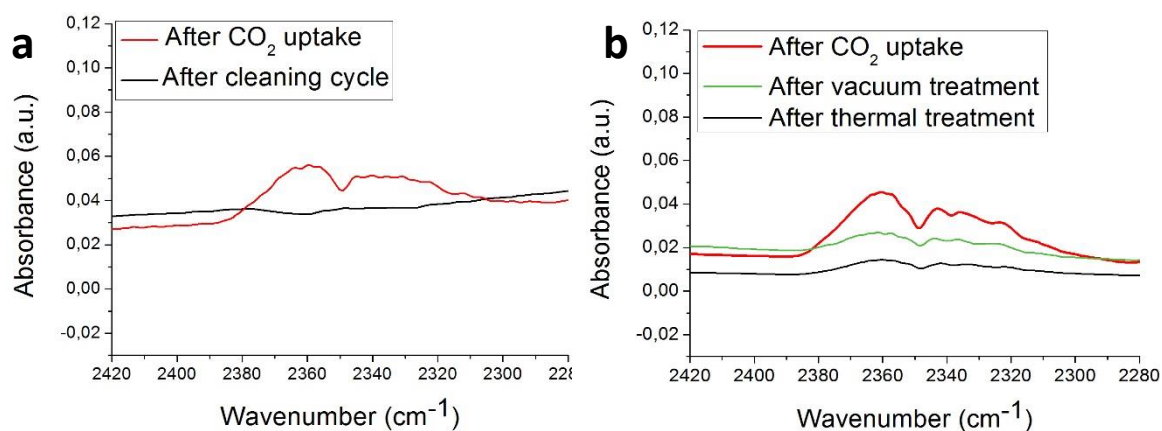


Figure 3.5 FTIR-ATR spectra between 2450 cm⁻¹ and 2200cm⁻¹ of (a) neat PEGDA before (black) and after (red) CO₂ absorption and of (b) P_Bmim[BF₄] after CO₂ absorption (red), vacuum cleaning (green) and thermal treatment (blue).

bands are still slightly visible. A more severe treatment could be necessary to completely remove the adsorbed gas. The next step to test the prepared samples containing ILs with different arrangements inside the polymer matrix was to carry out CO₂ barrier measurements on 3D printed membranes. This kind of analysis were fundamental for the evaluation of the intrinsic gas transport properties of the membranes such as permeability, diffusivity and solubility, important to understand how well these materials are able to interact with CO₂. Furthermore, it was a first step towards the possible application of these materials as supported liquid membranes (SLM) for CO₂ separation. The membranes were tested in the permeability apparatus with thickness ranging from 180 μm and 500 μm and ionic liquid concentration of 0.44 mmol/g for all the samples. Table 3.5 reports the values of diffusivity, permeability and solubility of the tested samples. Results show that

Table 3.5 Calculated diffusivity (D), solubility (S) and permeability (P) values for 3D printed membranes containing different ionic liquids.

Sample	D [$\frac{cm^2}{s}$]	S [bar^{-1}]	P [$\frac{cm^2}{s \times bar}$]
PEGDA	6,73	4.71	3,17
P_Bmim[BF ₄]	11,33	2.99	3,39
P_Bmim[Tf ₂ N]	8,65	5.26	4,55
P_C ₄ NMA ₁₁ [Tf ₂ N]	4,46	4.22	1,88
P_Amim[Tf ₂ N]	9,53	14.47	13,79
P_Bvim[Tf ₂ N]	8,45	3.20	2,70

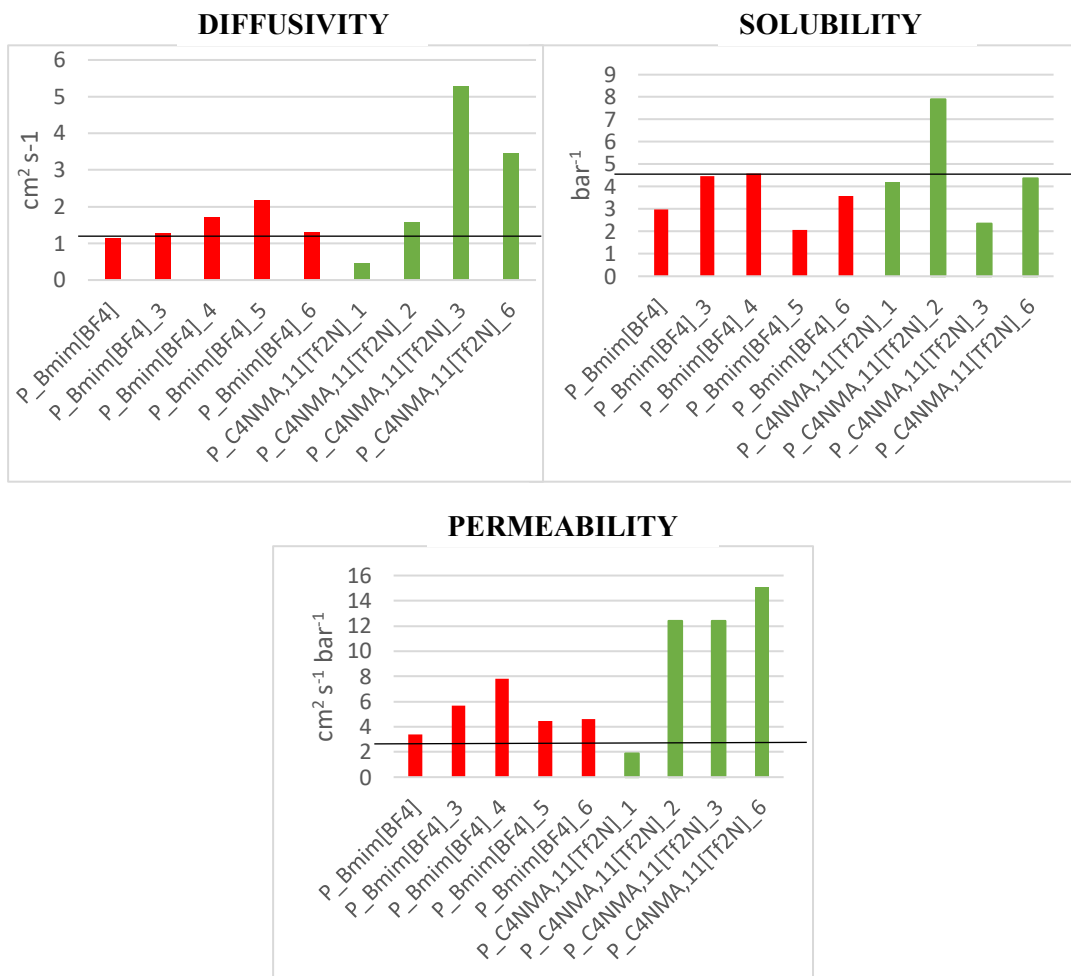


Figure 3.6 Diffusivity, solubility and permeability values of membranes containing increasing concentrations Bmim[BF4](red) e C₄N_{MA,11}[Tf2N] (green). The black line indicates the value calculated for neat PEGDA.

the addition of the ionic liquids to the formulation increases the gas diffusivity for all the samples, excluded C₄N_{MA,11}[Tf2N]. The samples with higher diffusivity is Bmim[BF4], which presents a value that is almost double with respect the neat PEGDA. For what regards solubility, the sample with a significant variation from PEGDA is Amim[Tf2N], which unfortunately, was not possible to 3D print. The intrinsic property that allows to evaluate the effectiveness of a SLM system is the permeability and, among the analyzed samples, the most promising are Bmim[BF4] and Bmim[Tf2N]. Afterwards, further analysis on the CO₂ transport properties were performed on samples P_Bmim[BF4] and P_C₄N_{MA,11}[Tf2N] containing an higher concentration of ionic liquid to observe the influence of the concentration on the best performing IL and on the worst one. Figure 3.6 shows the trend of diffusivity, solubility and permeability of the polymerized samples containing an increasing amount of IL from one to six times the normal concentration used so far (i.e. 4.4 mmol/g). The increasing amount of IL in the samples leads to a variation in the gas transport properties. In particular, for what regard Bmim[BF4], all the properties increase up to a maximum point and then decrease. The maximum value of

permeability was reached at a value of 17.6 mmol/g of IL. In the case of C₄N_{MA,11}[Tf₂N], instead, the behaviour is slightly different. In fact, the permeability increases as the IL concentration increases. This aspect can be linked to the different arrangement of the ILs inside the polymer matrix, as it copolymerize with the PEGDA network. Nevertheless, in comparison with neat PEGDA, an increase of permeability and diffusivity was observed in all samples. Finally, the 3D printed cubic structures (Figure 3.3) were tested in the CO₂ capture system to estimate their uptake capacity. Table 3.6 reports the values of the weight percentage variation of the samples before and after the exposition to the gas at 1 bar and 3 bar. The results are not quite similar to the expectations, in fact, sample with neat PEGDA presents higher CO₂ uptake than the other samples containing the ionic liquids. The experimental apparatus of this system can be improved to increase the accuracy of the measurements. For instance, by integrating the pressure chamber with a microbalance to allow simultaneous CO₂ uptake and weight recording.

Table 3.6 Weight percentage increase of samples exposed to CO₂ atmosphere at 1bar and 3bar.

Sample	Weight increase @ 1 Bar	Weight increase @ 3 Bar
PEGDA	0,42	0,87
P_Bmim[BF ₄]	0,24	0,69
P_Bmim[BF ₄] ₂	0,39	0,72
P_Bmim[BF ₄] ₃	0,46	0,63
P_Bmim[BF ₄] ₄	0,32	0,64
P_Bmim[BF ₄] ₆	0,41	0,72
P_Bmim[Tf ₂ N]	0,35	0,21
P_C ₄ N _{MA,11} [Tf ₂ N]	0,29	0,65
P_Bvim [Tf ₂ N]	0,29	0,79

1.4 Conclusion

This work aims to develop new materials that can be processed through DLP 3D printing and that present appealing properties for an application in CO₂ capture technology. Six commercially available ionic liquids with specific anions and cations were chosen according to their applications in CO₂ capture found in literature. The ionic liquids (Bmim[BF₄], Bmim[Tf₂N], Bvim[Tf₂N], Amim[Tf₂N], Bmim[ac] and C₄N_{MA,11}[Tf₂N]) were mixed with a bi-functional

acrylate monomer (PEGDA) in order to have, after the photo-curing process, a solid structure that acted as a support to enhance both chemical and mechanical properties. The formulations, containing Bmim[BF₄], Bmim[Tf₂N], Bvim[Tf₂N] and C₄N_{MA,11}[Tf₂N] gave optimal curing times, similar to the one of neat PEGDA, with particularly good results for the ILs containing a reactive group able to copolymerize with PEGDA, like Bvim[Tf₂N] and C₄N_{MA,11}[Tf₂N]. Those selected ILs were then successfully 3D printed using a DLP system, firstly to create thin membranes with thickness of 150 μm, after to build more complex three-dimensional structure with a hollow cubic shape. Optimal printing results were also achieved by increasing the concentration of ILs in the formulations, up to 26.4 mmol/g.

The 3D printed samples were then tested to investigate their interaction with CO₂. Permeability analysis, carried out on the 3D printed membranes, showed high solubility for samples containing Amim[Tf₂N] IL that, unfortunately, did not get good result in the 3D printing process. Nevertheless, Bmim [BF₄] and Bmim [Tf₂N] samples showed high permeability values, allowing them to be possible candidates for application in SLM technology. FTIR analysis confirmed physical CO₂ adsorption on the samples and desorption cycles were performed both with thermal and vacuum treatment, showing a not complete desorption of the captured gas, suggesting for a more severe treatment. A weighting system for the CO₂ uptake on the 3D printed cubic structures was set up with applied pressures up to 3 bar and IL concentrations up to 26.4 mmol/g. Results showed an increase in weight due to CO₂ absorption proportional to the applied pressure. Unexpectedly, all the samples were not highly performing showed lower absorption capacity than the one with neat PEGDA, maybe due to the decreasing of solubility brought by the presence of this kind of ionic liquids in the polymer matrix.

The results are promising, especially for an application of these materials in the SLM technology, where permeability plays a crucial role. Further in-depth analysis will be necessary to clarify the aspects described in this paper. One of the limitations of the work is the use of only one polymer and a restrict range of ionic liquid samples. Future work will be done to analyze new ionic liquids-based materials to identify the most promising one for CO₂ capture and separation, as well to improve the CO₂ uptake measurement system.

Chapter 4

3D printing of synthesized Poly Ionic Liquids for CO₂ capture

1.1 Introduction

Following the work described in Chapter 3, where formulations containing a mixture of PEGDA and ionic liquids were successfully 3D printed, a step forward was made in the same direction. This chapter presents an ongoing study, carried out in the research group of Prof. Sans Sangorrin at the University of Nottingham, centered on the synthesis of new ionic liquids characterized by reactive groups able to co-polymerize and by specific CO₂-philic ionic species. Since the work is still not entirely complete, some results need to be fully interpreted and further studies will be considered for the future.

As already mentioned in Chapter 1, section 1.3, ionic liquids (ILs) are salts characterized by a very low melting point. This effect is caused by the presence of large and asymmetric ions, which, interacting with each other with hydrogen bonds, disturb the coulomb interaction, increasing the dynamics between ions (248). ILs are also characterized by an extremely low vapor pressure that renders them useful in green chemistry (249). Among the many applications in which ILs are employed, CO₂ capture is one of the most studied topics in the last years. In fact, ILs can interact with CO₂ in different ways and its solubility can be tuned by modifying some properties, such as Lewis acid-base interactions, molecular rearrangements, free volume in the material and chemical interactions. A near-infinite amount of ionic liquids can be created, because composed by different combinations of ions: in this work, the anions and cations were chosen specifically to create a molecule that was able to photo-polymerize and to possess a high CO₂ solubility. Here, all the ionic liquids were synthesized starting from an imidazole moiety: many studies showed that imidazolium-based ILs possess superior CO₂ adsorption due to a remarkable solubility (132, 136, 250-252). Furthermore, it was demonstrated that the increase of the length of the alkyl chain in the cation could slightly increase CO₂ solubility (253, 254). For that reason, the ILs were synthesized with two different molecular arrangements, bearing two different alkyl chains, one linear and a longer branched one. The anion plays a crucial role in the CO₂ capture process as well, since many studies reported different CO₂ solubility of ionic liquids with the same cation but different anions (255). In particular, fluorinated anions were found to be more likable to interact with CO₂ than other anions (256) and

bis(trifluoromethanesulfonyl)imide (TFSI) anion generally gives the highest CO₂ solubility among most of the cations. The high CO₂ solubility can also be attributed to the flexibility of the structure of TFSI, aiming at increasing the free volume and decreasing the energy of cavity formation in the host material (257). For this reason, TFSI was used as counter ion in the synthesized ILs. To study different combinations of anions, aiming to increase the ability of the IL to interact with CO₂, ILs with Acetate anions were also synthesized. In fact, Acetate ILs are known to form complex intermediates with CO₂ due to a Lewis acid base reaction, giving rise to a high CO₂ solubility (258). In order to have the possibility to photo-polymerize and 3D print the ILs, a reactive functionality was added to the ILs cation. In particular, a vinyl group was grafted by quaternization reaction to the imidazole ring, with the primary role of reacting through a photo induced free-radical polymerization and copolymerize with PEGDA to obtain a cross-linked polymerized ionic liquid (PIL).

Firstly, the synthesis and characterization through NMR technique will be presented. Afterwards, a polymerization study on the formulations containing PEGDA and the synthesized ILs with different ratios will be shown presenting photo-rheology, FTIR analysis and UV-curing tests. A study on the control over the matrix porosity by introducing different additives was also carried out with the aim of increasing the CO₂ interaction by incrementing the surface to volume ratio. Two ways were adopted: the first using a long chain PIL (Poly(diallyldimethylammonium) bis(trifluoromethanesulfonyl)imide (PDADMA TFSI) to increase the free volume in the polymer matrix and the second by ionic complexation using Pyromellitic Acid (PMA) that can trigger an electrostatic complexation between imidazolium based PILs and the multivalent benzoic acid (259). Characterization analysis, such as UV-visible, permeability, TGA, DSC, and N₂ isotherm will be shown on the polymerized formulations containing these additives in different concentrations to investigate their effects. After the characterization analysis, the prepared formulations were loaded in the 3D printer to build simple structures. The 3D printed structures were finally tested in high-pressure CO₂ atmosphere to investigate their CO₂ uptake capacity.

1.2 Experimental and methods

1.2.1 Materials

For the ionic liquids' synthesis, 2-methyl imidazole, purchased from Sigma Aldrich, was used as starting materials for all the synthesized ILs. 1-bromobutane and 1-bromo-3,3-dimethylbutane, purchased from Tokyo Chemical Industry, were employed as precursors for the alkyl chain reaction, while 4-vinylbenzyl chloride was used for the linking of the reactive group. Potassium hydroxide was used to deprotonate the imidazolium ring during the alkyl chain reaction, while anhydrous magnesium sulfate was necessary for dehydrate the solution, both were purchased from Sigma Aldrich; lithium bis(trifluoromethylsulfonyl)imide was used for TFSI

ion exchange, AMBERLITE_IRA 402 (OH) was used for OH ion exchange, sodium hydroxide and acetic acid was used for Acetate ion exchange, acetonitrile, dichloromethane, acetone and diethyl ether were purchased from Sigma Aldrich. Polyethylene glycol diacrylate (PEGDA) with average molecular weight 250, purchased from Merck, was used as constituent monomer and cross-linker. Phenylbis(2,4,6-trimethylbenzoyl)phosphine oxide (BAPO) powder 97% purity, purchased from IGM Resins, was employed as photo-initiator to start the free radical reaction and 1-Phenylazo-2-naphthol-6,8-disulfonic acid disodium salt (orange G), used as a dye in the 3D printable formulations, was purchased from Tokyo Chemical Industry. Pyromellitic acid (PMA) was purchased from Tokyo Chemical Industry.

1.2.2 Ionic liquids synthesis

2-methyl-3-butylimidazole

The first synthesis process consists in the deprotonation of the nitrogen site of the imidazole ring, by inserting in the solution a base (potassium hydroxide), to react with the linear alkyl chain precursor (1-bromobutane). During the reaction, acetonitrile was used as solvent and inert atmosphere was maintained to prevent any oxidation process. The final compound will be the imidazole with the linear alkyl chain attached to the nitrogen, with potassium bromide and water as side products. Purification processes followed the reaction. The synthesis steps are described here (see figure 4.1 for the schematized reaction). 6 g of 2-methylimidazole were dissolved in 90 ml of acetonitrile in a two-neck round bottom flask and stirred for 15 minutes. Afterwards, 8 g of potassium hydroxide were added to the solution and stirred for further 30 minutes. Subsequently 8 ml of 1-bromobutane were added dropwise to the solution in argon atmosphere and stirred for 4 hours at room temperature. The solvent was removed under dynamic vacuum. The compound was extracted three times in 300 ml dichloromethane and washed three times with 600 ml of distilled water. The solution was dried with anhydrous magnesium sulfate and, finally, dichloromethane was removed under dynamic vacuum. A yellowish oil was obtained as final compound (Yield 70%). ¹H NMR (400MHz, Acetone-d₆) δ 0.94 (t, 3H, CH₃), 1.35 (dq, 2H, CH₂), 1.71 (m, 2H, CH₂), 2.3 (s, 3H, CH₃), 3.91 (t, 2H, CH₂), 6.75 (s, 1H, C=CH), 6.95 (s, 1H, C=CH).

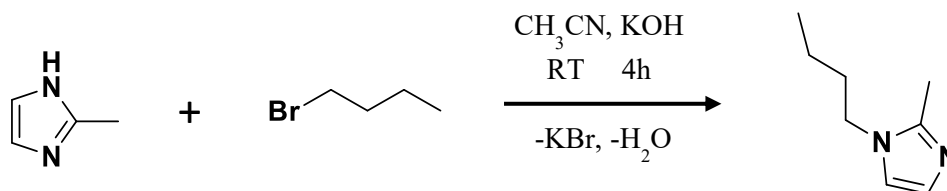


Figure 4.1 reaction scheme for 2-methyl-3-butylimidazole.

1-(4-vinylbenzyl)-2-methyl-3-butylimidazolium chloride

The next synthesis consists in the quaternization reaction of 2-methyl-3-butylimidazole with 4-vinylbenzyl chloride used as precursor for the attachment of the vinyl group to make the IL suitable for polymerization. In this case, the reaction was performed using the two neat compounds without any solvent, in inert atmosphere to prevent any oxidation process, and in dark environment, to avoid premature reaction of the vinyl group since 4-vinylbenzyl chloride is light sensible.

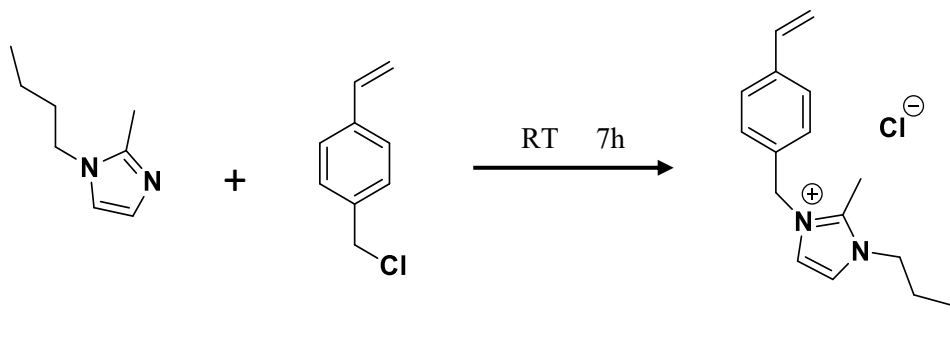


Figure 4.2 reaction scheme for C4vbmim₋Cl.

The final raw compound is a solid ionic liquid with chloride as anion. Purification processes followed the reaction. The synthesis steps are described here (see figure 4.2 for the schematized reaction). 4.85 g of 2-methyl-3-butylimidazole and 5 ml of 4-vinylbenzyl chloride were mixed dropwise in argon atmosphere in a two-neck round bottom flask. The reaction was let stir for 7 hours. Subsequently, the crude compound was dissolved in acetone and precipitated with diethyl ether (500 ml) three times. The final powder was filtrated and the solvents evaporated under dynamic vacuum (yield 72%). ¹H NMR (400MHz, DMSO-d₆) δ 0.91 (t, 3H, CH₃), 1.28 (dq, 2H, CH₂), 1.72 (m, 2H, CH₂), 2.63 (s, 3H, CH₃), 4.12 (t, 2H, CH₂), 5.31 (dd, 1H, C=CH₂), 5.41 (s, N⁺-CH₂), 5.87 (dd, 1H, C=CH₂), 6.75 (dd, 1H, C=CH₂), 7.31 (m, 2H, HC=C=CH), 7.52 (m, 2H, HC=C=CH), 7.76 (m, 2H, HC=CH).

1-(4-vinylbenzyl)-2-methyl-3-butylimidazolium bis(trifluoromethanesulfonyl)imide

The next step concerns the anion exchange between chlorine and TFSI, to create C4vbmim₋TFSI (molecular structure in Table 4.1). This was made by mixing the obtained 1-(4-vinylbenzyl)-2-methyl-3-butylimidazolium chloride with TFSI precursor Lithium bis(trifluoromethylsulfonyl)imide salt. The procedure follows the steps described here. 1-(4-vinylbenzyl)-2-methyl-3-butylimidazolium chloride and 1.2 molar equivalent of Lithium bis(trifluoromethylsulfonyl)imide were dissolved in distilled water in two separate beakers. The solutions were mixed together and stirred for 30 minutes. The upper phase (water rich) was washed (extraction) with dichloromethane three times and mixed with the bottom phase (ionic liquid rich). The solution was washed with water three times and dried over anhydrous magnesium sulfate. Subsequently the solvent was evaporated under dynamic vacuum and a transparent oil was obtained (Yield: 90%). The process was

performed in dark environment to prevent the polymerization of the ionic liquid induced by light exposure.

1-(4-vinylbenzyl)-2-methyl-3-butyliimidazolium acetate

The second synthesized ionic liquid was the linear alkyl chain cation with acetate as counter ion (C4vbmim_Ac, see molecular structure in Table 4.1). The synthesis process was the ion exchange between chlorine and acetate of 1-(4-vinylbenzyl)-2-methyl-3-butyliimidazolium chloride. For this reaction, an intermediate step was required, where chloride was first substituted by OH⁻ through an ion exchange column. This was done with the aim of avoiding the direct ion exchange from Cl⁻ to Ac⁻ that would generate a salt as side product (e.g. NaCl by using sodium acetate as precursor) that could be hardly removed. The process was performed as follows: a column (100 g AMBERLITE_IRA 402 (OH)) was washed with 1 l of sodium hydroxide 1M and drained dropwise. Subsequently, the column was washed with 1 l of deionized water until the pH of the drained solution became neutral. C4vbmim_Cl was dissolved in water and poured dropwise in the column. After that, water was added slowly through the column washing it until the drained solution became basic. At that moment, the compound was collected dropwise in a round bottom flask until the pH became neutral again. Afterward, 1.2 molar equivalent of acetic acid was added to the basic solution and stirred until it became neutral. The water was evaporated and the compound dissolved in acetone. The solution was then precipitated with diethyl ether and the solvent evaporated.

2-methyl-3-3,3-dimethylbutylimidazole

2-methyl-3-3,3-dimethylbutylimidazole was synthesized, as for 2-methyl-3-butyliimidazole, by deprotonating the nitrogen of the imidazole ring and making it react with the precursor for the branched alkyl chain (1-bromo-3,3-dimethylbutane). Again, potassium bromide and water were left as side product of the reaction. A final purification process was made to clean the target product. The reaction process is reported here (see figure 4.3 for the sketch of the reaction). 6 g of 2-methylimidazole were dissolved in 90 ml of acetonitrile and stirred for 15 minutes in a two-neck round bottom flask, 8 g of potassium hydroxide were added to the solution and stirred for 30 minutes. Subsequently 8 ml of 1-bromo-3,3-dimethylbutane were added dropwise to the solution in argon atmosphere and stirred for 4 hours at room temperature. The solvent was removed under dynamic vacuum. The compound was extracted three times in 300 ml dichloromethane and

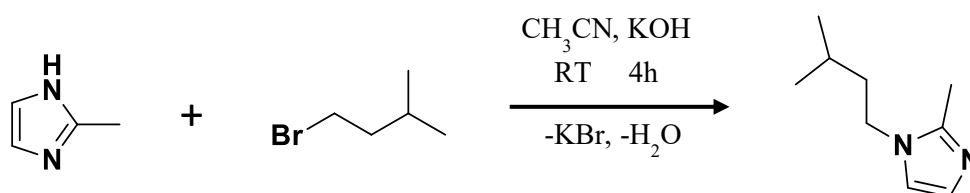


Figure 4.3 reaction scheme for 2-methyl-3-3,3-dimethylbutylimidazole.

washed three times with 600 ml of deionized water. The solution was dried over anhydrous magnesium sulfate and, finally, dichloromethane was removed under dynamic vacuum. A yellowish oil was obtained as final compound (Yield: 75%). ¹H NMR (400MHz, Acetone-d₆) δ 0.97 (m, 6H, H₃C-C-CH₃), 1.61 (m, 3H, CH₂, CH), 2.3 (s, 3H, CH₃), 3.92 (m, 2H, CH₂), 6.75 (d, 1H, C=CH), 6.96 (s, 1H, C=CH).

1-(4-vinylbenzyl)-2-methyl-3-3,3-dimethylbutylimidazolium chloride

Starting from 2-methyl-3-3,3-dimethylbutylimidazole, the ionic liquid with the chloride as counter-ion was synthesized by reacting it with 4-vinylbenzyl chloride as for the synthesis of C4vbmim₋Cl. The reaction was performed by mixing the two reagents without solvent in dark environment and inert atmosphere to prevent any oxidation. The synthesis procedure is described here (see figure 4.4 for the reaction sketch). In a two-neck round bottom flask were mixed 4.85 g of 2-methyl-3-3,3-dimethylbutylimidazole and 5 ml of 4-vinylbenzyl chloride dropwise in argon atmosphere. The reaction was let stir for 7 hours. Subsequently, the crude compound was dissolved in acetone and precipitated with diethyl ether (500 ml) three times. The final powder was filtrated and the solvents were evaporated under dynamic vacuum (yield: 80%). ¹H NMR (400MHz, DMSO-d₆) δ 0.85 (d, 6H, H₃C-C-CH₃), 1.51 (dp, 1H, CH), 1.62 (m, 2H, CH₂), 2.50 (s, 3H, CH₃), 4.05 (m, 2H, CH₂), 5.26 (s, 2H, N⁺-CH₂), 5.28 (d, 1H, C=CH₂), 5.79 (dd, 1H, C=CH₂), 6.71 (dd, 1H, C=CH), 7.19 (m, 2H, HC-C=CH), 7.31 (d, 1H, C=CH), 7.35(d, 1H, C=CH), 7.46 (m, 2H, HC-C=CH).

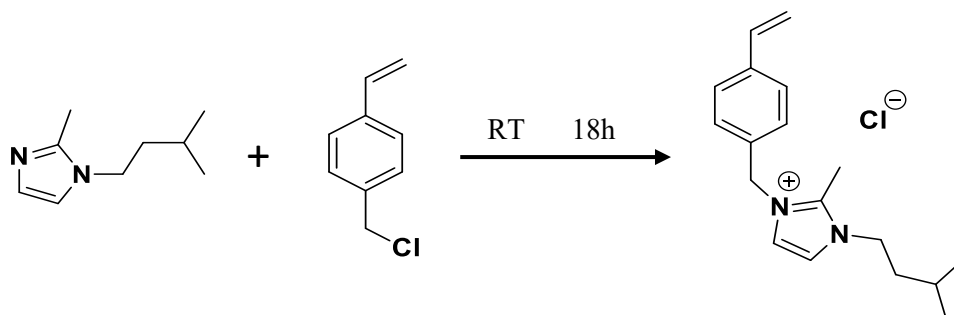


Figure 4.4 reaction schematic for (iPr)C2vbmim₋Cl.

1-(4-vinylbenzyl)-2-methyl-3-3,3-dimethylbutylimidazolium bis(trifluoromethanesulfonyl)imide

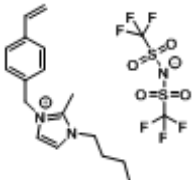
(iPr)C2vbmim₋Cl was modified by exchanging the anion from chlorine to TFSI in order to obtain the third ionic liquid, that is (iPr)C2vbmim₋TFSI as shown in Table 4.1. The reaction follows the same steps described for the synthesis of C4vbmim₋TFSI. 1-(4-vinylbenzyl)-2-methyl-3-3,3-dimethylbutylimidazolium chloride and 1.2 molar equivalent of Lithium bis(trifluoromethylsulfonyl)imide were dissolved in water in two separate beakers. The solutions were mixed together and stirred for 30 minutes. The upper phase (water rich) was washed (extraction) with dichloromethane three times and mixed with the bottom phase (ionic liquid rich). The solution was washed with water three times and dried over anhydrous

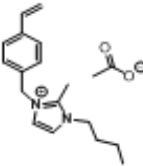
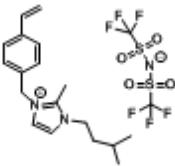
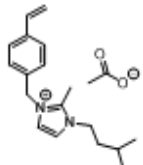
magnesium sulfate. Subsequently the solvent was evaporated under dynamic vacuum. At the end, a transparent oil was obtained (Yield: 95%).

1-(4-vinylbenzyl)-2-methyl-3,3,3-trimethylbutylimidazolium acetate

The last synthesized ionic liquid is the branched chain cation with acetate as anion ((iPr)C2vbmim_Ac, see Table 4.1). The ion exchange was made again through an ion exchange column filled with AMBERLITE_IRA 402 beads, to make the first OH⁻ ion exchange step and then by neutralizing the solution with acetic acid and make the last exchange with acetate anion. The procedure is reported here. A column (100 g AMBERLITE_IRA 402 (OH)) was washed with 1 l of sodium hydroxide 1M and drained dropwise. Subsequently, the column was washed with 1 l of deionized water until the pH of the drained solution became neutral. (iPr)C2vbmim_Cl was dissolved in water and poured dropwise in the column. After that, water was added slowly through the column washing it until the drained solution became basic. At that moment, the compound was collected dropwise in a round bottom flask until the pH became neutral again. Afterward, 1.2 molar equivalent of acetic acid was added to the basic solution and stirred until it became neutral. The water was evaporated and the compound dissolved in acetone. The solution was then precipitated with diethyl ether and the solvent evaporated.

Table 4.1 list of synthesized ionic liquids with molecular structure and abbreviations.

IL	Abbreviation
<p>1-(4-vinylbenzyl)-2-methyl-3-butylimidazolium bis(trifluoromethanesulfonyl)imide</p> 	<p>C4vbmim_TFSI</p>

<p>1-(4-vinylbenzyl)-2-methyl-3-butylimidazolium acetate</p> 	<p>C4vbmim_Ac</p>
<p>1-(4-vinylbenzyl)-2-methyl-3,3,3-trimethylbutylimidazolium</p> 	<p>(iPr)C2vbmim_TFSI</p>
<p>1-(4-vinylbenzyl)-2-methyl-3,3,3-trimethylbutylimidazolium acetate</p> 	<p>(iPr)C2vbmim_Ac</p>

1.2.3 Formulations and sample fabrications

The aim of the work was to create a formulation that was photo-curable and 3D printable; for that reason, a vinyl group, able to participate to the photopolymerization reaction, was added to all the synthesized ILs. Nevertheless, the mono-functional vinyl group present in the IL is not sufficient to achieve the desired mechanical properties needed for a self-standing structure. Furthermore, since a 3D printer with a DLP system is used, a thermoset polymer will be produced. For this reason, PEGDA (M_n 250) was used as co-polymer and cross-linker. Different formulations were prepared based on the typology of the sample characterization. Initially, formulations containing a high amount of IL were obtained to create thin membranes easy to manufacture and to handle. BAPO was used as photo-initiator for the photo-induced polymerization reaction with a concentration of 1 wt% with respect to the amount of the photocurable monomers. A typical formulation is resumed below.

- PEGDA (M_n 250): 20 mol%

- IL: 80 mol%
- BAPO: 1 %wt

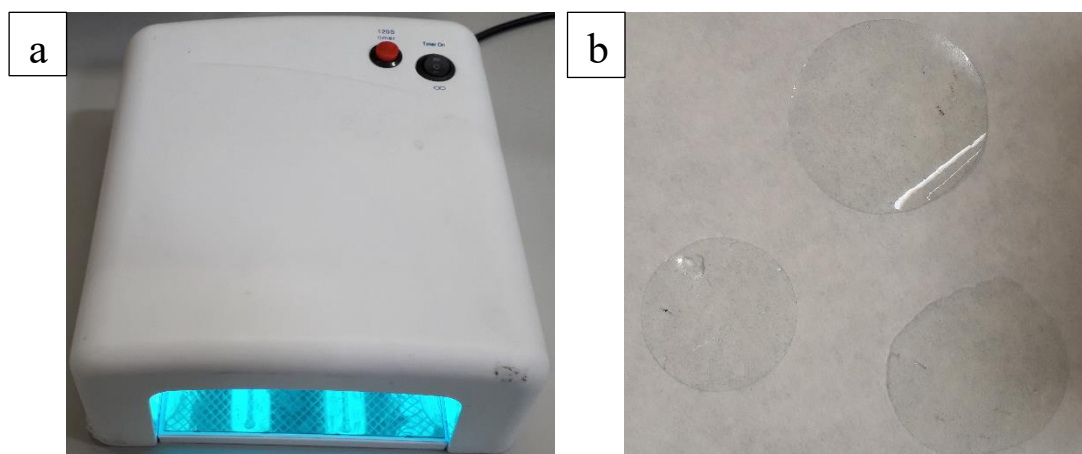


Figure 4.5 (a) UV lamp used for the photo-curing process and (b) prepared photo-cured membranes by UV polymerization.

Few drops of formulation were clamped between two glass plates covered by a layer of Teflon used to prevent the sticking of the polymerized resin on the glass. The photo-curing process was performed by irradiating the samples with a UV-lamp for 2 minutes (see Figure 4.5a). As final result, circular membranes with thickness ranging from 50 μm to 200 μm were obtained (see Figure 4.5b). The membranes, after curing, were easily detached from the Teflon surface and carefully washed with isopropyl alcohol. The next step was to prepare the formulations in such a way that they were suitable to be 3D printable in a DLP apparatus. A dye (see Figure 4.6) was added in the formulation in order to achieve more accuracy during the printing by reducing light scattering. Furthermore, the IL/PEGDA ratio was reduced to 60/40 mol% to produce more cross-linked network compatible with 3D printing. The formulation composition is reported below.

- PEGDA (M_n): 40 mol%
- IL: 60 mol%
- BAPO: 1 %wt
- Dye (Orange G): 0.1 %wt

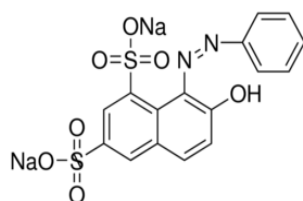


Figure 4.6 molecular structure of Orange G

The 3D printer used in this study was a DLP type LittleRP 3D printer . An Acer P1500 projector was used as the 3D printer light source and it was equipped with an OSRAM lamp (210 W). The formulation was pured in the plastic tray and the build plate was lowered into the resin against the transparent teflon film. At this point the Creation Workshop RC36 software started the projection, layer per layer,

of the loaded object CAD until the printing was finished. The slice thickness was set to 50 μm and the curing times were adjusted to 6s for the burn-in time, the initial base printing (200 μm), and 1.5s for the normal time, the exposure time for the rest of the structure. The final object was finally washed with isopropyl alcohol and post-cured in the UV-lamp for 2 minutes to complete the polymerization.

1.2.4 Material characterization

Firstly, the synthesized ionic liquids were characterized by means of NMR. The samples (6 μl) were solubilized in a deuterated solvent to avoid interference with the sample spectra and poured in a NMR tube. NMR technique was employed to finely characterize the synthesized molecules by knowing the exact amount of each kind of atoms present in it. ^1H NMR spectra were recorded on a Bruker AVX400 (400 MHz) spectrometer at ambient temperature. ^{13}C NMR spectra were recorded on a Bruker AVX400 (101 MHz) spectrometer at ambient temperature. ^{19}F NMR spectra were recorded on a Bruker AVX400 (376 MHz) spectrometer at ambient temperature. Once the ionic liquids were chemically characterized, their viscosity was calculated by testing them through rheological measurements. Real-time rheological measurements were performed using an Anton Paar rheometer (Physica MCR 302). The gap between the rotating plates was set to 100 μm , which is the nominal thickness chosen for this kind of measurements, to have a good signal to noise ratio. For all the measurements, the temperature was fixed at 25 $^\circ\text{C}$, at a constant shear frequency of 3.18 rad/s at 1% of amplitude. The parameters of frequency and amplitude were chosen based on the stress-relaxation signal response and they are closely related to the material under investigation. At higher frequencies the elastic modulus is predominant, while at lower frequencies the situation is reversed and the viscous properties of the material become dominant. A good trade-off needs to be found to study the mechanical properties of the desired material. After this characterization on the neat ILs, the reactivity of the photocurable formulations described in section 1.2.3 was studied. FTIR-ATR was employed to investigate the conversion of the double bond (vinyl and acrylic) during light irradiation. Samples containing IL/PEGDA ratio of 100/0, 80/20, 40/60 and 0/100 mol%, from 0s to 120s were analyzed to understand the different behaviors of polymerization at different concentration of IL and different exposures times. The measurements were done by polymerizing each sample, as described in section 1.2.3, for the desired amount of time under the UV lamp and analyzing in the FTIR-ATR apparatus in dark room to avoid further polymerization during the measurement. Afterwards, photo-rheological analyses were carried out on the formulations containing the ILs. Anton Paar rheometer (Physica MCR 302) in parallel plate mode with a Hamamatsu LC8 visible lamp with power intensity of 10 mW/cm^2 (10% of maximum) and a cut-off filter below 400 nm equipped with 8 mm light guide was used for the measurements. The lamp was turned on after a waiting time of one minute in order to leave enough time to have a stable signal. The outcome data consist in a plot of the elastic (G') and loss (G'') modulus and

their ratio versus time. At this point, the formulations were modified by the addition of two different additives to introduce a porosity in the polymer matrix. Long chain PIL (Poly(diallyldimethylammonium) bis(trifluoromethanesulfonyl)imide (PDADMA_TFSI) was used to increase the free volume in the polymer matrix and Pyromellitic Acid (PMA) to create porosity by ionic complexation. In the first case, uv-visible analysis was carried out on formulations containing 0 %wt, 6 %wt and 20 %wt of PDADMA_TFSI in order to see their effect on the light absorption due to the emulsion between PEGDA and PDADMA_TFSI. The UV-visible spectra were collected with a Varian Cary-500 spectrophotometer in the range between 300 nm and 800 nm, with a resolution of 1 nm, monitored with a scan rate of 480 nm/min. Permeability measurements were also carried out on the photo-cured membranes with different concentrations of the PIL, to investigate gas transport properties variation by introducing a porosity in the material. The measure was performed at 25 °C and 0% relative humidity. Description of the permeability measurement apparatus is described in Chapter 2 section 1.2.3. In the second case, formulations were prepared containing different amount of Pyromellitic acid (PMA) in molar ratio of 1:4, 1:1 with respect to the imidazole, corresponding to 6 wt%, 25wt% of the whole formulation. Thin membranes were photo-polymerized with the method described in section 1.2.3, swelled in water and neutralized in NaOH solution 0.01M. TGA and DSC analysis were carried out on the membranes with and without pyromellitic acid to see the stability of the membranes at higher temperatures. Measurements were performed with a TA Instruments Q600, simultaneous thermo-gravimetric and differential thermal analysis (DSC/DTA). TGA analysis were performed from 0 °C to 400°C with a scan rate of 30°C/min. DSC measurements were carried out from -50 °C to 200 °C with a scan rate of 10 °C/min. Nitrogen isotherms were carried out on membranes containing 0 %wt, 6 %wt and 25 %wt of PMA. Permeability analysis were performed as well on the membrane with and without PMA to see the transport gas behavior within the polymer matrix if a porosity was created. Finally, the 3D printed structures containing the two PILs and 6 %wt and 25 %wt of PMA were tested to the CO₂ uptake. The CO₂ uptake measurements (25 °C, 0–40 bar) were performed with a Hiden XEMIS intelligent gravimetric analyzer. Prior to CO₂ uptake determination, the samples were outgassed under vacuum at 250 °C typically overnight.

1.3 Results and discussion

1.3.1 Ionic liquids and formulations characterization

The overall reactions' yields for the synthesis of the chloride ILs (C4vbimim_Cl and (iPr)C2vbimim_Cl) were over 70 %, while the TFSI ion exchange yield was over 90% for all the reactions. Problems arose with the acetate ion exchange, since after the ion exchange column process and the removal of the solvent, the compound started to polymerize, becoming solid and insoluble in all the available solvents. This effect was observed all the times the process was repeated.

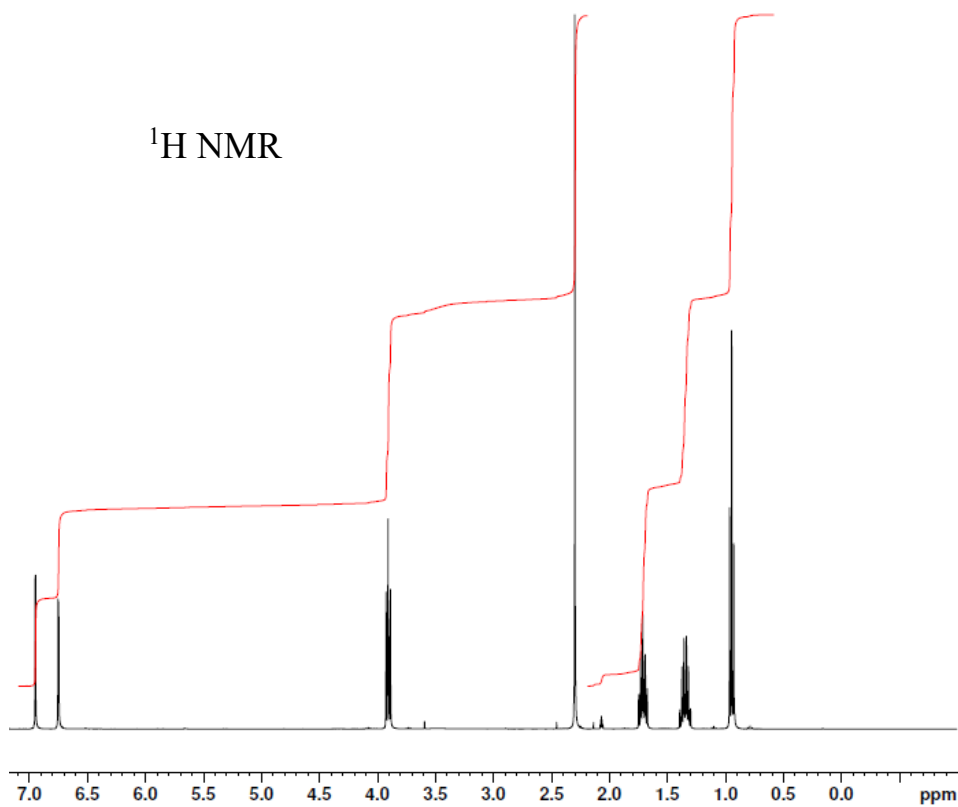


Figure 4.7 ^1H NMR (400 MHz) of 2-methyl-3-butylimidazole in Acetone- d_6 .

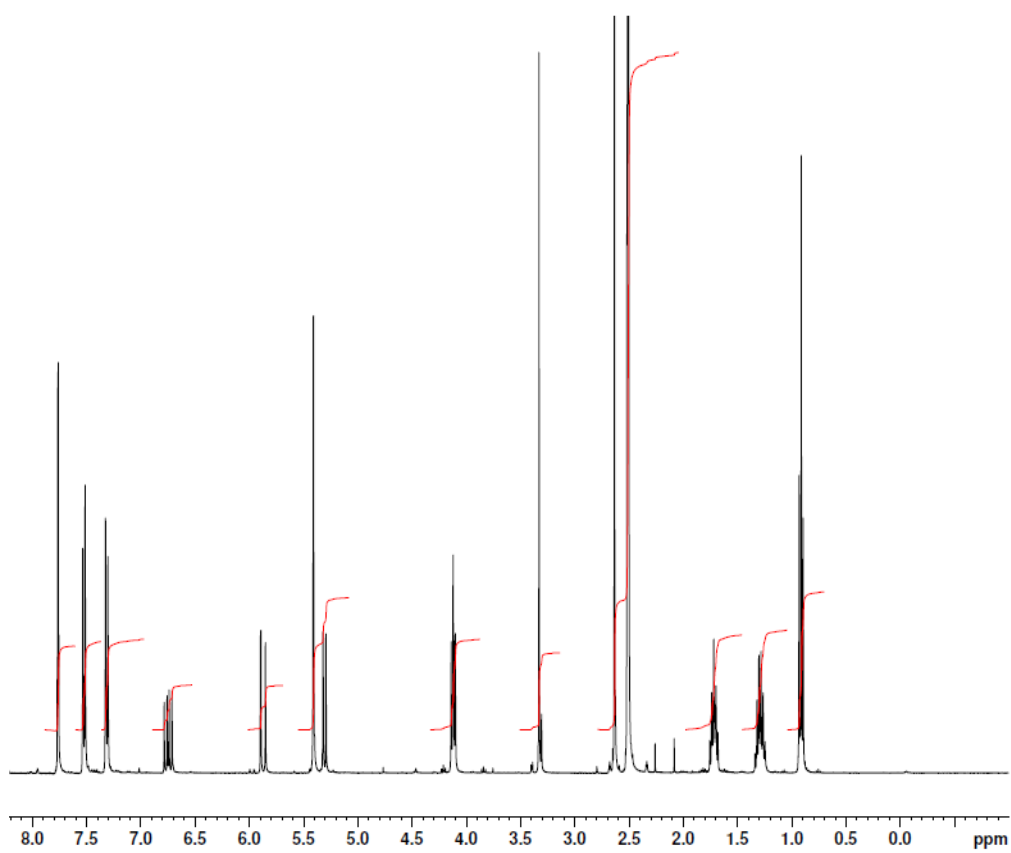


Figure 4.8 ^1H NMR (400 MHz) of C4vbmim-Cl in DMSO- d_6 .

For this reason, C4vbmim_Ac and (iPr)C2vbmim_Ac were not included in the study for further analysis. The synthesized ionic liquids were analyzed in the NMR apparatus to investigate their chemical composition. ^1H NMR and ^{13}C NMR were done on the final compounds of all the reactions steps, ^{19}F NMR was carried out on the ILs containing the TFSI anion. Figure 4.7 shows the ^1H NMR spectrum of 2-methyl-3-butylimidazole in Acetone- d_6 . It is clearly visible, in the range between 1 ppm and 4 ppm, the presence of the multiplets generated by the hydrogen protons of the alkyl chain. In particular, the triplet at 0.94 ppm is ascribable to the methyl group at the end of the alkyl chain, while the three multiplets at 1.35 ppm, 1.71 ppm and 3.91 ppm correspond to the remaining H-C-H groups. At 2.3 ppm is clearly visible the singlet corresponding to the methyl group present on the imidazole ring. Whereas, the two duplets at 6.75 ppm and 6.95 ppm are ascribable to the protons of the C-H group attached to the imidazole ring. The second step reaction is the synthesis of C4vbmim_Cl, created by quaternization reaction between 2-methyl-3-butylimidazole and the vinyl benzene precursor, leaving Cl^- as counter ion. Figure 4.8 displays the ^1H NMR spectrum of C4vbmim_Cl dissolved in DMSO- d_6 . From the graph, it is possible to observe that the peaks described for the NMR spectrum of 2-methyl-3-butylimidazole are all still present. The only difference is a little shift for the peaks corresponding to the methyl group (2.63 ppm) and the C-H (7.76 ppm) of the imidazole ring because of the perturbation brought by hydrogen atoms present in the vinyl-benzene group. In order, from right to left, at 5.31 ppm and 5.87 ppm two duplet corresponding to the protons of the CH_2 of the vinyl group. At 5.41 ppm it is visible the singlet corresponding to the two protons of H-C-H group close to the nitrogen (N^+). Centered at 6.75 ppm it appears the quadruplet ascribable to the proton of C-H of the vinyl group and at 7.31 ppm and 7.52 ppm the protons of the benzene ring generate the two duplets. C4vbmim_Cl was then processed by exchanging the chlorine ion with TFSI through the process described in section 1.2.2. Figure 4.9 displays the ^1H , ^{13}C and ^{19}F NMR spectra of C4vbmim_TFSI dissolved in DMSO- d_6 . The results show that the spectrum of protons NMR remains the same as for C4vbmim_Cl, and a peak in ^{19}F NMR spectrum appears now at 79 ppm for the presence of the TFSI ion, that carries six fluorine atoms. For the synthesis of the second ionic liquid ((iPr)C2vbmim_TFSI), the first step was to create the cation bearing the branched alkyl chain (2-methyl-3-3,3-dimethylbutylimidazole). Figure 4.10 displays the ^1H NMR spectrum of 2-methyl-3-3,3-dimethylbutylimidazole in acetone- d_6 . From right to left, at 9.97 ppm it is visible the multiplet corresponding to the two methyl group (CH_3) on the tail of the alkyl chain. At 1.61 ppm there is the multiplet generated by the three protons (C-H and CH_2) on the alkyl chain. At 2.3 ppm the singlet corresponding the methyl group on the imidazole ring is visible. At 3.92 ppm it is visible the multiplet of the last CH_2 group of the alkyl chain and at 6.75 ppm and 6.96 ppm the double peaks related to the two protons of the imidazole ring are present. The next reaction involved the linking of the vinyl-benzyl group to the 2-methyl-3-3,3-dimethylbutylimidazole molecule. Figure 4.11 shows the ^1H NMR spectrum of (iPr)C2vbmim_Cl in DMSO- d_6 .

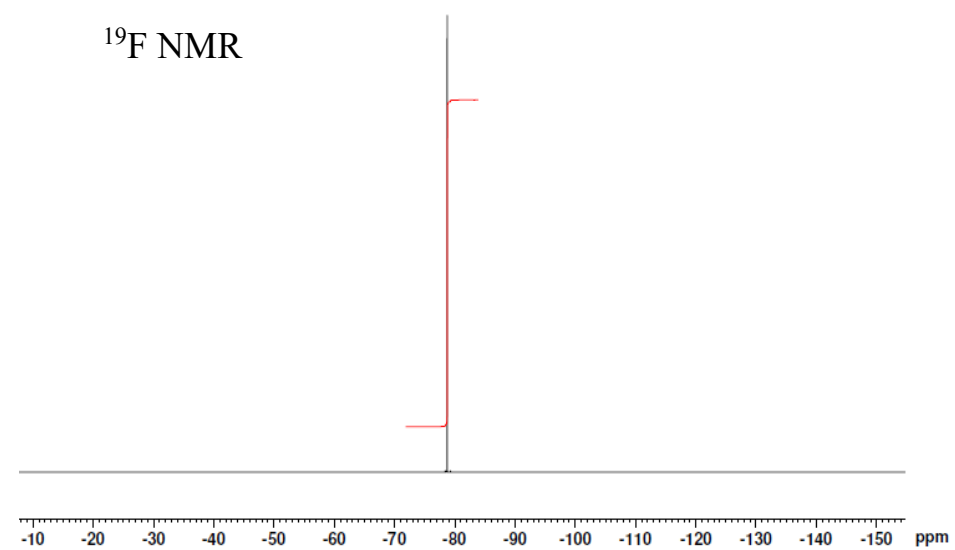
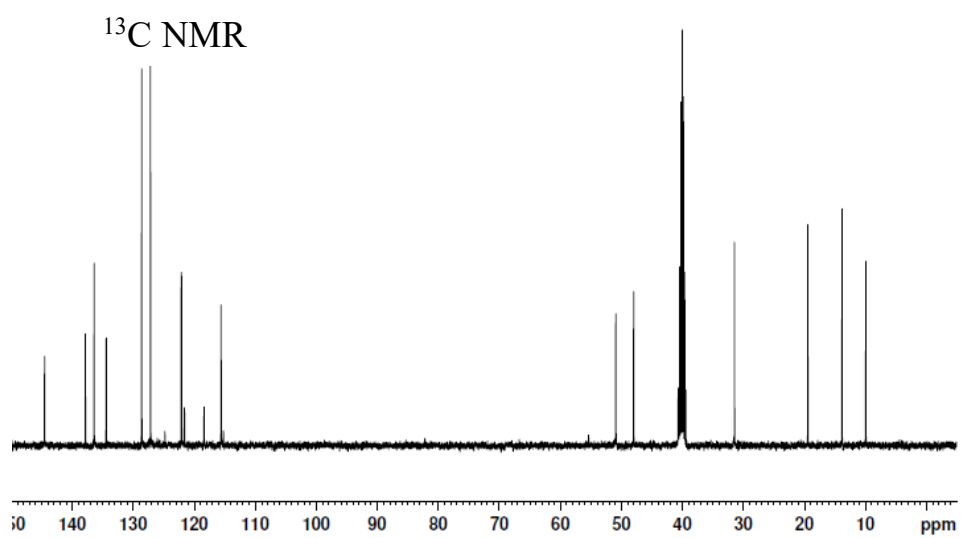
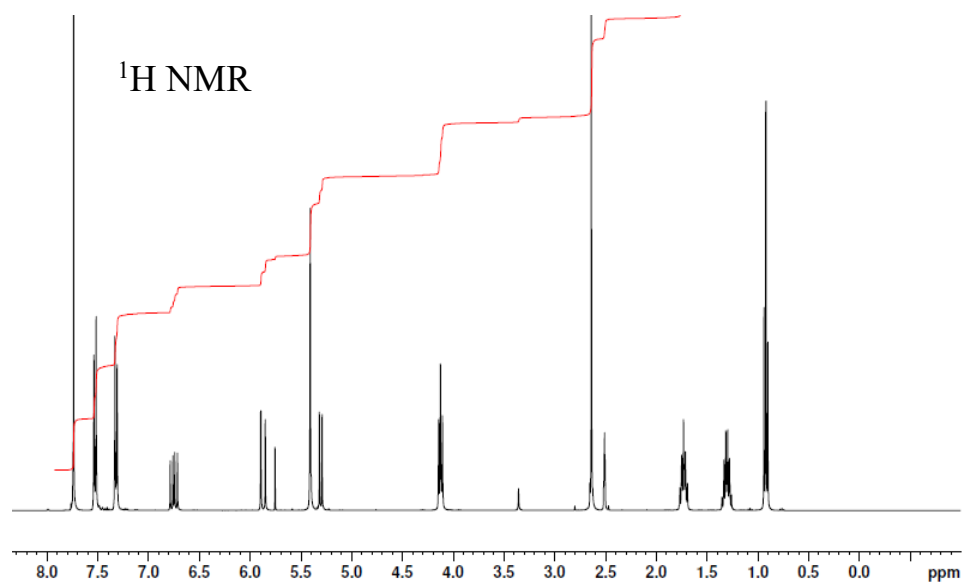


Figure 4.9 ^1H , ^{13}C and ^{19}F NMR spectra of C4vbim_TFSI in DMSO-d₆.

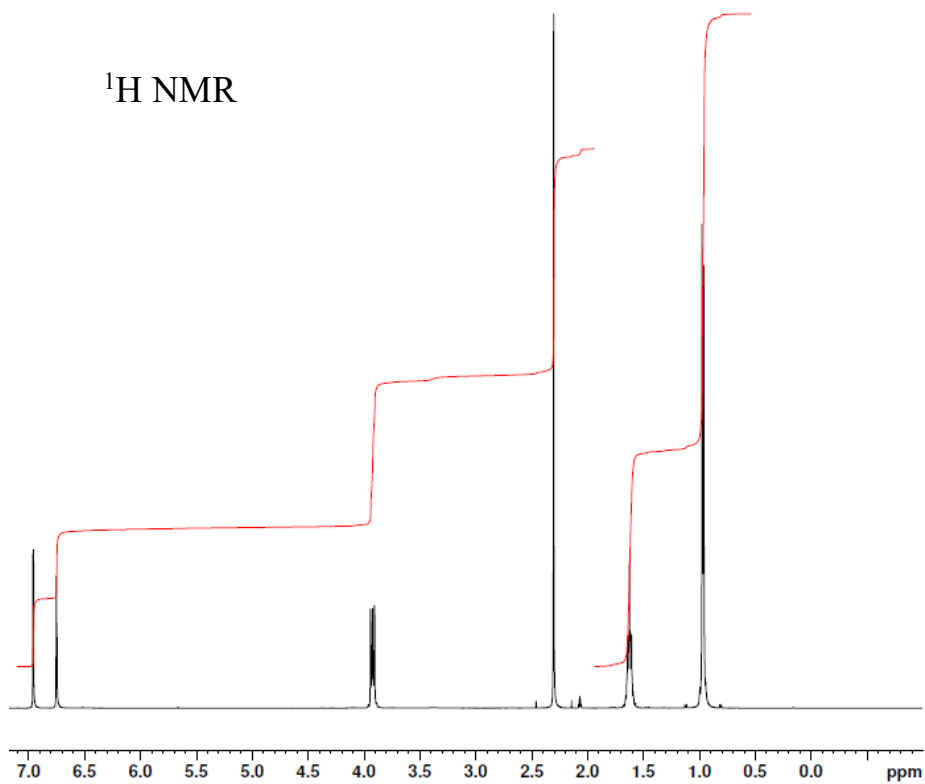


Figure 4.10 ^1H NMR (400 MHz) of 2-methyl-3,3,3-trimethylbutylimidazole in acetone- d_6 .

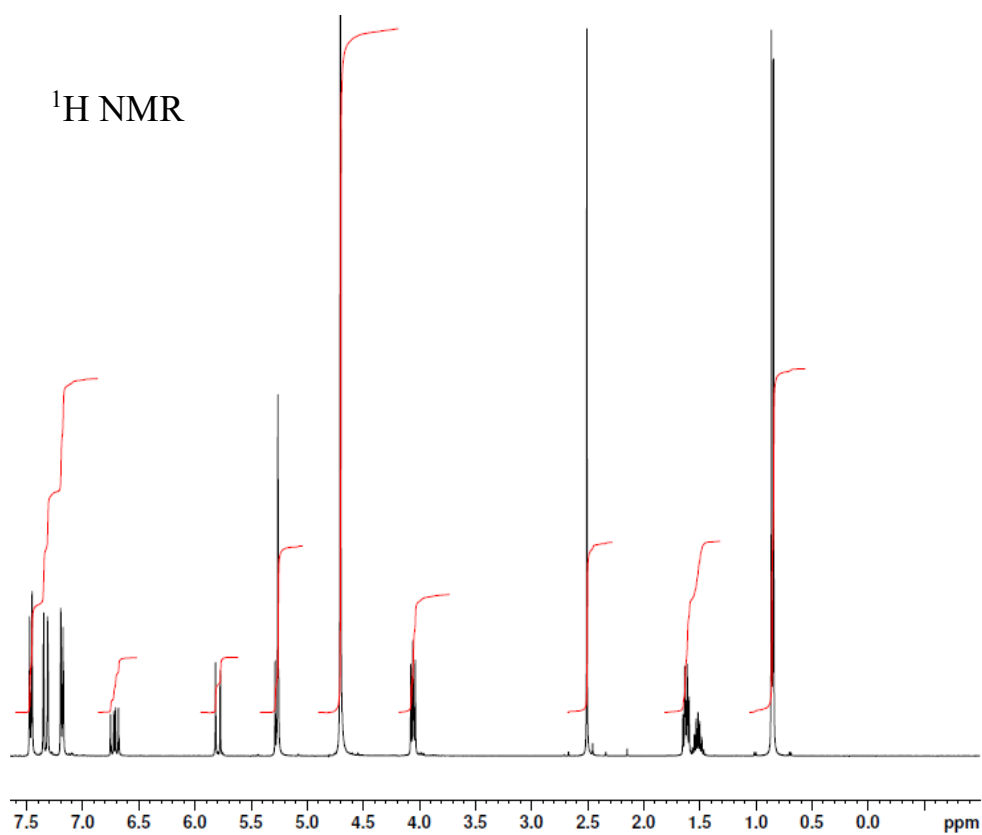


Figure 4.11 ^1H NMR (400 MHz) of 2-methyl-3,3,3-trimethylbutylimidazole in acetone- d_6 .

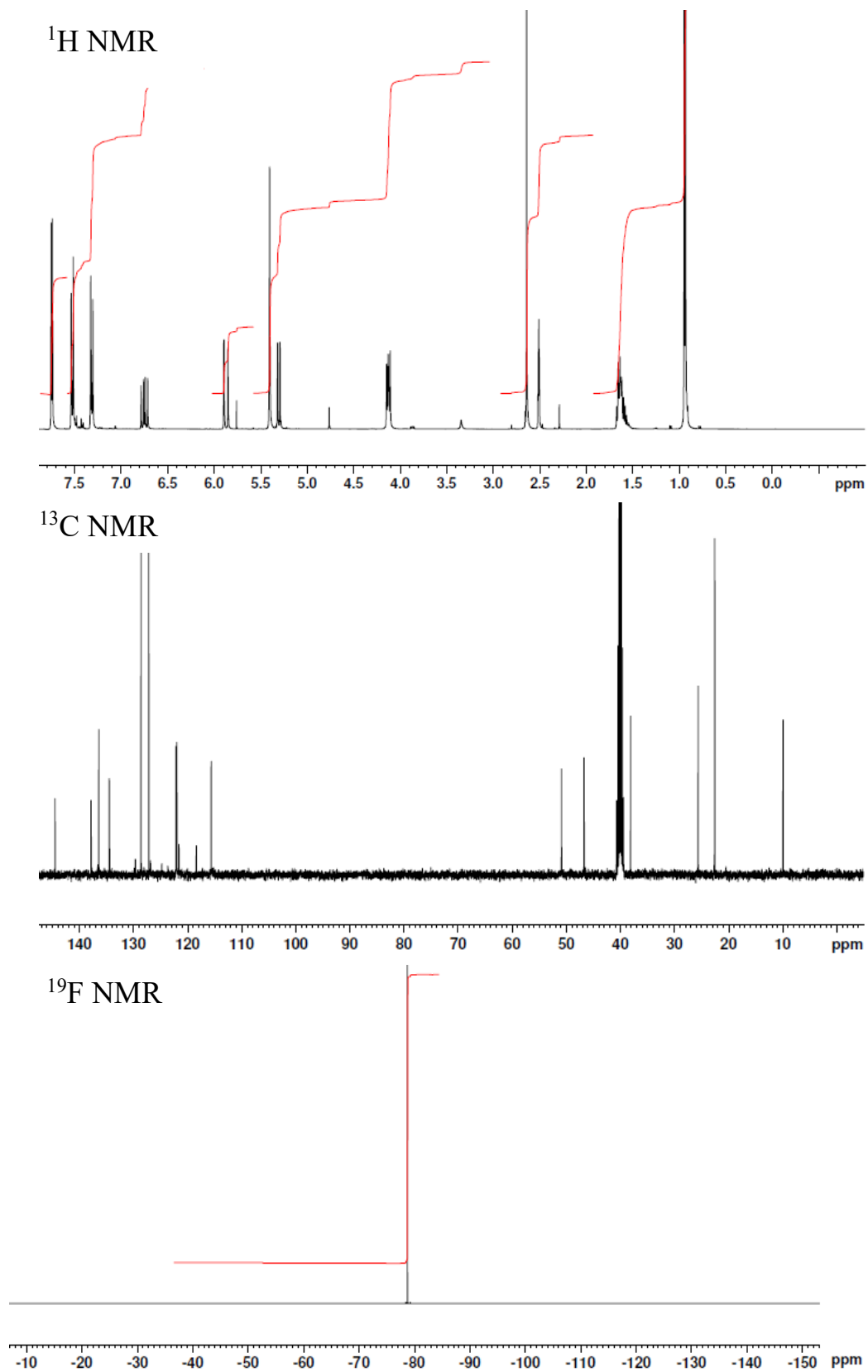


Figure 4.12 ^1H , ^{13}C and ^{19}F NMR spectra of (iPr)C2vbmim_TFSI in DMSO- d_6 .

The presence of the vinyl-benzene group brought a perturbation on the spectrum for what regards the peaks related the protons in the alkyl chain as well as the methyl group and the C-H groups on the imidazole ring. In particular, the peak corresponding to the two methyl groups on the alkyl chain lies now at 0.85 ppm, while the peak of the C-H shifted to 1.51 ppm. The peak of the other CH₂ group shifted to 4.05 ppm, the one corresponding to the methyl group on the imidazole is visible at 2.5 ppm, while the protons of the C-H on the imidazole ring are located at 7.31 ppm and 7.35 ppm. The new peaks brought by the vinyl-benzene group lye, from right to left, at 5.26 ppm for the CH₂ close to the nitrogen atom (N⁺) and at 5.28 ppm and 5.79 ppm for the two protons of the CH₂ of the vinyl group. While, at 6.71 ppm the quadruplet related to C-H of the vinyl group is visible and the multiplets at 7.19 ppm and 7.46 ppm correspond to the C-H of the benzene ring. The final ionic liquid synthesized was (iPr)C2vbmim_TFSI by ion exchange of (iPr)C2vbmim_Cl. Figure 4.12 shows the ¹H, ¹³C and ¹⁹F NMR spectra of (iPr)C2vbmim_TFSI. ¹H NMR displays the same peaks as for the (iPr)C2vbmim_Cl IL, ¹³C NMR shows the carbon atoms present in the molecule,

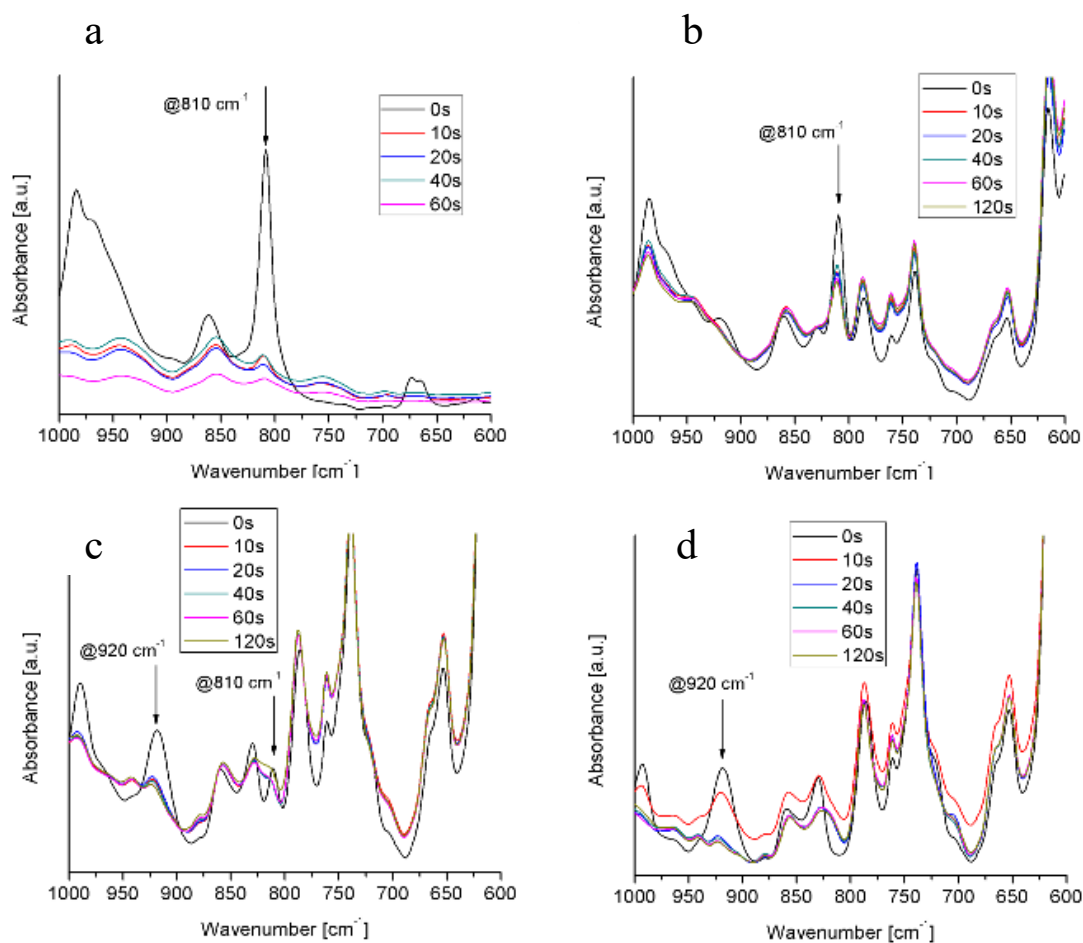


Figure 4.13 FTIR-ATR analysis of (iPr)C2vbmim_TFSI in different IL/PEGDA ratios: (a) 0/100 mol%, (b) 40/60 mol%, (c) 80/20 mol% and (d) 100/0 mol% on UV irradiation times from 0s to 120s.

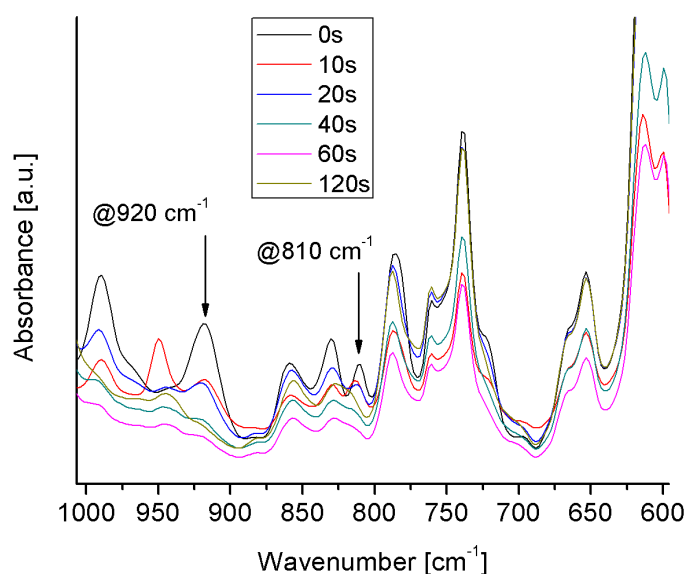
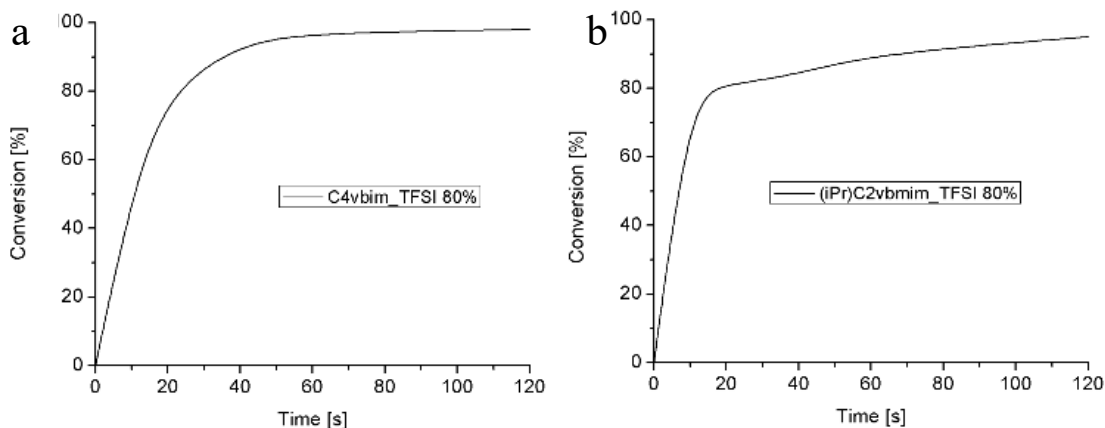


Figure 4.14 FTIR-ATR analysis of C4vbmim_TFSI with IL/PEGDA ratios: 80/20 mol% on UV irradiation times from 0s to 120s.

while ^{19}F senses the fluorine atoms present in the TFSI anion, with the characteristic peak centered at -79 ppm.

Once the ionic liquids were characterized by means of NMR, they were used to prepare the formulations described in section 4.2.3.

A study on the polymerization behavior and reaction kinetic was conducted on the prepared formulations containing both C4vbmim_TFSI and (iPr)C2vbmim_TFSI ILs. Firstly, formulations containing an IL/PEGDA ratio equivalent to 0/100, 40/60, 80/20 and 100/0 mol% were prepared and analyzed by means of FTIR as described in section 4.2.4. Figure 4.13 shows the FTIR-ATR spectra of formulations containing (iPr)C2vbmim_TFSI ionic liquid in different concentrations and different times of irradiation, from 0 to 120 seconds. The region of interest of the IR spectrum is between 1000 cm^{-1} and 600 cm^{-1} , in particular the peak centered at 810 cm^{-1} , where is located the vibrating frequency of the C=C carbon double bond of the acrylic group of PEGDA and the peak at 920 cm^{-1} which is characteristic of the C=C double bond of the vinyl group attached to the benzene ring of the ionic liquid were investigated.



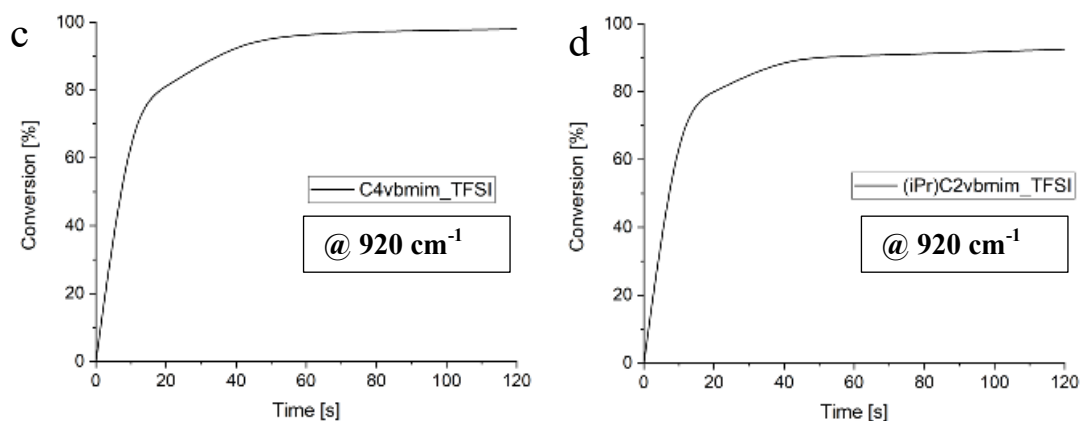


Figure 4.15 C=C double bond conversion, for polymerized samples with concentration 80/20 mol% IL/PEGDA followed at (a) 810 cm^{-1} for C4vbmim_TFSI, at (b) 810 cm^{-1} for (iPr)C2vbmim_TFSI at (c) 920 cm^{-1} for C4vbmim_TFSI and at (d) 920 cm^{-1} for (iPr)C2vbmim_TFSI.

From the results, it is possible to clearly see the progressive decrease of the peak at 810 cm^{-1} after UV-light exposure. In fact, as the exposure time increases, more conversion of the double bond is expected. In the case of 100% PEGDA, the formulation is almost totally cured after only 10 seconds and the conversion of the double bond is quicker due to the faster reaction of the bi-functional group with respect the other sample containing the IL. For the sample containing 80% and 100% of IL, the peak at 920 cm^{-1} is more evident and it was followed to study the conversion of the vinyl group of the polymerized ionic liquid. The samples with IL/PEGDA ratio equivalent to 80/20 mol% showed a good kinetic with a high conversion and polymerization rate for both the acrylic and vinyl groups, indicating the copolymerization of PEGDA with the ionic liquids (see Figure 4.15). For this reason, it was chosen as ILs concentration for other analysis. In figure 4.14, the FTIR-ATR reaction kinetic of C4vbmim_TFSI with concentration 80/20 mol% is shown. For a complete vision of the IR peaks of the kinetics of all the samples, the spectra from 4000 cm^{-1} to 600 cm^{-1} are shown in Figure E1 in Appendix E. The formulations containing 80/20 mol% IL/PEGDA were then analyzed by means of photo-rheology to further investigate their photo-curing ability, by directly correlating in real time reactive group conversion and irradiation time. Figure 4.16 depicts the photo-rheology curves of the formulations containing the two neat ionic liquids. The curves show the variation of the storage modulus during light irradiation as the formulation starts to polymerize. The lamp was turned on after 60 seconds from the beginning of the measurement to stabilize the system and, after nearly five seconds, the curve started to raise due to the crosslinking reaction. An initial fast growth of the storage modulus is noticeable in the first part after 30 seconds, then the rate of polymerization starts to decrease in the final stage of the measurement.

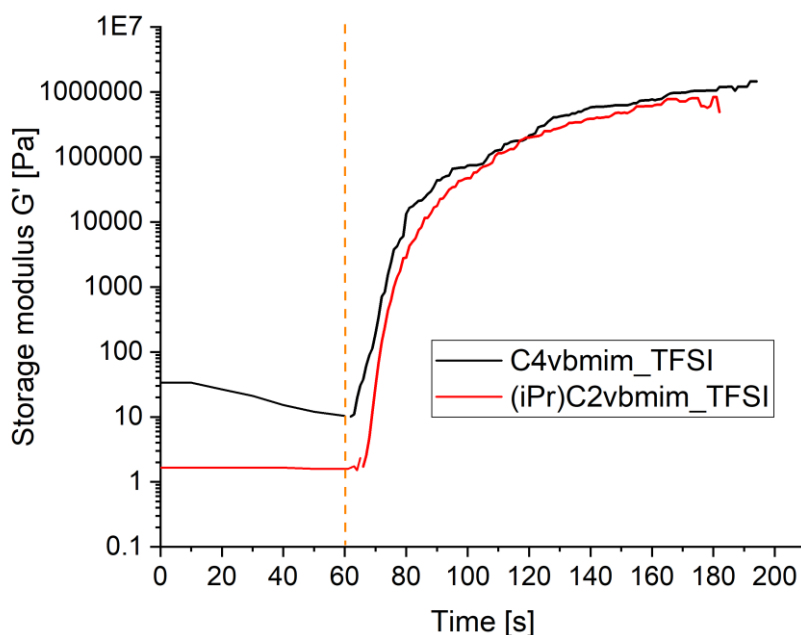


Figure 4.16 Photo-rheology analysis (smoothed curves) of C4vbmim_TFSI and (iPr)C2vbmim_TFSI. Light is tuned on after 1 minute (dotted line).

1.3.1 Matrix porosity modifications

1.3.1.1 Long chain poly ionic liquid (PDADMA_TFSI)

The next study was carried out to try to introduce an increase of gas mobility in the polymer matrix. The free volume inside the polymeric network was increased by dispersing a not-crosslinked long chain PIL. Poly(diallyldimethylammonium) bis(trifluoromethanesulfonyl)imide (PDADMA_TFSI) was chosen as the long chain PIL to be inserted in the formulations unlinked to the IL/PEGDA matrix. Formulations containing different concentrations of PDADMA_TFSI (0 %wt, 6 %wt and 20 %wt) were prepared and analyzed. The formulations appeared very turbid as the PIL concentration increased, because of the immiscibility of the two phases (PDADMA_TFSI and IL/PEGDA) and the creation of an emulsion. Thus, the liquid formulations were analyzed by means of UV-visible spectroscopy to estimate their turbidity caused by the formation of the phase separation. In fact, this aspect become relevant when 3D printing is involved, since the light scattering is an important parameter to take into account in terms of polymerization capacity and printing resolution. Figure 4.17 shows the light absorbance of the formulations, containing both of C4vbmim_TFSI and (iPr)C2vbmim_TFSI, calculated for the same thickness for all samples at the same wavelength. Results show that, as expected, by increasing the PDADMA_TFSI concentration in the formulations, the turbidity increases hindering the light penetration.

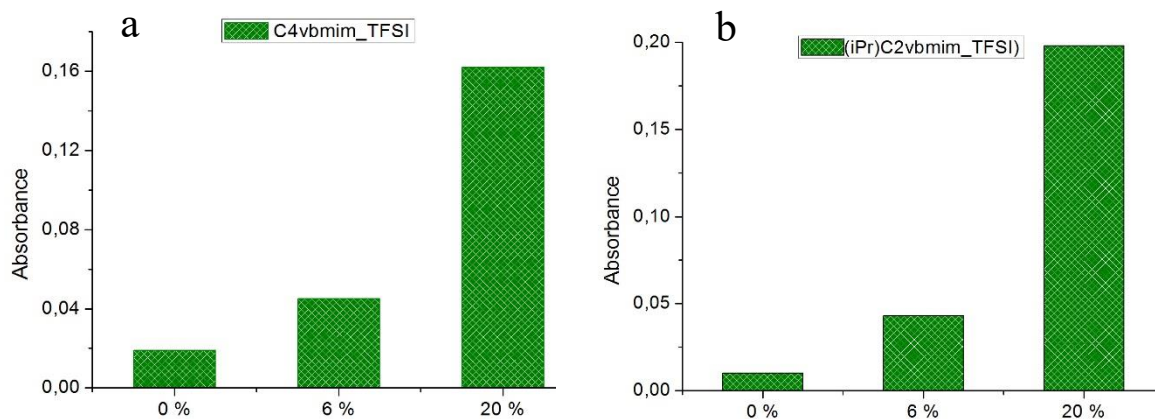


Figure 4.17 light absorbance of formulations containing (a) C4vbmim_TFSI and (b) (iPr)C2vbmim_TFSI at 0, 6 and 20 %wt of PDADMA.

Once the light absorption of the formulations was assessed, membranes with thickness of 150 μm were prepared as described in section 1.2.3 and tested for what regards their permeability behavior to CO_2 . Permeability measurements were performed on the membranes containing both the synthesized ILs and different concentrations of PDADME_TFSI (0, 6, 20 %wt). The analysis was carried out

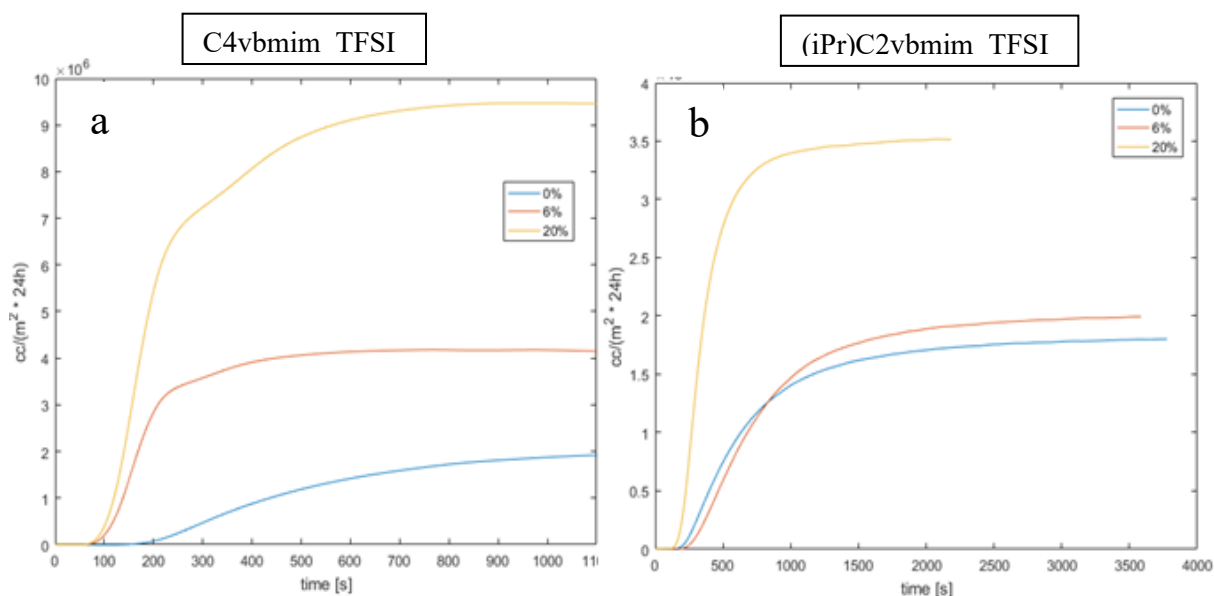


Figure 4.18 CO_2 transmission rate curves of membranes containing (a) C4vbmim_TFSI and (b) (iPr)C2vbmim_TFSI and 0 %wt, 6 %wt and 20 %wt of PDADMA_TFSI.

with the aim of finding out a correlation between the increase of gas transport properties in the membranes and their gas transmission rate through a fixed thickness. Figure 4.18 displays the CO_2 transmission rate curves of the membranes containing 0 %wt, 6 %wt and 20 %wt of PDADMA_TFSI versus time, at 25°C and 0% relative humidity. Results show an increase of CO_2 transmission rate, proportional to the permeability, with the increase of PIL concentration. This effect

can be explained as a consequence of an increase of the PIL/PEGDA chain mobility due to the presence of PDADMA_TFSI embedded in the matrix that enhance the CO₂ transport properties (260).

1.3.1.2 Ionic complexation by multivalent benzoic acid

The second way to introduce a macroporosity in the IL/PEGDA polymerized formulations was to use pyromellitic acid (PMA) to create an electrostatic complexation with the imidazolium-based ILs. In fact, PMA possesses a central benzene ring with 4 carboxylic groups (-COOH) that, upon neutralization in a basic solution (NaOH), creates an induced gradient pore structure and an in situ electrostatic cross-linking, with creation of voids (see Figure 4.19). The pore formation process would be triggered by the deswelling of the hydrophobic IL in contact with water as it penetrates the matrix. Simultaneously, the neutralization of the acid (PMA) by the base (NaOH) induces a complexation between the positively charged polymer cation and the negatively charged isophthalate, generating a crosslinked network locking the pores (259).

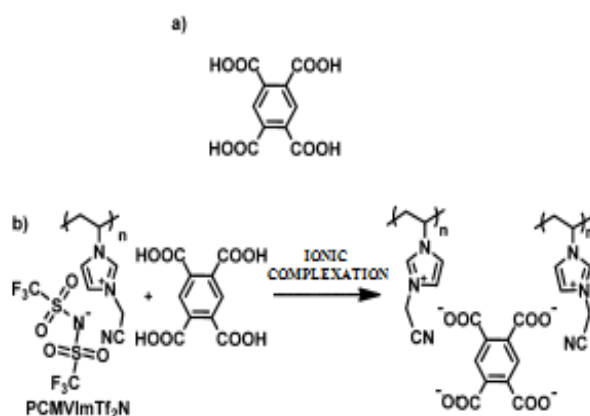


Figure 4.19 Schematic explanation of the electrostatic complexation process. (a) Chemical structure of PMA; (b) complexation process with neutralized PMA and a PIL (257).

From this assumption, samples containing 25 %wt of PMA were prepared as described in section 1.2.4 and DSC and TGA analysis were performed to know the stability of the samples at high temperatures and investigate the thermal properties of the material. Figure 4.20 and 4.21 display respectively the TGA and DSC analysis of C4vbmim_TFSI and (iPr)C2vbmim_TFSI containing membranes with and without PMA. Results show the loss of weight during the heating cycles from 25°C up to 800°C at 30°C/min. in the case of neat PIL/PEGDA, the samples show high thermal stability up to 350°C where they start to degrade in two steps, with onset at 400°C and 530°C. Whereas, for the samples with 25%wt of PMA, two weight losses are detected starting at T1 = 75°C and T2 = 220°C, attributed to the water evaporation present in the membrane (T1) and a second water evaporation at higher temperature (T2) probably bonded to PMA, due to its high hygroscopic nature. For what regards the DSC analysis, Figure 4.21 shows the curves in the temperature range from -20°C and 200°C with an increase of 10°C/min. Results show that the samples containing only the PILs display a Tg around 17°C that is lower than the Tg of neat PEGDA that is around 27°C (261). This can be explained by the fact that the ILs induce an increase of the chain mobility.

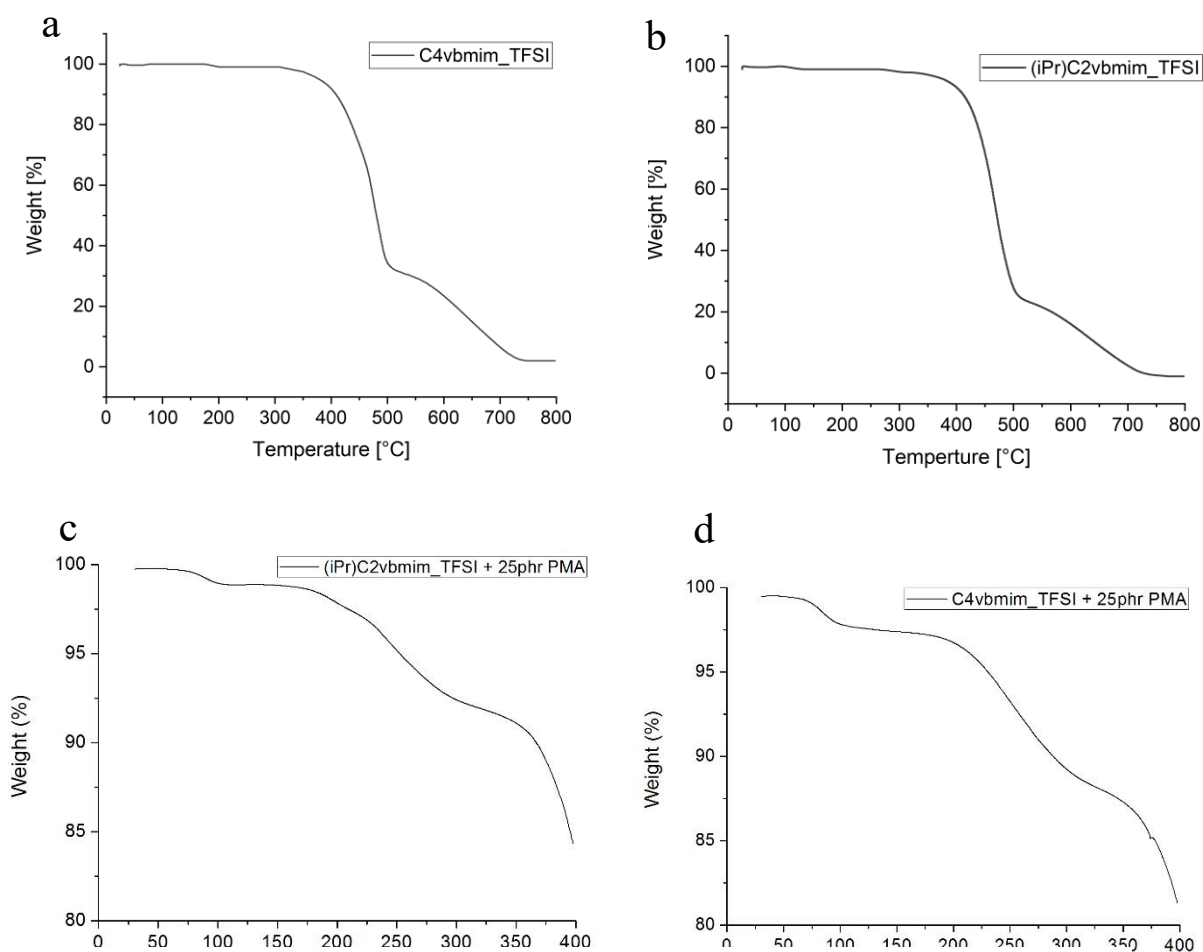


Figure 4.20 TGA curves from 25°C to 800°C of membranes containing (a) C4vbmim_TFSI, (b) and from 25°C to 400°C of membranes containing C4vbmim_TFSI + 25 %wt PMA and (c) (iPr)C2vbmim_TFSI + 25 %wt PMA.

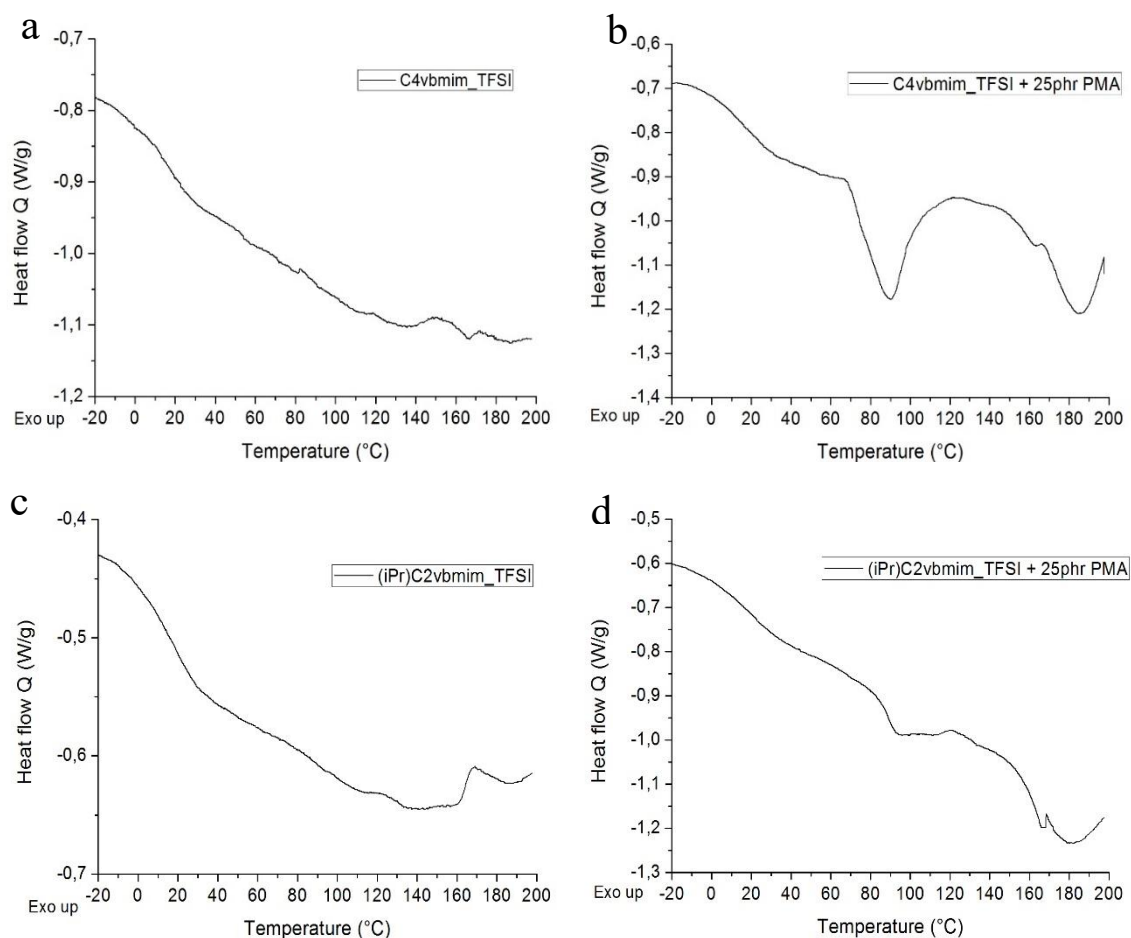


Figure 4.21 DSC curves from -30°C to 200°C of membranes containing (a) C4vbmim_TFSI, (b) C4vbmim_TFSI + 25%wt PMA, (c) (iPr)C2vbmim_TFSI and (d) (iPr)C2vbmim_TFSI + 25%wt PMA.

For what regards the samples containing 25%wt of PMA, two endothermic reactions at $T_1 = 90^{\circ}\text{C}$ and $T_2 = 180^{\circ}\text{C}$ are visible from the curves. These two-phase transitions are ascribable to the weight losses found in the TGA analysis. Analysis of the gas transport properties on the polymerized membranes containing PIL/PEGDA and PMA were performed through both N_2 absorption isotherms and CO_2 permeability analysis. Figure F1 in Appendix F shows the nitrogen absorption isotherms of membranes containing C4vbmim_TFSI + 0%wt, 6%wt and 25%wt of PMA. Whereas, Figure G1 in Appendix G displays the CO_2 transmission rate curves for membranes containing (iPr)C2vbmim_TFSI and C4vbmim_TFSI + 6%wt of PMA. Results from both analyses are not successful, since with increasing concentration of PMA in the samples lower N_2 absorption and CO_2 permeability was recorded. Thus, no evidence of a macro porosity in the polymer matrix was created.

1.3.2 3D printing and CO₂ uptake

Finally, the formulations were 3D printed as described in section 4.2.3. A simple geometry (see Figure 4.22a) was created with the help of a CAD software and printed with a DLP apparatus. The printing parameters were found by performing multiple tests on the formulation and, differently from the formulation

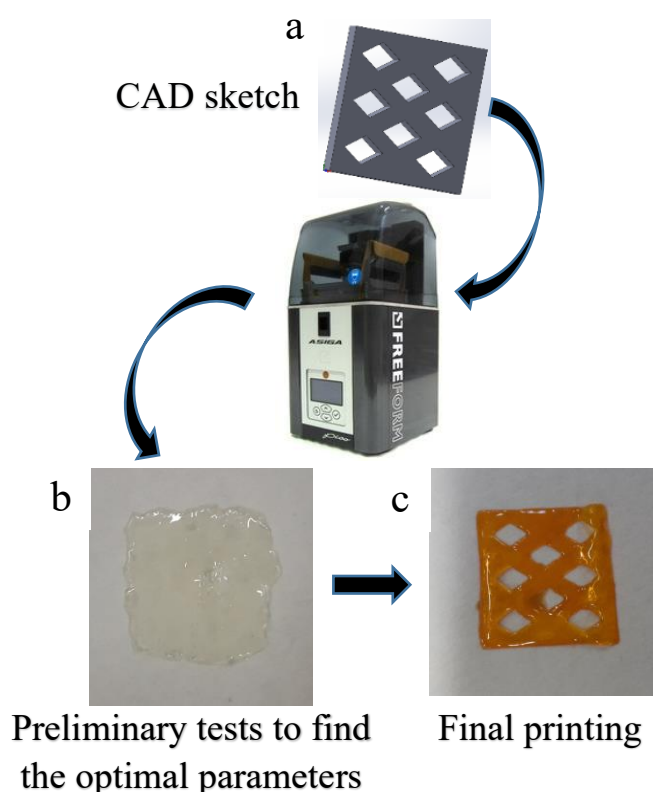


Figure 4.22 3D printing process flow depicting the (a) CAD sketch and the printed samples (b) before and (c) after resin and parameters optimization.

used to create the membranes, a dye was added to the resin to increase precision and printing resolution during the 3D printing process. 3D printing parameters were then adjusted in order to have the best printing performance, which includes perfect adherence of the object to the building platform, good printing times and good resolution along X-Y direction as well as along Z direction. The first problems emerged in the first steps of the printing as the structure had issues to stick to the platform. The burn-in time was adjusted in such a way that it was not too high, preventing over-polymerization of the resin and introducing a big time difference between the burn-in and normal times, but not too low to allow the structure to remain attached to the platform. The optimal burn-in time was set to 6 seconds for four layers (200 μm). The normal time, instead, is usually lower than the burning time because the remaining layers require less time to cure and to stick to the previous ones, even if, it should not be too low to allow a good polymerization and

printing resolution. The normal time was set to 1.5 seconds. The final object (see figure 4.22c) was then washed and post-cured.

The 3D printed samples containing both (iPr)C2vbmim_TFSI and C4vbmim_TFSI ILs were finally tested in the CO₂ uptake apparatus. Measurements were carried out at high pressure from 0 to 40 bar at 25°C and weight variation was recorded. Figure 4.23 reports the CO₂ uptake analysis for samples containing the two PILs compared with the IL counterpart 1-butyl-3-methylimidazolium bis(trifluoromethylsulfonyl)imide (bmim [TFSI]) tested from Aki et al. (155). Results show a good positive adsorption of the samples with a slightly better uptake from the linear alkyl chain PIL. This is a proof that the different conformation of the alkyl chain does not influence too much the gas uptake capacity. Nevertheless, both PILs demonstrated a high CO₂ adsorption capacity, with an uptake of 8.76 mg(CO₂)/g(PIL) at 1 bar, that is a promising result for this kind of materials.

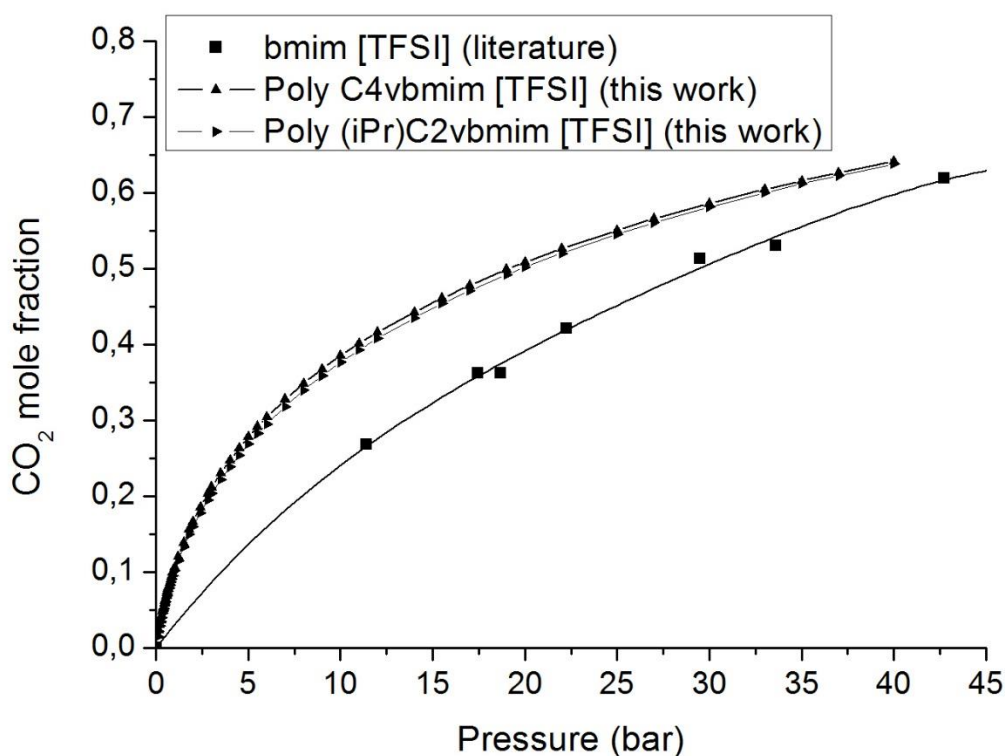


Figure 4.23 High pressure CO₂ uptake analysis for polymerized samples containing (iPr)C2vbmim_TFSI and C4vbmim_TFSI PILs compared to liquid counterpart 1-butyl-3-methylimidazolium bis(trifluoromethylsulfonyl)imide (bmim [TFSI]) (155), with applied pressure from 0 to 40 bar at 25°C. The data of bmim [TFSI] were fitted with a polynomial function of the fourth order.

1.4 Conclusion

The aim of the study was to create an ionic liquid with the specific characteristic to make it CO₂-philic and photo-curable and, in particular able to be 3D printable with DLP technique. This was done by successfully synthesizing two imidazole-based ionic liquids bearing two different alkyl chain, one linear and one branched, and a reactive vinyl group. Moreover, a fluorinated anion (TFSI) was chosen as counter ion for its high CO₂ uptake capacity. The ionic liquids were characterized by means of NMR to confirm the correct synthesis and a polymerization study was conducted to estimate their ability to photo-polymerize and the possibility to use them as additive or constitutive monomer for a 3D printable resin. FTIR-ATR and photo-rheology on mixtures with PEGDA confirmed their ability to be photo-cured by showing good reactivity and fast reactive group conversion up to IL/PEGDA (Mn 250) ratio of 80/20 mol%.

Afterwards, the possibility to introducing a macro porosity in the polymer matrix was studied following two paths. The first, by addition of a long chain PIL (PDADMA_TFSI) to increase the free volume in the polymer network, while in the second, the creations of macro pores was stabilized by ionic cross-linking by neutralization of multi-acid bearing –COOH groups, using PMA. In the first case, PDADMA_TFSI brought a considerable turbidity of the formulations, confirmed also by UV-visible analysis, which could become an issue for an application in DLP 3D printing. Nevertheless, permeability analysis of membranes containing PDADMA_TFSI with concentrations up to 20%wt gave results in according with the theory by displaying a higher permeability in the membranes with higher concentration of PDADMA_TFSI. In the second case, instead, the addition of PMA as ionic complexing agent did not reach the expected results, confirmed by unsuccessful nitrogen isotherms and permeability analysis. In contrast, the formulations containing mixture of both ILs and PEGDA were successfully 3D printed in a DLP 3D printer, and simple lattice geometries were created.

The 3D printed structures were tested to measure their CO₂ uptake capacity in a high-pressure CO₂ apparatus. PIL (iPr)C2vbmim_TFSI interestingly showed lower CO₂ adsorption capacity than the linear alkyl chain PIL C4vbmim_TFSI. This result seems to be in contrast with what found in literature about the higher CO₂ adsorption capacity in cations bearing longer alkyl chains. Nevertheless, two possible explanations to this behaviour can be done. First, the results in literature are associated to CO₂ solubility tests carried out on RTIL, where the ionic species are free to move in the liquid material, while in PILs the ions are linked to the polymer network, modifying the physical properties of the materials and the interaction mechanism with CO₂. Secondly, there is the possibility that the branched alkyl chain used to synthesize (iPr)C2vbmim_TFSI was not longer enough to introduce a significant variation in the CO₂ capture capacity.

The overall CO₂ adsorption was still high and a comparison with the IL counterpart bmim[TFSI] showed the predominance of the prepared PILs. This result is consistent with previously published studies on poly ionic liquids employed

for CO₂ capture technology (143, 168, 262, 263) and confirm the appealing properties of this kind of materials to be used as sorbents for gas storage.

1.5 Next steps

Further studies will be carried out on this work to complete the experimental part and deeply understand the unexplained results found so far. In particular, the next goals that will be achieved are described below.

- A solid state high pressure NMR analysis would be necessary to understand the interaction mechanisms between CO₂ and the polyions in the polymer network.
- Increasing the number of synthesized PILs with different anions and cations would lead to a better understanding on how the CO₂ solubility varies in a polymer matrix where the polyions are interchanged.
- The successful 3D printing of more complex geometries, which is a time-consuming task due to the long ILs synthesis processes and the small amount of compound that is obtained.
- Further analysis, such as viscosity measurements and TGA/IR.

Ionic liquids' nomenclature

C4vbmim_Cl: 1-(4-vinylbenzyl)-2-methyl-3-butylimidazolium chloride

(iPr)C2vbmi_Cl: 1-(4-vinylbenzyl)-2-methyl-3-3,3-Dimethylbutylimidazolium chloride

C4vbmim_TFSI: 1-(4-vinylbenzyl)-2-methyl-3-butylimidazolium bis(trifluoromethanesulfonyl)imide

C4vbmim_Ac: 1-(4-vinylbenzyl)-2-methyl-3-butylimidazolium acetate

(iPr)C2vbimim_TFSI: 1-(4-vinylbenzyl)-2-methyl-3-3,3-Dimethylbutylimidazolium bis(trifluoromethanesulfonyl)imide

(iPr)C2vbimim_Ac: 1-(4-vinylbenzyl)-2-methyl-3-3,3-Dimethylbutylimidazolium Acetate

Conclusion

The work described in this thesis was carried out to investigate the possibility to create, through DLP 3D printing technology, materials with specific characteristic compatible with CO₂ separation and capture technology. To achieve this goal, the materials need to fulfil certain requirements. First of all the prepared material must be in liquid form to be processed in a DLP apparatus, secondly it needs to be photo-reactive, i.e. it must possess one or more chemical groups that, under certain condition of light, are able to create a crosslinked network and a final solid structure. At the same time, the material must be able to interact with CO₂ either by having a higher permeability with respect to other gases (i.e. high permselectivity), or by possessing a high solubility (i.e. high CO₂ capture capacity).

The first study was centered on the investigation of the CO₂ transport properties (i.e. permeability, diffusivity and solubility) of membranes containing azobenzene moieties (dyes) able to be photocontrolled from an external light source. The possibility to control the gas permeability of a polymer membrane was a key aspect for an application in CO₂ separation technology. Moreover, the capacity to carry out this process without stressing the system (the light source does not touch the membrane) was an important feature. The membranes, composed of crosslinked PEGDA and the azo dyes, showed a remarkable CO₂ permeability change under light irradiation. In particular, the permeability of the membranes increased of 70% when irradiated with the laser source at a characteristic wavelength (532 nm) close to the absorption band of the azo dye. This effect was explained by the cyclic isomerization of the azobenzene molecules inside the polymer matrix, brought by light absorption, leading to an increase of the inner free volume. In this context, 3D printing was exploited by creating an original device able to use this effect to control the CO₂ concentration in a mixture of gases. The prototype was successfully 3D printed in one single shot using two functional formulations, one containing a laser-transparent dye and the other with the photo-functional azo dye. The device was then connected to a water solution, and a significant pH change, due to increasing CO₂ concentration after light irradiation, was recorded. Furthermore, the azo membranes were also tested with oxygen, showing a high permselectivity PCO₂/PO₂ of about 30. This last result was also appealing for a possible application of this material in membrane technology for CO₂ separation.

The second study was focused on the use of ionic liquids in 3D printable formulations for applications in CO₂ capture and separation. The polymerization characteristics of formulations containing PEGDA and different kinds of ILs were investigated showing different behaviors, depending on the nature of cations,

anions and on the presence of functional groups. Formulations with ILs containing a vinyl and a methacrylate group showed faster reaction kinetic compared to other samples with ILs dispersed in the matrix, even if they were good as well. Furthermore, it was found that the ionic liquid with ammonium as cation ($C_4N_{MA,11}$ [Tf₂N]) showed slow polymerization kinetic and was difficult to print, due to polymerization inhibition caused by ammonium species. The mechanical properties evaluated on the polymerized samples confirmed the results found with the polymerization kinetic study and the formulations were successfully 3D printed to create complex cubic hollow structures. The 3D printed structures were finally tested to investigate their CO₂ absorption ability. FTIR analysis showed the presence of peaks related to CO₂ centered at 2340 cm⁻¹ and 2360 cm⁻¹ after exposure. Nevertheless, weight analysis of CO₂ absorption at pressures up to 3 bar showed unsatisfying uptake results for all the tested ionic liquids. These results need to be considered related to the measuring apparatus used to perform this kind of tests. In fact, the samples needed to be moved from the CO₂ chamber to an external scale, introducing impurities and a series of systematic errors impossible to predict. Thus, an improved measuring system needs to be set up in future studies to better understand the CO₂ absorption capacity of these materials.

The last part of the thesis work was centered upon the synthesis of specific imidazolium-based ionic liquids bearing a reactive vinyl group and two different alkyl chains at the cation and two different anions (TFSI and acetate). The NMR results confirmed the correct synthesis of the ILs, except for the one with the acetate as anion, which caused problems during the ion exchange process. Moreover, the photopolymerization study of the ionic liquids mixed with an acrylate monomer (PEGDA) demonstrated a good reactivity with double bond conversion up to 97% after 2 minutes of light exposure, for concentration of ILs up to 80 mol%. For an application in CO₂ capture technology, the increase of gas interaction with the polymer matrix was a key aspect. In this regard, two ways were undertaken to increasing gas transport properties within the polymer network: the use of a long chain PIL (PDADMA[TFSI]) and the creation of a macroporosity triggered by ionic complexation of neutralized pyromellitic acid (PMA). The first one seemed to be the most suitable, since CO₂ permeability analysis on membrane containing different concentration of PDADMA[TFSI] up to 20 %wt, showed an increased permeability. Nevertheless, the PIL was not soluble in PEGDA neither in the synthesized ILs and formed an emulsion due to phase separation in the formulation by increasing its turbidity, confirmed by UV-visible analysis. This effect, in fact, should be taken under consideration as it might affect the polymerization capacity. For what regards the macroporosity introduction by PMA neutralization, following the method used by Täuber et al. (259), results from the nitrogen isotherms and CO₂ permeability analysis showed that no porosity was created within the polymer matrix. 3D printing tests were then performed on formulations containing the synthesized ionic liquids and simple geometries were successfully 3D printed. Finally, the CO₂ absorption analysis (up to 40 bar), performed in a high pressure chamber equipped with a microbalance, showed high uptake capacity for both PILs

with no remarkable difference between linear and branched alkyl chains. Furthermore, the adsorption analyses were compared with the uptake capacity of the analogous RTIL found in literature confirming the high potential of this PILs for applications in CO₂ capture technology.

References

1. Wu J. Landscape sustainability science: ecosystem services and human well-being in changing landscapes. *Landscape ecology*. 2013;28(6):999-1023.
2. Steffen W, Persson Å, Deutsch L, Zalasiewicz J, Williams M, Richardson K, et al. The Anthropocene: From global change to planetary stewardship. *Ambio*. 2011;40(7):739.
3. Hulme M. On the origin of the greenhouse effect: John Tyndall's 1859 interrogation on nature. *Weather*. 2009;64(5):121-3.
4. Human RNE, Jun TX. Energy related CO₂ emissions and the progress on CCS projects: a review. *Renewable and Sustainable Energy Reviews*. 2014;31:368-85.
5. Olivier JG, Peters JA, Janssens-Maenhout G. Trends in global CO₂ emissions 2012 report. 2012.
6. Agency IE. CO₂ Emissions from Fuel Combustion (2012 edition). 2012.
7. Nejat P, Jomehzadeh F, Taheri MM, Gohari M, Majid MZA. A global review of energy consumption, CO₂ emissions and policy in the residential sector (with an overview of the top ten CO₂ emitting countries). *Renewable and sustainable energy reviews*. 2015;43:843-62.
8. Suarez-Gutierrez L, Li C, Müller WA, Marotzke J. Internal variability in European summer temperatures at 1.5 C and 2 C of global warming. *Environmental Research Letters*. 2018;13(6):064026.
9. Coley D, Kershaw T, Eames M. A comparison of structural and behavioural adaptations to future proofing buildings against higher temperatures. *Building and Environment*. 2012;55:159-66.
10. Field CB. *Climate change 2014—Impacts, adaptation and vulnerability: Regional aspects*: Cambridge University Press; 2014.
11. Hansen J, Sato M, Ruedy R, Kharecha P, Lacis A, Miller R, et al. Dangerous human-made interference with climate: a GISS modelE study. *Atmospheric chemistry and physics*. 2007;7(9):2287-312.
12. Houghton JT, Ding Y, Griggs DJ, Noguer M, van der Linden PJ, Dai X, et al. *Climate change 2001: the scientific basis*: The Press Syndicate of the University of Cambridge; 2001.
13. Hansen J, Sato M. Greenhouse gas growth rates. *Proceedings of the National Academy of Sciences*. 2004;101(46):16109-14.
14. Bains P, Psarras P, Wilcox J. CO₂ capture from the industry sector. *Progress in Energy and Combustion Science*. 2017;63:146-72.
15. Edenhofer O. *Climate change 2014: mitigation of climate change*: Cambridge University Press; 2015.

16. IEA. Technology Roadmap Carbon Capture and Storage—2013 Edition. Organization for Economic Co-operation and Development/International Energy ...; 2013.
17. Machida H, Ando R, Esaki T, Yamaguchi T, Norinaga K. Modelling of CO₂ solubility in phase separation solvent composed of amine/ether/water system for CO₂ capture. *Journal of Molecular Liquids*. 2019;292:111411.
18. Kussainova D, Shah D. Monoethanolamine based DESs for CO₂ absorption: Insights from molecular dynamics simulations. *Separation and Purification Technology*. 2020;231:115931.
19. Yang H, Xu Z, Fan M, Gupta R, Slimane RB, Bland AE, et al. Progress in carbon dioxide separation and capture: A review. *Journal of environmental sciences*. 2008;20(1):14-27.
20. Olajire AA. CO₂ capture and separation technologies for end-of-pipe applications—a review. *Energy*. 2010;35(6):2610-28.
21. Pires J, Martins F, Alvim-Ferraz M, Simões M. Recent developments on carbon capture and storage: an overview. *Chemical engineering research and design*. 2011;89(9):1446-60.
22. Heo Y-J, Seong DB, Park S-J. Synthesis of polyethylenimine-impregnated titanate nanotubes for CO₂ capture: Influence of porosity and nitrogen content on amine-modified adsorbents. *Journal of CO₂ Utilization*. 2019;34:472-8.
23. Zhao P, Zhang G, Xu Y, Lv Y. Amine functionalized hierarchical bimodal mesoporous silicas as a promising nanocomposite for highly efficient CO₂ capture. *Journal of CO₂ Utilization*. 2019;34:543-57.
24. Stefanelli E, Puccini M, Vitolo S, Seggiani M. CO₂ sorption kinetic study and modeling on doped-Li₄SiO₄ under different temperatures and CO₂ partial pressures. *Chemical Engineering Journal*. 2020;379:122307.
25. Yang Y, Liu W, Hu Y, Sun J, Tong X, Li Q, et al. Novel low cost Li₄SiO₄-based sorbent with naturally occurring wollastonite as Si-source for cyclic CO₂ capture. *Chemical Engineering Journal*. 2019;374:328-37.
26. Theo WL, Lim JS, Hashim H, Mustaffa AA, Ho WS. Review of pre-combustion capture and ionic liquid in carbon capture and storage. *Applied energy*. 2016;183:1633-63.
27. Halder K, Khan MM, Grünauer J, Shishatskiy S, Abetz C, Filiz V, et al. Blend membranes of ionic liquid and polymers of intrinsic microporosity with improved gas separation characteristics. *Journal of Membrane Science*. 2017;539:368-82.
28. Marsh K, Boxall J, Lichtenthaler R. Room temperature ionic liquids and their mixtures—a review. *Fluid phase equilibria*. 2004;219(1):93-8.
29. Zeng S, Zhang X, Bai L, Zhang X, Wang H, Wang J, et al. Ionic-liquid-based CO₂ capture systems: structure, interaction and process. *Chemical reviews*. 2017;117(14):9625-73.
30. Andirova D, Cogswell CF, Lei Y, Choi S. Effect of the structural constituents of metal organic frameworks on carbon dioxide capture. *Microporous and Mesoporous Materials*. 2016;219:276-305.
31. Nandasiri MI, Jambovane SR, McGrail BP, Schaeff HT, Nune SK. Adsorption, separation, and catalytic properties of densified metal-organic frameworks. *Coordination Chemistry Reviews*. 2016;311:38-52.
32. Venna SR, Carreon MA. Metal organic framework membranes for carbon dioxide separation. *Chemical Engineering Science*. 2015;124:3-19.

33. Li W, Zhang Y, Li Q, Zhang G. Metal– organic framework composite membranes: Synthesis and separation applications. *Chemical Engineering Science*. 2015;135:232-57.
34. Araújo OdQF, de Medeiros JL. Carbon capture and storage technologies: present scenario and drivers of innovation. *Current Opinion in Chemical Engineering*. 2017;17:22-34.
35. Jansen D, Gazzani M, Manzolini G, van Dijk E, Carbo M. Pre-combustion CO₂ capture. *International Journal of Greenhouse Gas Control*. 2015;40:167-87.
36. Hadjipaschalis I, Kourtis G, Poullikkas A. Assessment of oxyfuel power generation technologies. *Renewable and Sustainable Energy Reviews*. 2009;13(9):2637-44.
37. Wang Ca, Zhang X, Liu Y, Che D. Pyrolysis and combustion characteristics of coals in oxyfuel combustion. *Applied Energy*. 2012;97:264-73.
38. Rahman FA, Aziz MMA, Saidur R, Bakar WAWA, Hainin M, Putrajaya R, et al. Pollution to solution: Capture and sequestration of carbon dioxide (CO₂) and its utilization as a renewable energy source for a sustainable future. *Renewable and Sustainable Energy Reviews*. 2017;71:112-26.
39. Pennline HW, Luebke DR, Jones KL, Myers CR, Morsi BI, Heintz YJ, et al. Progress in carbon dioxide capture and separation research for gasification-based power generation point sources. *Fuel Processing Technology*. 2008;89(9):897-907.
40. Guerrero-Lemus R, Martínez-Duart JM. Renewable energy and CO₂: current status and costs. *Renewable Energies and CO₂*: Springer; 2013. p. 9-33.
41. Herzog H, Golomb D. Carbon capture and storage from fossil fuel use. *Encyclopedia of energy*. 2004;1(6562):277-87.
42. Chen Y, Mutelet F, Jaubert J-NI. Modeling the solubility of carbon dioxide in imidazolium-based ionic liquids with the PC-SAFT equation of state. *The Journal of Physical Chemistry B*. 2012;116(49):14375-88.
43. Aghaie M, Rezaei N, Zendehboudi S. A systematic review on CO₂ capture with ionic liquids: Current status and future prospects. *Renewable and Sustainable Energy Reviews*. 2018;96:502-25.
44. Chakma A. Formulated solvents: New opportunities for energy efficient separation of acid gases. *Energy Sources*. 1999;21(1-2):51-62.
45. Sreedhar I, Nahar T, Venugopal A, Srinivas B. Carbon capture by absorption–path covered and ahead. *Renewable and Sustainable Energy Reviews*. 2017;76:1080-107.
46. Martín MM. *Industrial chemical process analysis and design*: Elsevier; 2016.
47. Stewart M. *Surface Production Operations: Vol 2: Design of Gas-Handling Systems and Facilities*: Gulf Professional Publishing; 2014.
48. Miller B. 8-Greenhouse gas-carbon dioxide emissions reduction technologies. *Fossil fuel emissions control technologies*. 2015:367-438.
49. Rackley SA. *Carbon capture and storage*: Butterworth-Heinemann; 2017.
50. Speight JG. *Natural gas: a basic handbook*: Gulf Professional Publishing; 2018.
51. Sistla YS, Khanna A. CO₂ absorption studies in amino acid-anion based ionic liquids. *Chemical Engineering Journal*. 2015;273:268-76.
52. Thomas DC, Lazarova MB, Inkson K. Global careers: new phenomenon or new perspectives? *Journal of World Business*. 2005;40(4):340-7.

53. Dave N, Do T, Puxty G, Rowland R, Feron P, Attalla M. CO₂ capture by aqueous amines and aqueous ammonia—A Comparison. *Energy Procedia*. 2009;1(1):949-54.
54. Aroonwilas A, Tontiwachwuthikul P. High-efficiency structured packing for CO₂ separation using 2-amino-2-methyl-1-propanol (AMP). *Separation and purification technology*. 1997;12(1):67-79.
55. van der Zwaan B, Smekens K. CO₂ capture and storage with leakage in an energy-climate model. *Environmental Modeling & Assessment*. 2009;14(2):135-48.
56. Davidson RM. Post-combustion carbon capture from coal fired plants: solvent scrubbing: IEA Clean Coal Centre London; 2007.
57. Aroonwilas A, Veawab A. Characterization and comparison of the CO₂ absorption performance into single and blended alkanolamines in a packed column. *Industrial & engineering chemistry research*. 2004;43(9):2228-37.
58. Bishnoi S, Rochelle GT. Absorption of carbon dioxide into aqueous piperazine: reaction kinetics, mass transfer and solubility. *Chemical engineering science*. 2000;55(22):5531-43.
59. Barzagli F, Mani F, Peruzzini M. Continuous cycles of CO₂ absorption and amine regeneration with aqueous alkanolamines: a comparison of the efficiency between pure and blended DEA, MDEA and AMP solutions by ¹³C NMR spectroscopy. *Energy & Environmental Science*. 2010;3(6):772-9.
60. Xu G-W, Zhang C-F, Qin S-J, Gao W-H, Liu H-B. Gas– Liquid Equilibrium in a CO₂– MDEA– H₂O System and the Effect of Piperazine on It. *Industrial & engineering chemistry research*. 1998;37(4):1473-7.
61. Kim YE, Lim JA, Jeong SK, Yoon YI, Bae ST, Nam SC. Comparison of carbon dioxide absorption in aqueous MEA, DEA, TEA, and AMP solutions. *Bulletin of the Korean Chemical Society*. 2013;34(3):783-7.
62. Tontiwachwuthikul P, Meisen A, Lim CJ. CO₂ absorption by NaOH, monoethanolamine and 2-amino-2-methyl-1-propanol solutions in a packed column. *Chemical Engineering Science*. 1992;47(2):381-90.
63. Alper E. Reaction mechanism and kinetics of aqueous solutions of 2-amino-2-methyl-1-propanol and carbon dioxide. *Industrial & Engineering Chemistry Research*. 1990;29(8):1725-8.
64. Sreenivasulu B, Gayatri D, Sreedhar I, Raghavan K. A journey into the process and engineering aspects of carbon capture technologies. *Renewable and Sustainable Energy Reviews*. 2015;41:1324-50.
65. Mores P, Scenna N, Mussati S. A rate based model of a packed column for CO₂ absorption using aqueous monoethanolamine solution. *International Journal of Greenhouse Gas Control*. 2012;6:21-36.
66. Wappel D, Gronald G, Kalb R, Draxler J. Ionic liquids for post-combustion CO₂ absorption. *International Journal of Greenhouse Gas Control*. 2010;4(3):486-94.
67. Koronaki I, Prentza L, Papaefthimiou V. Modeling of CO₂ capture via chemical absorption processes— An extensive literature review. *Renewable and Sustainable Energy Reviews*. 2015;50:547-66.
68. Zhao B, Su Y, Tao W, Li L, Peng Y. Post-combustion CO₂ capture by aqueous ammonia: A state-of-the-art review. *International Journal of Greenhouse Gas Control*. 2012;9:355-71.

69. Cullinane JT, Rochelle GT. Thermodynamics of aqueous potassium carbonate, piperazine, and carbon dioxide. *Fluid Phase Equilibria*. 2005;227(2):197-213.
70. Guo D, Thee H, da Silva G, Chen J, Fei W, Kentish S, et al. Borate-catalyzed carbon dioxide hydration via the carbonic anhydrase mechanism. *Environmental science & technology*. 2011;45(11):4802-7.
71. Ahmadi M, Gomes V, Ngian K. Advanced modelling in performance optimization for reactive separation in industrial CO₂ removal. *Separation and Purification Technology*. 2008;63(1):107-15.
72. Endo K, Nguyen QS, Kentish SE, Stevens GW. The effect of boric acid on the vapour liquid equilibrium of aqueous potassium carbonate. *Fluid Phase Equilibria*. 2011;309(2):109-13.
73. Lu Y, Ye X, Zhang Z, Khodayari A, Djukadi T. Development of a carbonate absorption-based process for post-combustion CO₂ capture: the role of biocatalyst to promote CO₂ absorption rate. *Energy Procedia*. 2011;4:1286-93.
74. Russo M, Olivieri G, Marzocchella A, Salatino P, Caramuscio P, Cavaleiro C. Post-combustion carbon capture mediated by carbonic anhydrase. *Separation and Purification Technology*. 2013;107:331-9.
75. Pellegrini G, Strube R, Manfrida G. Comparative study of chemical absorbents in postcombustion CO₂ capture. *Energy*. 2010;35(2):851-7.
76. Puxty G, Rowland R, Attalla M. Comparison of the rate of CO₂ absorption into aqueous ammonia and monoethanolamine. *Chemical Engineering Science*. 2010;65(2):915-22.
77. Yeh AC, Bai H. Comparison of ammonia and monoethanolamine solvents to reduce CO₂ greenhouse gas emissions. *Science of the Total Environment*. 1999;228(2-3):121-33.
78. Meisen A, Shuai X. Research and development issues in CO₂ capture. *Energy Conversion and Management*. 1997;38:S37-S42.
79. Ho MT, Allinson GW, Wiley DE. Reducing the cost of CO₂ capture from flue gases using pressure swing adsorption. *Industrial & Engineering Chemistry Research*. 2008;47(14):4883-90.
80. Yang RT. *Gas separation by adsorption processes*: Butterworth-Heinemann; 2013.
81. Grande CA, Rodrigues AE. Electric swing adsorption for CO₂ removal from flue gases. *International Journal of Greenhouse Gas Control*. 2008;2(2):194-202.
82. Akten ED, Siriwardane R, Sholl DS. Monte Carlo simulation of single-and binary-component adsorption of CO₂, N₂, and H₂ in zeolite Na-4A. *Energy & Fuels*. 2003;17(4):977-83.
83. Batten SR, Robson R. Interpenetrating nets: ordered, periodic entanglement. *Angewandte Chemie International Edition*. 1998;37(11):1460-94.
84. Batten SR, Neville SM, Turner DR. *Coordination polymers: design, analysis and application*: Royal Society of Chemistry; 2008.
85. Tanaka D, Kitagawa S. Template effects in porous coordination polymers. *Chemistry of Materials*. 2007;20(3):922-31.
86. Yaghi OM, O'Keeffe M, Ockwig NW, Chae HK, Eddaoudi M, Kim J. Reticular synthesis and the design of new materials. *Nature*. 2003;423(6941):705.
87. Eddaoudi M, Moler DB, Li H, Chen B, Reineke TM, O'keeffe M, et al. *Modular chemistry: secondary building units as a basis for the design of highly*

porous and robust metal– organic carboxylate frameworks. *Accounts of chemical research*. 2001;34(4):319-30.

88. O’Keeffe M, Peskov MA, Ramsden SJ, Yaghi OM. The reticular chemistry structure resource (RCSR) database of, and symbols for, crystal nets. *Accounts of chemical research*. 2008;41(12):1782-9.
89. Rosi NL, Kim J, Eddaoudi M, Chen B, O’Keeffe M, Yaghi OM. Rod packings and metal– organic frameworks constructed from rod-shaped secondary building units. *Journal of the American Chemical Society*. 2005;127(5):1504-18.
90. Eddaoudi M, Kim J, Rosi N, Vodak D, Wachter J, O’Keeffe M, et al. Systematic design of pore size and functionality in isorecticular MOFs and their application in methane storage. *Science*. 2002;295(5554):469-72.
91. Institute EPR. Program on Technology Innovation: Post-combustion CO2 Capture Technology Development. 2008.
92. Millward AR, Yaghi OM. Metal– organic frameworks with exceptionally high capacity for storage of carbon dioxide at room temperature. *Journal of the American Chemical Society*. 2005;127(51):17998-9.
93. Xu X, Song C, Andresen JM, Miller BG, Scaroni AW. Preparation and characterization of novel CO2 “molecular basket” adsorbents based on polymer-modified mesoporous molecular sieve MCM-41. *Microporous and mesoporous materials*. 2003;62(1-2):29-45.
94. Xu X, Song C, Andresen JM, Miller BG, Scaroni AW. Novel polyethylenimine-modified mesoporous molecular sieve of MCM-41 type as high-capacity adsorbent for CO2 capture. *Energy & Fuels*. 2002;16(6):1463-9.
95. Chen Z, Chanda M. Gel-coated polymeric solid amine for sorption of carbon dioxide from humid air. *Journal of Polymer Materials*. 2002;19(4):381-7.
96. Satyapal S, Filburn T, Trela J, Strange J. Performance and properties of a solid amine sorbent for carbon dioxide removal in space life support applications. *Energy & Fuels*. 2001;15(2):250-5.
97. Leal O, Bolivar C, Sepulveda G, Molleja G, Martinez G, Esparragoza L. Carbon dioxide adsorbent and method for producing the adsorbent. Google Patents; 1992.
98. Leal O, Bolívar C, Ovalles C, García JJ, Espidel Y. Reversible adsorption of carbon dioxide on amine surface-bonded silica gel. *Inorganica Chimica Acta*. 1995;240(1-2):183-9.
99. Dibenedetto A, Aresta M, Fragale C, Narracci M. Reaction of silylalkylmono- and silylalkyldi- amines with carbon dioxide: evidence of formation of inter- and intra-molecular ammonium carbamates and their conversion into organic carbamates of industrial interest under carbon dioxide catalysis. *Green Chemistry*. 2002;4(5):439-43.
100. Diaf A, Garcia JL, Beckman EJ. Thermally reversible polymeric sorbents for acid gases: CO2, SO2, and NOx. *Journal of applied polymer science*. 1994;53(7):857-75.
101. Diaf A, Beckman EJ. Thermally reversible polymeric sorbents for acid gases. III. CO2-sorption enhancement in polymer-anchored amines. *Reactive and Functional Polymers*. 1995;27(1):45-51.
102. Kato M, Yoshikawa S, Nakagawa K. Carbon dioxide absorption by lithium orthosilicate in a wide range of temperature and carbon dioxide concentrations. *Journal of Materials Science Letters*. 2002;21(6):485-7.

103. Drage TC, Arenillas A, Smith KM, Pevida C, Piippo S, Snape CE. Preparation of carbon dioxide adsorbents from the chemical activation of urea-formaldehyde and melamine-formaldehyde resins. *Fuel*. 2007;86(1-2):22-31.
104. Pevida C, Plaza MG, Arias B, Feroso J, Rubiera F, Pis J. Surface modification of activated carbons for CO₂ capture. *Applied Surface Science*. 2008;254(22):7165-72.
105. Kato M, Nakagawa K, Essaki K, Maezawa Y, Takeda S, Kogo R, et al. Novel CO₂ absorbents using lithium-containing oxide. *International Journal of Applied Ceramic Technology*. 2005;2(6):467-75.
106. Brunetti A, Scura F, Barbieri G, Drioli E. Membrane technologies for CO₂ separation. *Journal of Membrane Science*. 2010;359(1-2):115-25.
107. Bounaceur R, Lape N, Roizard D, Vallieres C, Favre E. Membrane processes for post-combustion carbon dioxide capture: a parametric study. *Energy*. 2006;31(14):2556-70.
108. Powell CE, Qiao GG. Polymeric CO₂/N₂ gas separation membranes for the capture of carbon dioxide from power plant flue gases. *Journal of Membrane Science*. 2006;279(1-2):1-49.
109. McKee B. Solutions for 21st century, Zero emissions technologies for fossil fuels, Technology Status report. IEA Working Party on Fossil Fuels. 2002:1-47.
110. Gupta M, Coyle I, Thambimuthu K. Strawman document for CO₂ capture and storage technology roadmap. Canada: Canmet Energy Technology Centre. Natural Resources. 2003.
111. Bara JE, Hatakeyama ES, Gin DL, Noble RD. Improving CO₂ permeability in polymerized room-temperature ionic liquid gas separation membranes through the formation of a solid composite with a room-temperature ionic liquid. *Polymers for Advanced Technologies*. 2008;19(10):1415-20.
112. Car A, Stropnik C, Yave W, Peinemann K-V. PEG modified poly (amide-b-ethylene oxide) membranes for CO₂ separation. *Journal of Membrane Science*. 2008;307(1):88-95.
113. Dasgupta B, Sen SK, Banerjee S. Gas transport properties of fluorinated poly (ether imide) membranes containing indan moiety in the main chain. *Journal of Membrane Science*. 2009;345(1-2):249-56.
114. Choi S-H, Tasselli F, Jansen JC, Barbieri G, Drioli E. Effect of the preparation conditions on the formation of asymmetric poly (vinylidene fluoride) hollow fibre membranes with a dense skin. *European polymer journal*. 2010;46(8):1713-25.
115. Czyperek M, Zapp P, Bouwmeester HJ, Modigell M, Ebert K, Voigt I, et al. Gas separation membranes for zero-emission fossil power plants: MEM-BRAIN. *Journal of membrane science*. 2010;359(1-2):149-59.
116. Mondal MK, Balsora HK, Varshney P. Progress and trends in CO₂ capture/separation technologies: a review. *Energy*. 2012;46(1):431-41.
117. Lu J-G, Zheng Y-F, Cheng M-D. Membrane contactor for CO₂ absorption applying amino-acid salt solutions. *Desalination*. 2009;249(2):498-502.
118. Mansourizadeh A, Ismail A. Effect of LiCl concentration in the polymer dope on the structure and performance of hydrophobic PVDF hollow fiber membranes for CO₂ absorption. *Chemical Engineering Journal*. 2010;165(3):980-8.
119. Chabanon E, Roizard D, Favre E. Membrane contactors for postcombustion carbon dioxide capture: a comparative study of wetting resistance

- on long time scales. *Industrial & Engineering Chemistry Research*. 2011;50(13):8237-44.
120. Merino E, Ribagorda M. Control over molecular motion using the cis–trans photoisomerization of the azo group. *Beilstein journal of organic chemistry*. 2012;8(1):1071-90.
121. Crecca CR, Roitberg AE. Theoretical study of the isomerization mechanism of azobenzene and disubstituted azobenzene derivatives. *The Journal of Physical Chemistry A*. 2006;110(26):8188-203.
122. Tanchak OM, Barrett CJ. Light-induced reversible volume changes in thin films of azo polymers: the photomechanical effect. *Macromolecules*. 2005;38(25):10566-70.
123. Toshchevnikov V, Ilnytskyi J, Saphiannikova M. Photoisomerization kinetics and mechanical stress in azobenzene-containing materials. *The journal of physical chemistry letters*. 2017;8(5):1094-8.
124. Ikeda T, Tsutsumi O. Optical switching and image storage by means of azobenzene liquid-crystal films. *Science*. 1995;268(5219):1873-5.
125. Tamai N, Miyasaka H. Ultrafast dynamics of photochromic systems. *Chemical Reviews*. 2000;100(5):1875-90.
126. Ferri V, Elbing M, Pace G, Dickey MD, Zharnikov M, Samori P, et al. Light-powered electrical switch based on cargo-lifting azobenzene monolayers. *Angewandte Chemie International Edition*. 2008;47(18):3407-9.
127. Henzl J, Mehlhorn M, Gawronski H, Rieder KH, Morgenstern K. Reversible cis–trans isomerization of a single azobenzene molecule. *Angewandte Chemie International Edition*. 2006;45(4):603-6.
128. Kameda M, Sumaru K, Kanamori T, Shinbo T. Photoresponse gas permeability of azobenzene-functionalized glassy polymer films. *Journal of applied polymer science*. 2003;88(8):2068-72.
129. Bujak K, Nocoń K, Jankowski A, Wolińska-Grabczyk A, Schab-Balcerzak E, Janeczek H, et al. Azopolymers with imide structures as light-switchable membranes in controlled gas separation. *European Polymer Journal*. 2019.
130. Prasetya N, Donose BC, Ladewig BP. A new and highly robust light-responsive Azo-UiO-66 for highly selective and low energy post-combustion CO₂ capture and its application in a mixed matrix membrane for CO₂/N₂ separation. *Journal of Materials Chemistry A*. 2018;6(34):16390-402.
131. Prasetya N, Ladewig BP. New Azo-DMOF-1 MOF as a Photoresponsive Low-Energy CO₂ Adsorbent and Its Exceptional CO₂/N₂ Separation Performance in Mixed Matrix Membranes. *ACS applied materials & interfaces*. 2018;10(40):34291-301.
132. Anthony JL, Maginn EJ, Brennecke JF. Solubilities and Thermodynamic Properties of Gases in the Ionic Liquid 1-n-Butyl-3-methylimidazolium Hexafluorophosphate. *The Journal of Physical Chemistry B*. 2002;106(29):7315-20.
133. Henni A, East A, Raina R, deMontigny D, Tontiwachwuthikul P, Young S, et al. Quantum-Mechanical and Thermodynamic Study of Amines and Ionic Liquids for CO₂ Capture: Faculty of Graduate Studies and Research, University of Regina; 2013.
134. Zhang S, Sun N, He X, Lu X, Zhang X. Physical properties of ionic liquids: database and evaluation. *Journal of physical and chemical reference data*. 2006;35(4):1475-517.

135. Welton T. Room-temperature ionic liquids. Solvents for synthesis and catalysis. *Chemical reviews*. 1999;99(8):2071-84.
136. Blanchard LA, Hancu D, Beckman EJ, Brennecke JF. Green processing using ionic liquids and CO₂. *Nature*. 1999;399(6731):28.
137. Wasserscheid P, Welton T. *Ionic liquids in synthesis*: John Wiley & Sons; 2008.
138. Ghandi K. A review of ionic liquids, their limits and applications. *Green and sustainable chemistry*. 2014;4(01):44.
139. Rochelle GT. Amine scrubbing for CO₂ capture. *Science*. 2009;325(5948):1652-4.
140. Ramdin M, de Loos TW, Vlucht TJ. State-of-the-art of CO₂ capture with ionic liquids. *Industrial & Engineering Chemistry Research*. 2012;51(24):8149-77.
141. Shannon MS, Bara JE. Properties of alkylimidazoles as solvents for CO₂ capture and comparisons to imidazolium-based ionic liquids. *Industrial & Engineering Chemistry Research*. 2011;50(14):8665-77.
142. Zulfiqar S, Sarwar MI, Mecerreyes D. Polymeric ionic liquids for CO₂ capture and separation: potential, progress and challenges. *Polymer Chemistry*. 2015;6(36):6435-51.
143. Tang J, Sun W, Tang H, Radosz M, Shen Y. Enhanced CO₂ absorption of poly (ionic liquid) s. *Macromolecules*. 2005;38(6):2037-9.
144. Tang J, Shen Y, Radosz M, Sun W. Isothermal carbon dioxide sorption in poly (ionic liquid) s. *Industrial & Engineering Chemistry Research*. 2009;48(20):9113-8.
145. Bara JE, Lessmann S, Gabriel CJ, Hatakeyama ES, Noble RD, Gin DL. Synthesis and performance of polymerizable room-temperature ionic liquids as gas separation membranes. *Industrial & engineering chemistry research*. 2007;46(16):5397-404.
146. Tomé LC, Gouveia AS, Freire CS, Mecerreyes D, Marrucho IM. Polymeric ionic liquid-based membranes: Influence of polycation variation on gas transport and CO₂ selectivity properties. *Journal of membrane science*. 2015;486:40-8.
147. Green O, Grubjesic S, Lee S, Firestone MA. The design of polymeric ionic liquids for the preparation of functional materials. *Polymer Reviews*. 2009;49(4):339-60.
148. Lu J, Yan F, Texter J. Advanced applications of ionic liquids in polymer science. *Progress in Polymer Science*. 2009;34(5):431-48.
149. Yuan J, Antonietti M. Poly (ionic liquid) s: Polymers expanding classical property profiles. *Polymer*. 2011;52(7):1469-82.
150. Ye Y-S, Rick J, Hwang B-J. Ionic liquid polymer electrolytes. *Journal of Materials Chemistry A*. 2013;1(8):2719-43.
151. Mecerreyes D. Polymeric ionic liquids: Broadening the properties and applications of polyelectrolytes. *Progress in Polymer Science*. 2011;36(12):1629-48.
152. Yuan J, Mecerreyes D, Antonietti M. Poly (ionic liquid) s: An update. *Progress in Polymer Science*. 2013;38(7):1009-36.
153. Hayes R, Warr GG, Atkin R. Structure and nanostructure in ionic liquids. *Chemical reviews*. 2015;115(13):6357-426.

154. Cadena C, Anthony JL, Shah JK, Morrow TI, Brennecke JF, Maginn EJ. Why is CO₂ so soluble in imidazolium-based ionic liquids? *Journal of the American Chemical Society*. 2004;126(16):5300-8.
155. Aki SN, Mellein BR, Saurer EM, Brennecke JF. High-pressure phase behavior of carbon dioxide with imidazolium-based ionic liquids. *The Journal of Physical Chemistry B*. 2004;108(52):20355-65.
156. 岳振国, 刘晓敏, 赵玉灵, 张晓春, 吕兴梅, 张锁江. Molecular simulation on microstructure of ionic liquids in capture of CO₂. *过程工程学报*. 2011;11(4):652-9.
157. Xu G, Liang F, Yang Y, Hu Y, Zhang K, Liu W. An improved CO₂ separation and purification system based on cryogenic separation and distillation theory. *Energies*. 2014;7(5):3484-502.
158. Zhang X, Zhang X, Dong H, Zhao Z, Zhang S, Huang Y. Carbon capture with ionic liquids: overview and progress. *Energy & Environmental Science*. 2012;5(5):6668-81.
159. Mortazavi-Manesh S, Satyro MA, Marriott RA. Screening ionic liquids as candidates for separation of acid gases: solubility of hydrogen sulfide, methane, and ethane. *AIChE Journal*. 2013;59(8):2993-3005.
160. Scovazzo P, Kieft J, Finan DA, Koval C, DuBois D, Noble R. Gas separations using non-hexafluorophosphate [PF₆]⁻ anion supported ionic liquid membranes. *Journal of Membrane Science*. 2004;238(1-2):57-63.
161. Baltus RE, Counce RM, Culbertson BH, Luo H, DePaoli DW, Dai S, et al. Examination of the potential of ionic liquids for gas separations. *Separation science and technology*. 2005;40(1-3):525-41.
162. Moriya Y, Sasaki T, Yanase T. Gas collection method and apparatus therefor. Google Patents; 2010.
163. Park Y-I, Kim B-S, Byun Y-H, Lee S-H, Lee E-W, Lee J-M. Preparation of supported ionic liquid membranes (SILMs) for the removal of acidic gases from crude natural gas. *Desalination*. 2009;236(1-3):342-8.
164. Zhijun Z, Haifeng D, ZHANG X. The research progress of CO₂ capture with ionic liquids. *Chinese Journal of Chemical Engineering*. 2012;20(1):120-9.
165. Hanioka S, Maruyama T, Sotani T, Teramoto M, Matsuyama H, Nakashima K, et al. CO₂ separation facilitated by task-specific ionic liquids using a supported liquid membrane. *Journal of Membrane Science*. 2008;314(1-2):1-4.
166. Shishatskiy S, Pauls JR, Nunes SP, Peinemann K-V. Quaternary ammonium membrane materials for CO₂ separation. *Journal of Membrane Science*. 2010;359(1-2):44-53.
167. Scovazzo P, Havard D, McShea M, Mixon S, Morgan D. Long-term, continuous mixed-gas dry fed CO₂/CH₄ and CO₂/N₂ separation performance and selectivities for room temperature ionic liquid membranes. *Journal of Membrane Science*. 2009;327(1-2):41-8.
168. Tang J, Tang H, Sun W, Plancher H, Radosz M, Shen Y. Poly (ionic liquid) s: a new material with enhanced and fast CO₂ absorption. *Chemical Communications*. 2005(26):3325-7.
169. Hu X, Tang J, Blasig A, Shen Y, Radosz M. CO₂ permeability, diffusivity and solubility in polyethylene glycol-grafted polyionic membranes and their CO₂ selectivity relative to methane and nitrogen. *Journal of Membrane Science*. 2006;281(1-2):130-8.

170. Technologies ACFoAM, Terminology ACFoAMTSFo. Standard terminology for additive manufacturing technologies: ASTM International; 2012.
171. Wong KV, Hernandez A. A review of additive manufacturing. ISRN Mechanical Engineering. 2012;2012.
172. Noorani R. Rapid prototyping: principles and applications. 2006.
173. Kruth J-P. Material in-process manufacturing by rapid prototyping techniques. CIRP annals. 1991;40(2):603-14.
174. Cooper K. Rapid prototyping technology: selection and application: CRC press; 2001.
175. Morvan S, Hochsmann R, Sakamoto M. ProMetal RCT (TM) process for fabrication of complex sand molds and sand cores. Rapid Prototyping. 2005;11(2):1.
176. Pham D, Ji C. Design for stereolithography. Proceedings of the Institution of Mechanical Engineers, Part C: Journal of Mechanical Engineering Science. 2000;214(5):635-40.
177. Wohlers TT. Wohlers Report 2010: additive manufacturing state of the industry: annual worldwide progress report: Wohlers Associates; 2010.
178. Roppolo I, Chiappone A, Angelini A, Stassi S, Frascella F, Pirri C, et al. 3D printable light-responsive polymers. Materials Horizons. 2017;4(3):396-401.
179. Vaupotic B, Brezocnik M, Balic J. Use of PolyJet technology in manufacture of new product. Journal of Achievements in Materials and Manufacturing Engineering. 2006;18(1-2):319-22.
180. Halloran JW, Tomeckova V, Gentry S, Das S, Cilino P, Yuan D, et al. Photopolymerization of powder suspensions for shaping ceramics. Journal of the European Ceramic Society. 2011;31(14):2613-9.
181. Murr LE, Gaytan SM, Ramirez DA, Martinez E, Hernandez J, Amato KN, et al. Metal fabrication by additive manufacturing using laser and electron beam melting technologies. Journal of Materials Science & Technology. 2012;28(1):1-14.
182. Xiong Y. Investigation of the laser engineered net shaping process for nanostructured cermets: University of California, Davis; 2009.
183. Nguyen KT, West JL. Photopolymerizable hydrogels for tissue engineering applications. Biomaterials. 2002;23(22):4307-14.
184. Pereira RF, Bártolo PJ. Photopolymerizable hydrogels in regenerative medicine and drug delivery. Future Medicine; 2014.
185. Scranton AB, Bowman CN, Peiffer RW. Photopolymerization: fundamentals and applications: ACS Publications; 1997.
186. Decker C. UV-curing chemistry: past, present, and future. JCT, Journal of coatings technology. 1987;59(751):97-106.
187. Azagarsamy MA, Anseth KS. Bioorthogonal click chemistry: an indispensable tool to create multifaceted cell culture scaffolds. ACS Publications; 2012.
188. Lin CC, Ki CS, Shih H. Thiol-norbornene photoclick hydrogels for tissue engineering applications. Journal of applied polymer science. 2015;132(8).
189. Tibbitt MW, Kloxin AM, Sawicki LA, Anseth KS. Mechanical properties and degradation of chain and step-polymerized photodegradable hydrogels. Macromolecules. 2013;46(7):2785-92.
190. Pereira RF, Bártolo PJ. 3D photo-fabrication for tissue engineering and drug delivery. Engineering. 2015;1(1):090-112.

191. Fouassier J-P. Photoinitiation, photopolymerization, and photocuring: fundamentals and applications: Hanser; 1995.
192. West JL, Hubbell JA. Polymeric biomaterials with degradation sites for proteases involved in cell migration. *Macromolecules*. 1999;32(1):241-4.
193. Mann BK, Gobin AS, Tsai AT, Schmedlen RH, West JL. Smooth muscle cell growth in photopolymerized hydrogels with cell adhesive and proteolytically degradable domains: synthetic ECM analogs for tissue engineering. *Biomaterials*. 2001;22(22):3045-51.
194. Dumanian G, Dascombe W, Hong C, Labadie K, Garrett K, Sawhney A, et al. A new photopolymerizable blood vessel glue that seals human vessel anastomoses without augmenting thrombogenicity. *Plastic and reconstructive surgery*. 1995;95(5):901-7.
195. Bryant SJ, Nuttelman CR, Anseth KS. Cytocompatibility of UV and visible light photoinitiating systems on cultured NIH/3T3 fibroblasts in vitro. *Journal of Biomaterials Science, Polymer Edition*. 2000;11(5):439-57.
196. Jasveer S, Jianbin X. Comparison of different types of 3D printing technologies. *International Journal of Scientific and Research Publications (IJSRP)*. 2018;8(4):1-9.
197. Vitale A, Cabral J. Frontal conversion and uniformity in 3D printing by photopolymerisation. *Materials*. 2016;9(9):760.
198. Frascella F, González G, Bosch P, Angelini A, Chiappone A, Sangermano M, et al. Three-Dimensional Printed Photoluminescent Polymeric Waveguides. *ACS applied materials & interfaces*. 2018;10(45):39319-26.
199. Schultz AR, Lambert PM, Chartrain NA, Ruohoniemi DM, Zhang Z, Jangu C, et al. 3D printing phosphonium ionic liquid networks with mask projection microstereolithography. *ACS Macro Letters*. 2014;3(11):1205-9.
200. Lee J, Emon MOF, Vatani M, Choi J-W. Effect of degree of crosslinking and polymerization of 3D printable polymer/ionic liquid composites on performance of stretchable piezoresistive sensors. *Smart Materials and Structures*. 2017;26(3):035043.
201. Wales DJ, Cao Q, Kastner K, Karjalainen E, Newton GN, Sans V. 3D-Printable Photochromic Molecular Materials for Reversible Information Storage. *Advanced Materials*. 2018;30(26):1800159.
202. Shen L, Feng S, Li J, Chen J, Li F, Lin H, et al. Surface modification of polyvinylidene fluoride (PVDF) membrane via radiation grafting: novel mechanisms underlying the interesting enhanced membrane performance. *Scientific reports*. 2017;7(1):2721.
203. Fan X-X, Xie R, Zhao Q, Li X-Y, Ju X-J, Wang W, et al. Dual pH-responsive smart gating membranes. *Journal of Membrane Science*. 2018;555:20-9.
204. Liu N, Cao Y, Lin X, Chen Y, Feng L, Wei Y. A facile solvent-manipulated mesh for reversible oil/water separation. *ACS applied materials & interfaces*. 2014;6(15):12821-6.
205. Dong L, Fan W, Zhang H, Chen M, Zhao Y. CO₂-Responsive polymer membranes with gas-tunable pore size. *Chemical Communications*. 2017;53(69):9574-7.
206. Dybtsev DN, Chun H, Kim K. Rigid and flexible: a highly porous metal-organic framework with unusual guest-dependent dynamic behavior. *Angewandte Chemie International Edition*. 2004;43(38):5033-6.

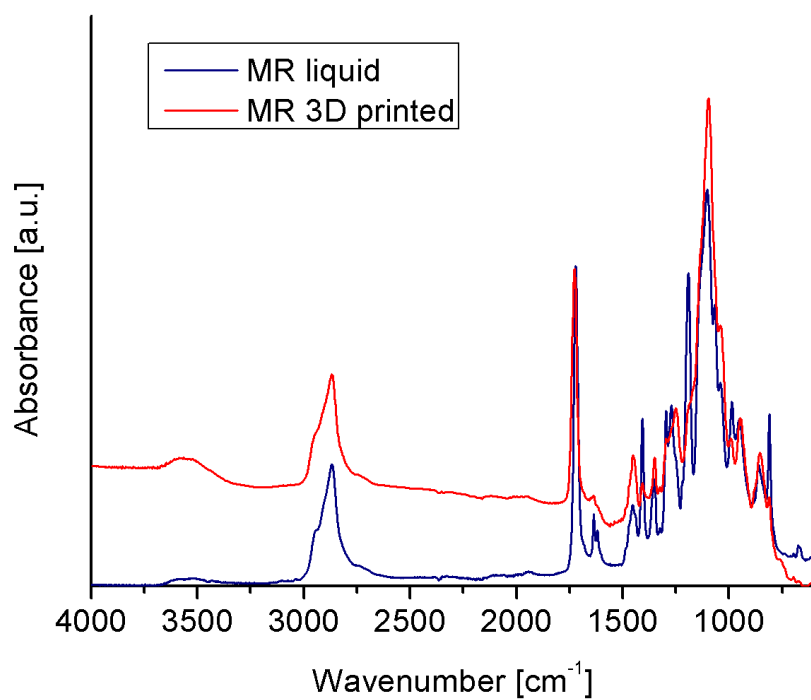
207. Wang X, Chi C, Zhang K, Qian Y, Gupta KM, Kang Z, et al. Reversed thermo-switchable molecular sieving membranes composed of two-dimensional metal-organic nanosheets for gas separation. *Nature communications*. 2017;8:14460.
208. Ma B, Ju X-J, Luo F, Liu Y-Q, Wang Y, Liu Z, et al. Facile fabrication of composite membranes with dual thermo-and pH-responsive characteristics. *ACS applied materials & interfaces*. 2017;9(16):14409-21.
209. Bolino L, Kundu T, Wang X, Wang Y, Hu Z, Koh K, et al. Breathing-induced new phase transition in an MIL-53 (Al)-NH₂ metal-organic framework under high methane pressures. *Chemical Communications*. 2017;53(58):8118-21.
210. Li H, Sadiq MM, Suzuki K, Doblin C, Lim S, Falcaro P, et al. MaLISA—a cooperative method to release adsorbed gases from metal-organic frameworks. *Journal of Materials Chemistry A*. 2016;4(48):18757-62.
211. Castellanos S, Kapteijn F, Gascon J. Photoswitchable metal organic frameworks: turn on the lights and close the windows. *CrystEngComm*. 2016;18(22):4006-12.
212. Cheng XQ, Wang ZX, Jiang X, Li T, Lau CH, Guo Z, et al. Towards sustainable ultrafast molecular-separation membranes: from conventional polymers to emerging materials. *Progress in Materials Science*. 2018;92:258-83.
213. Chang J, Zhang L, Wang P. Intelligent environmental nanomaterials. *Environmental Science: Nano*. 2018;5(4):811-36.
214. Baker RW, Low BT. Gas separation membrane materials: a perspective. *Macromolecules*. 2014;47(20):6999-7013.
215. Wandera D, Wickramasinghe SR, Husson SM. Stimuli-responsive membranes. *Journal of Membrane Science*. 2010;357(1-2):6-35.
216. Nicoletta FP, Cupelli D, Formoso P, De Filpo G, Colella V, Gugliuzza A. Light responsive polymer membranes: A review. *Membranes*. 2012;2(1):134-97.
217. Tomatsu I, Peng K, Kros A. Photoresponsive hydrogels for biomedical applications. *Advanced drug delivery reviews*. 2011;63(14-15):1257-66.
218. Akiba U, Minaki D, Anzai J-i. Photosensitive layer-by-layer assemblies containing azobenzene groups: Synthesis and biomedical applications. *Polymers*. 2017;9(11):553.
219. Kim S, Ogata T, Kurihara S. Azobenzene-containing polymers for photonic crystal materials. *Polymer Journal*. 2017;49(5):407.
220. Pirani F, Angelini A, Frascella F, Rizzo R, Ricciardi S, Descrovi E. Light-driven reversible shaping of individual azopolymeric micro-pillars. *Scientific reports*. 2016;6:31702.
221. Gillono M, Roppolo I, Frascella F, Scaltrito L, Pirri CF, Chiappone A. CO₂ permeability control in 3D printed light responsive structures. *Applied Materials Today*. 2019:100470.
222. Patel NP, Miller AC, Spontak RJ. Highly CO₂-permeable and-selective membranes derived from crosslinked poly (ethylene glycol) and its nanocomposites. *Advanced Functional Materials*. 2004;14(7):699-707.
223. Scordo G, Bertana V, Scaltrito L, Ferrero S, Cocuzza M, Marasso SL, et al. A novel highly electrically conductive composite resin for stereolithography. *Materials Today Communications*. 2019;19:12-7.
224. Ngo TD, Kashani A, Imbalzano G, Nguyen KT, Hui D. Additive manufacturing (3D printing): A review of materials, methods, applications and challenges. *Composites Part B: Engineering*. 2018;143:172-96.

225. Wang X, Jiang M, Zhou Z, Gou J, Hui D. 3D printing of polymer matrix composites: A review and prospective. *Composites Part B: Engineering*. 2017;110:442-58.
226. Fantino E, Chiappone A, Roppolo I, Manfredi D, Bongiovanni R, Pirri CF, et al. 3D printing of conductive complex structures with in situ generation of silver nanoparticles. *Advanced Materials*. 2016;28(19):3712-7.
227. Mishra M, Yagci Y. *Handbook of vinyl polymers: radical polymerization, process, and technology*: CRC press; 2016.
228. Priola A, Gozzelino G, Ferrero F, Malucelli G. Properties of polymeric films obtained from uv cured poly (ethylene glycol) diacrylates. *Polymer*. 1993;34(17):3653-7.
229. Liu SL, Shao L, Chua ML, Lau CH, Wang H, Quan S. Recent progress in the design of advanced PEO-containing membranes for CO₂ removal. *Progress in Polymer Science*. 2013;38(7):1089-120.
230. Costello L, Koros W. Thermally stable polyimide isomers for membrane-based gas separations at elevated temperatures. *Journal of Polymer Science Part B: Polymer Physics*. 1995;33(1):135-46.
231. Van der Vegt N. Temperature dependence of gas transport in polymer melts: molecular dynamics simulations of CO₂ in polyethylene. *Macromolecules*. 2000;33(8):3153-60.
232. Böhm N, Materny A, Kiefer W, Steins H, Müller M, Schottner G. Spectroscopic Investigation of the Thermal Cis– Trans Isomerization of Disperse Red 1 in Hybrid Polymers. *Macromolecules*. 1996;29(7):2599-604.
233. Buffeteau T, Lagugné Labarthe F, Pézolet M, Sourisseau C. Photoinduced orientation of azobenzene chromophores in amorphous polymers as studied by real-time visible and FTIR spectroscopies. *Macromolecules*. 1998;31(21):7312-20.
234. Kumar GS, Neckers D. Photochemistry of azobenzene-containing polymers. *Chemical Reviews*. 1989;89(8):1915-25.
235. Eisenbach CD. Effect of polymer matrix on the cis-trans isomerization of azobenzene residues in bulk polymers. *Die Makromolekulare Chemie: Macromolecular Chemistry and Physics*. 1978;179(10):2489-506.
236. Barrett CJ, Mamiya J-i, Yager KG, Ikeda T. Photo-mechanical effects in azobenzene-containing soft materials. *Soft Matter*. 2007;3(10):1249-61.
237. Norikane Y, Tamaoki N. Light-driven molecular hinge: a new molecular machine showing a light-intensity-dependent photoresponse that utilizes the trans– cis isomerization of azobenzene. *Organic letters*. 2004;6(15):2595-8.
238. Ismail AF, Khulbe KC, Matsuura T. *Gas Separation Membranes: Polymeric and Inorganic*: Springer International Publishing; 2015.
239. Patel NP, Miller AC, Spontak RJ. Highly CO₂-Permeable and Selective Polymer Nanocomposite Membranes. *Advanced Materials*. 2003;15(9):729-33.
240. Ghosal K, Freeman BD. Gas separation using polymer membranes: an overview. *Polymers for Advanced Technologies*. 1994;5(11):673-97.
241. Glasing J, Champagne P, Cunningham MF. *Current Opinion in Green and Sustainable Chemistry*. 2016.
242. Steldinger H, Esposito A, Brunnengräber K, Gläsel J, Etzold BJ. Activated Carbon in the Third Dimension—3D Printing of a Tuned Porous Carbon. *Advanced Science*. 2019.

243. Chiappone A, Fantino E, Roppolo I, Lorusso M, Manfredi D, Fino P, et al. 3D printed PEG-based hybrid nanocomposites obtained by sol–gel technique. *ACS applied materials & interfaces*. 2016;8(8):5627-33.
244. Gillono M, Chiappone A, Mendola L, Gomez Gomez M, Scaltrito L, Pirri CF, et al. Study on the Printability through Digital Light Processing Technique of Ionic Liquids for CO₂ Capture. *Polymers*. 2019;11(12):1932.
245. Nulwala H, Mirjafari A, Zhou X. Ionic liquids and poly (ionic liquid) s for 3D printing—A focused mini-review. *European Polymer Journal*. 2018;108:390-8.
246. Chen J-S, Ober CK, Poliks MD, Zhang Y, Wiesner U, Cohen C. Controlled degradation of epoxy networks: analysis of crosslink density and glass transition temperature changes in thermally reworkable thermosets. *Polymer*. 2004;45(6):1939-50.
247. Jakubiak J, Allonas X, Fouassier J, Sionkowska A, Andrzejewska E, Linden L, et al. Camphorquinone–amines photoinitiating systems for the initiation of free radical polymerization. *Polymer*. 2003;44(18):5219-26.
248. Fumino K, Wulf A, Ludwig R. Strong, localized, and directional hydrogen bonds fluidize ionic liquids. *Angewandte Chemie International Edition*. 2008;47(45):8731-4.
249. Berthod A, Ruiz-Angel M, Carda-Broch S. Ionic liquids in separation techniques. *Journal of Chromatography A*. 2008;1184(1-2):6-18.
250. Blanchard LA, Gu Z, Brennecke JF. High-Pressure Phase Behavior of Ionic Liquid/CO₂ Systems. *The Journal of Physical Chemistry B*. 2001;105(12):2437-44.
251. Pérez-Salado Kamps Á, Tuma D, Xia J, Maurer G. Solubility of CO₂ in the Ionic Liquid [bmim][PF₆]. *Journal of Chemical & Engineering Data*. 2003;48(3):746-9.
252. Husson-Borg P, Majer V, Costa Gomes MF. Solubilities of Oxygen and Carbon Dioxide in Butyl Methyl Imidazolium Tetrafluoroborate as a Function of Temperature and at Pressures Close to Atmospheric Pressure. *Journal of Chemical & Engineering Data*. 2003;48(3):480-5.
253. Mejía I, Stanley K, Canales R, Brennecke JF. On the high-pressure solubilities of carbon dioxide in several ionic liquids. *Journal of Chemical & Engineering Data*. 2013;58(9):2642-53.
254. Corvo MC, Sardinha J, Casimiro T, Marin G, Seferin M, Einloft S, et al. A rational approach to CO₂ capture by imidazolium ionic liquids: Tuning CO₂ solubility by cation alkyl branching. *ChemSusChem*. 2015;8(11):1935-46.
255. Anderson JL, Dixon JK, Brennecke JF. Solubility of CO₂, CH₄, C₂H₆, C₂H₄, O₂, and N₂ in 1-Hexyl-3-methylpyridinium Bis (trifluoromethylsulfonyl) imide: Comparison to Other Ionic Liquids. *Accounts of chemical research*. 2007;40(11):1208-16.
256. Pringle JM, Golding J, Baranyai K, Forsyth CM, Deacon GB, Scott JL, et al. The effect of anion fluorination in ionic liquids—physical properties of a range of bis (methanesulfonyl) amide salts. *New journal of chemistry*. 2003;27(10):1504-10.
257. Hu Y-F, Liu Z-C, Xu C-M, Zhang X-M. The molecular characteristics dominating the solubility of gases in ionic liquids. *Chemical Society Reviews*. 2011;40(7):3802-23.
258. Shiflett MB, Yokozeki A. Phase behavior of carbon dioxide in ionic liquids:[emim][acetate],[emim][trifluoroacetate], and

- [emim][acetate]+[emim][trifluoroacetate] mixtures. *Journal of Chemical & Engineering Data*. 2008;54(1):108-14.
259. Täuber K, Zhao Q, Antonietti M, Yuan J. Tuning the pore size in gradient poly (ionic liquid) membranes by small organic acids. *ACS Macro Letters*. 2014;4(1):39-42.
260. Budd PM, McKeown NB. Highly permeable polymers for gas separation membranes. *Polymer Chemistry*. 2010;1(1):63-8.
261. Rekowska N, Arbeiter D, Konasch J, Riess A, Mau R, Eickner T, et al. Thermomechanical properties of PEGDA and its co-polymers. *Current Directions in Biomedical Engineering*. 2018;4(1):669-72.
262. Tang H, Tang J, Ding S, Radosz M, Shen Y. Atom transfer radical polymerization of styrenic ionic liquid monomers and carbon dioxide absorption of the polymerized ionic liquids. *Journal of Polymer Science Part A: Polymer Chemistry*. 2005;43(7):1432-43.
263. Tang J, Tang H, Sun W, Radosz M, Shen Y. Poly (ionic liquid) s as new materials for CO₂ absorption. *Journal of Polymer Science Part A: Polymer Chemistry*. 2005;43(22):5477-89.

Appendix A



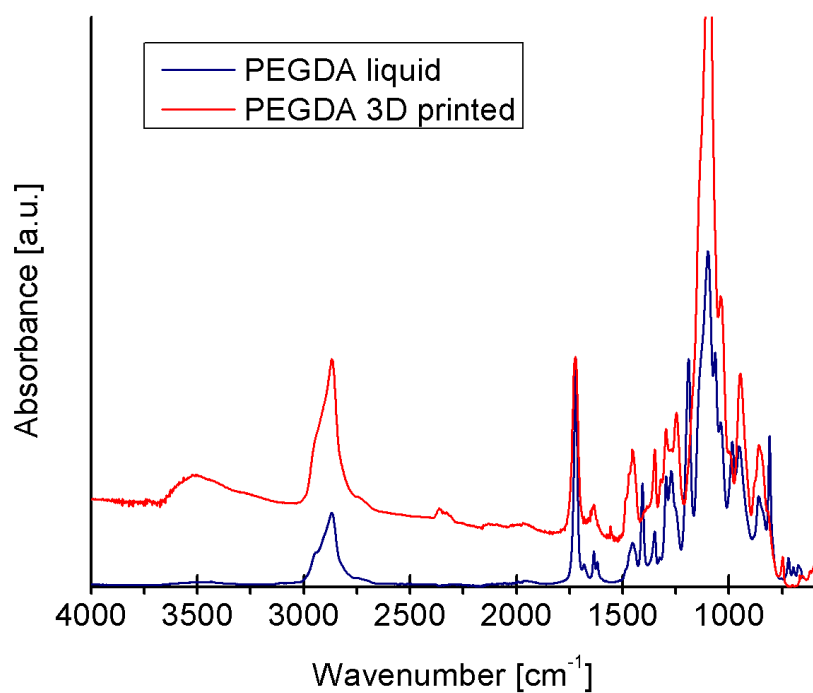
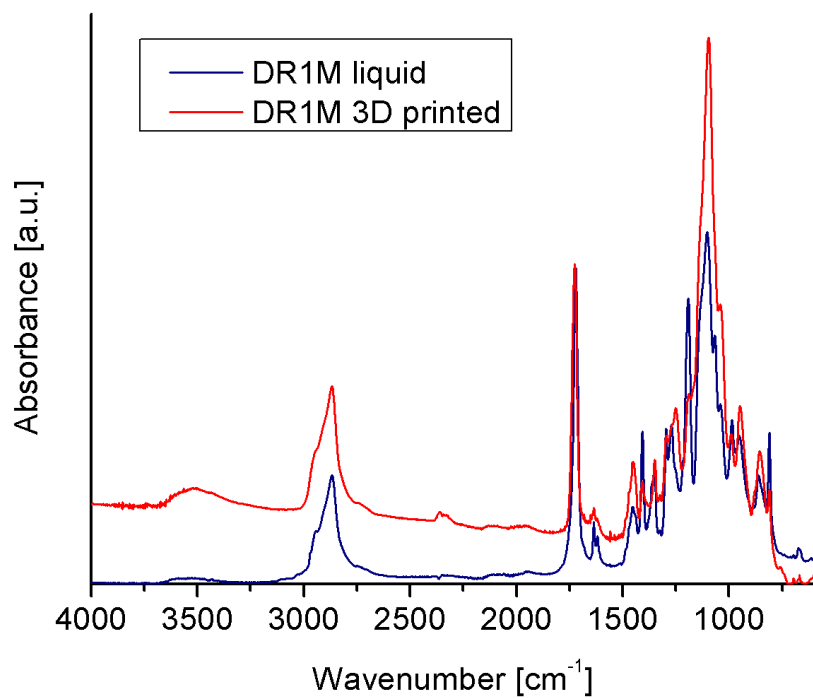


Figure A1 FTIR spectra from 600 cm⁻¹ to 4000 cm⁻¹ of samples containing PEGDA/MR, PEGDA/DR1M and neat PEGDA before and after the 3D printing process.

Appendix B

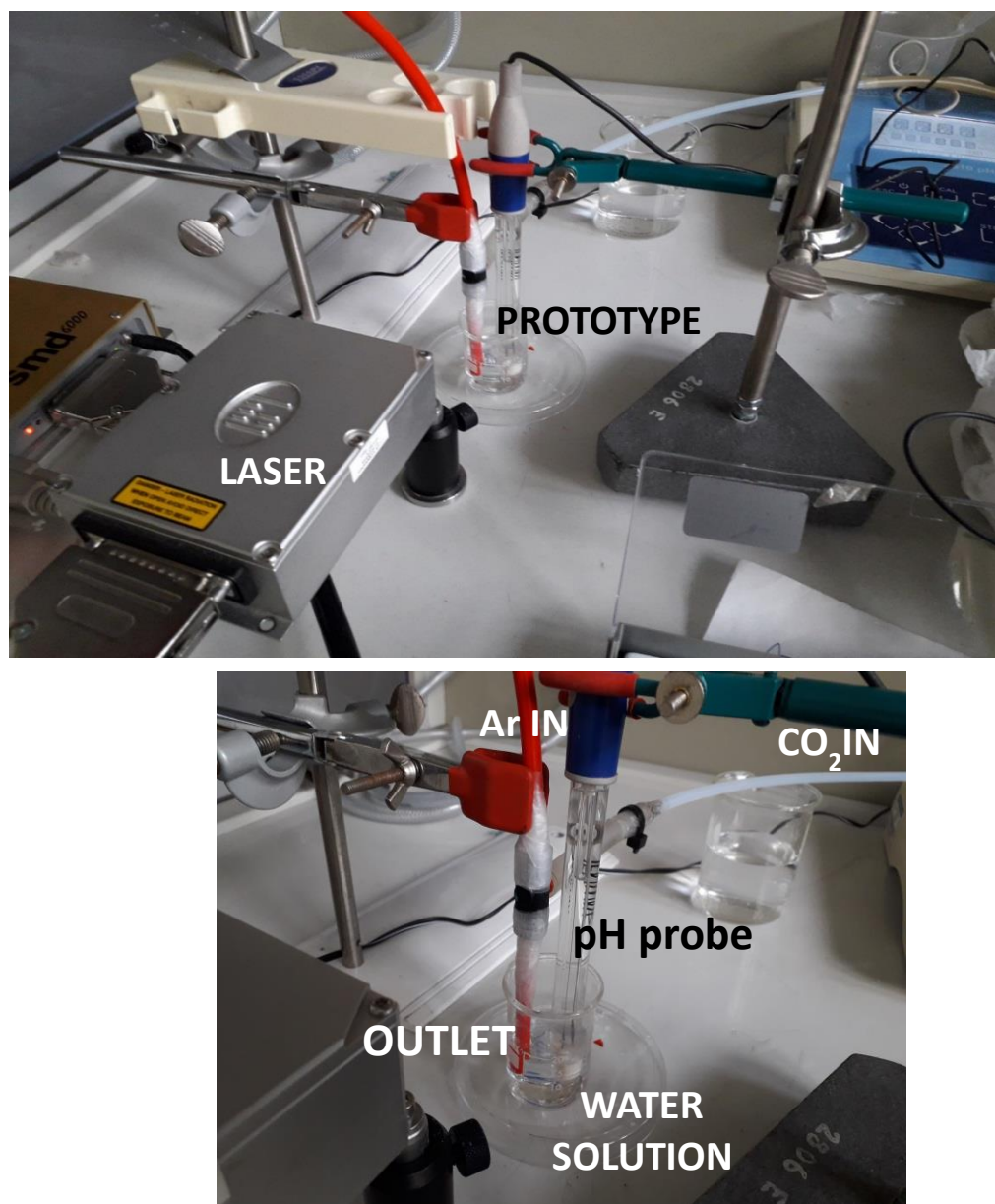
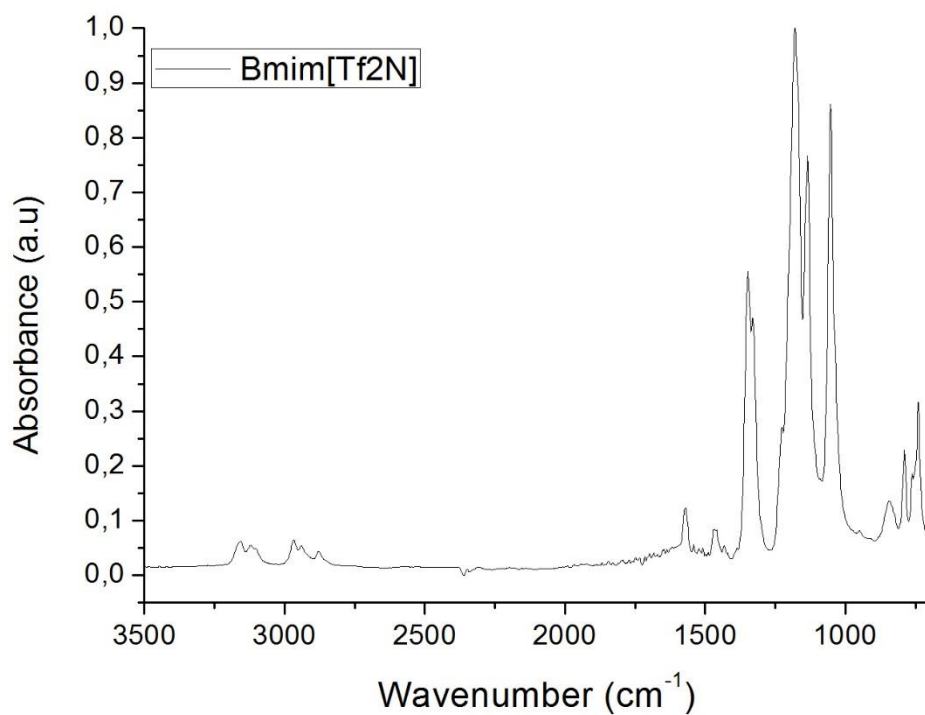
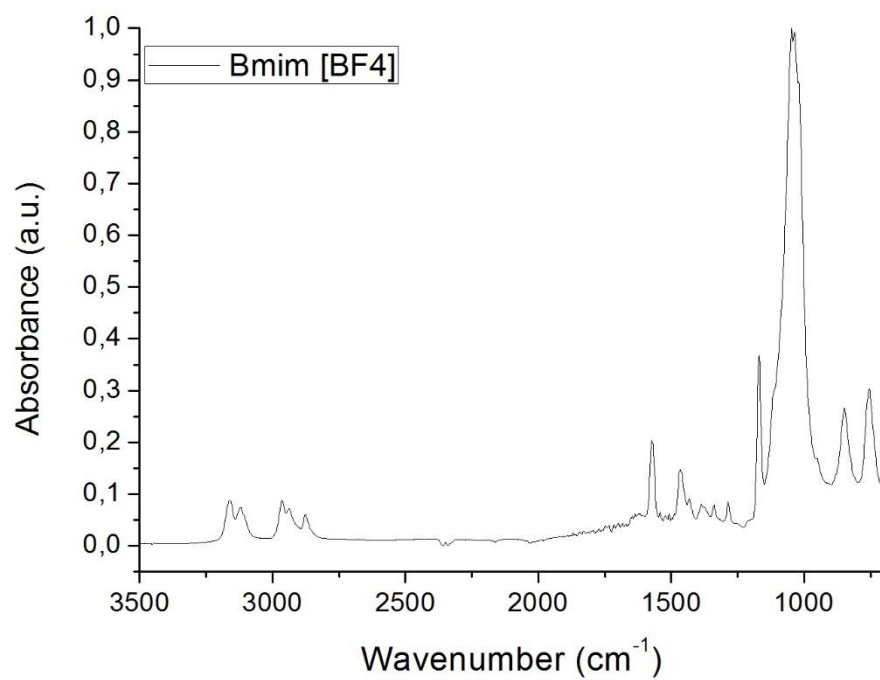
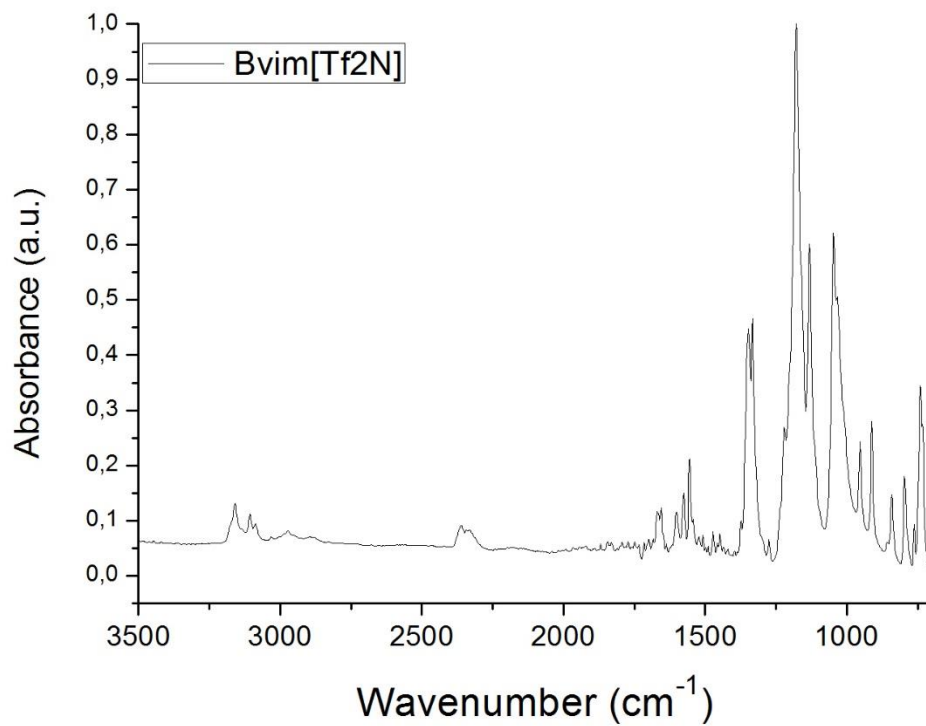
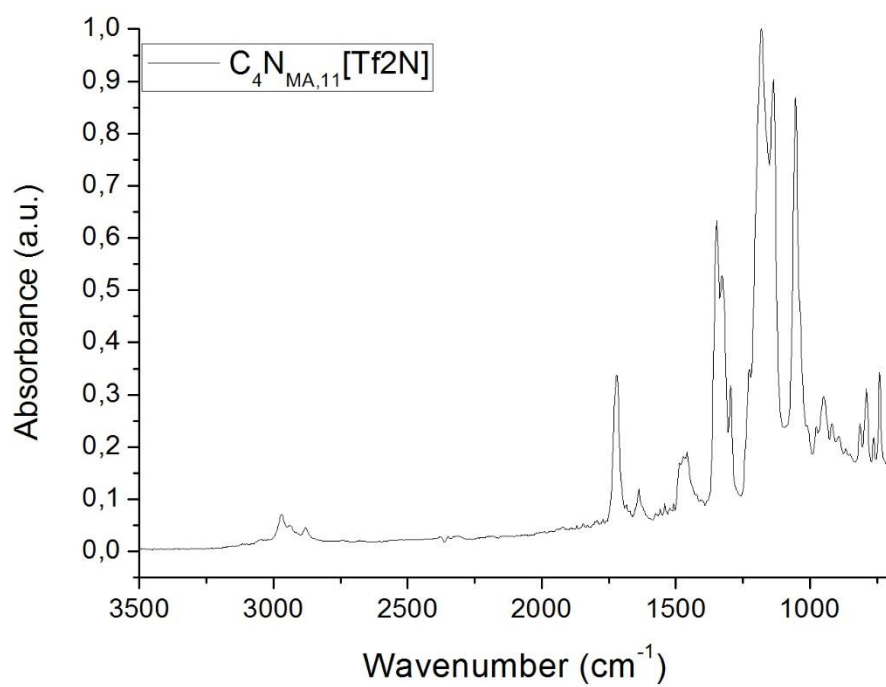


Figure B1 Experimental setup of the dynamic light-controlled CO₂ permeability related to pH variation.

Appendix C





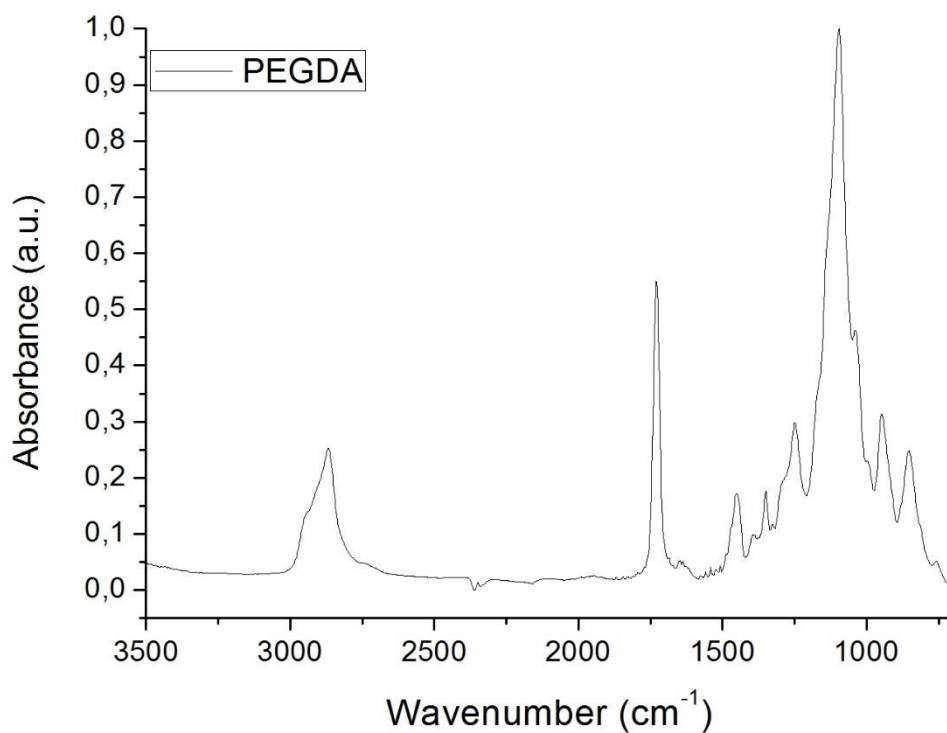
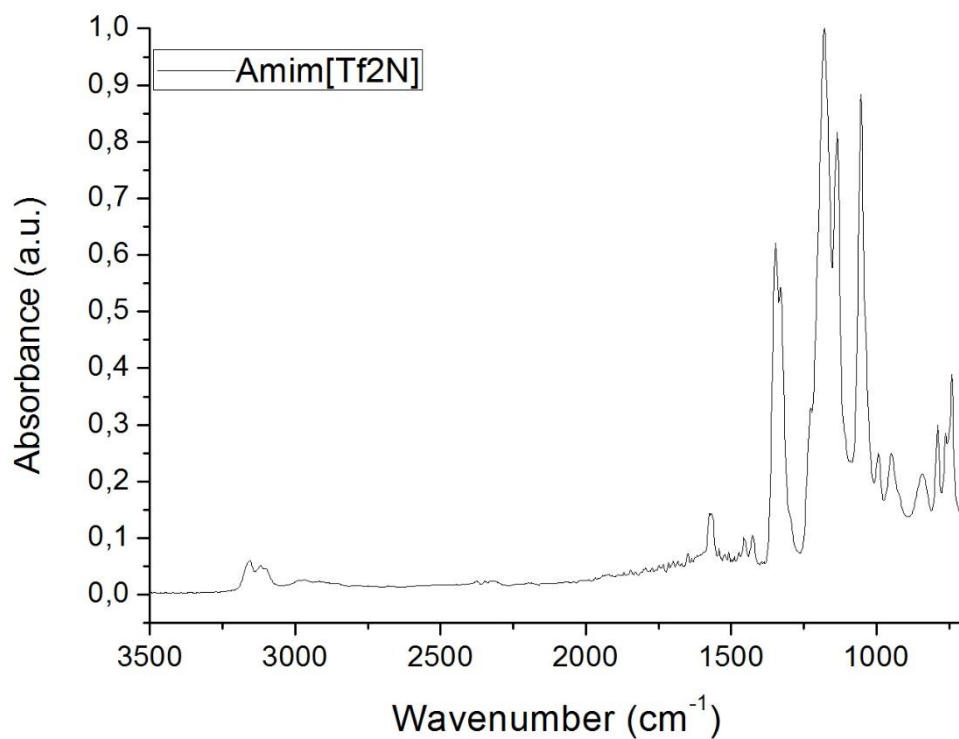
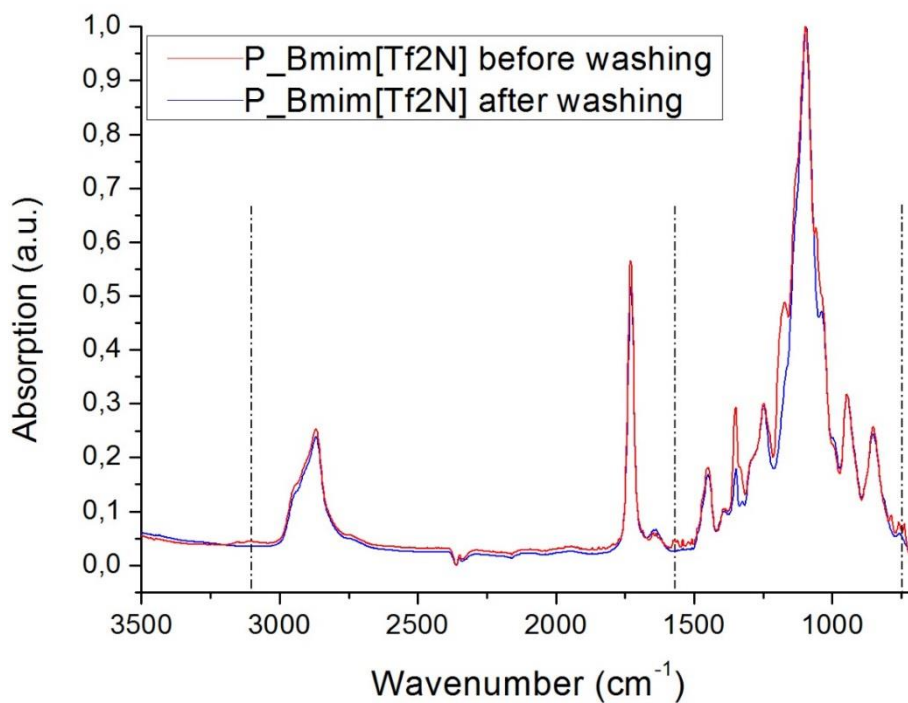
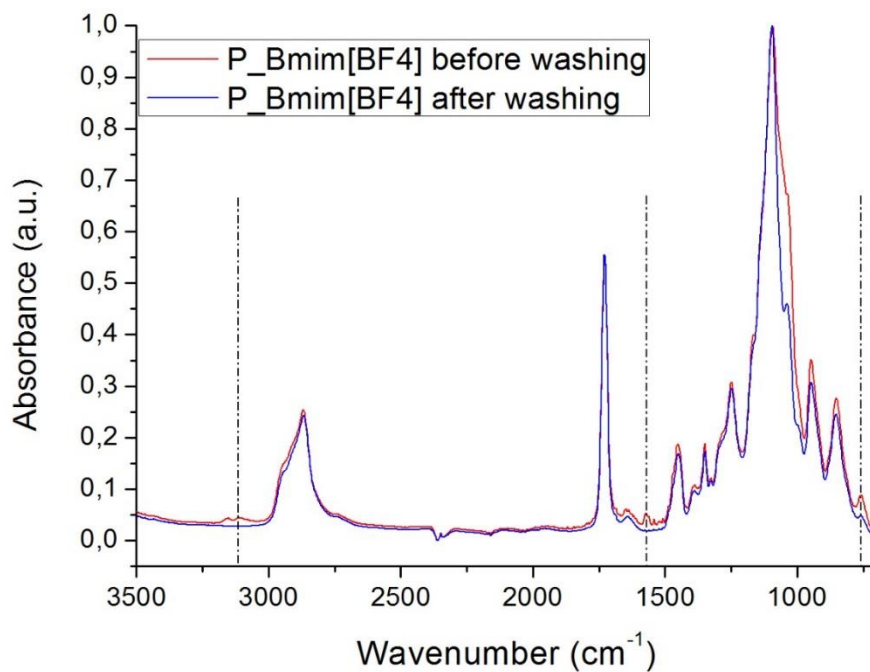
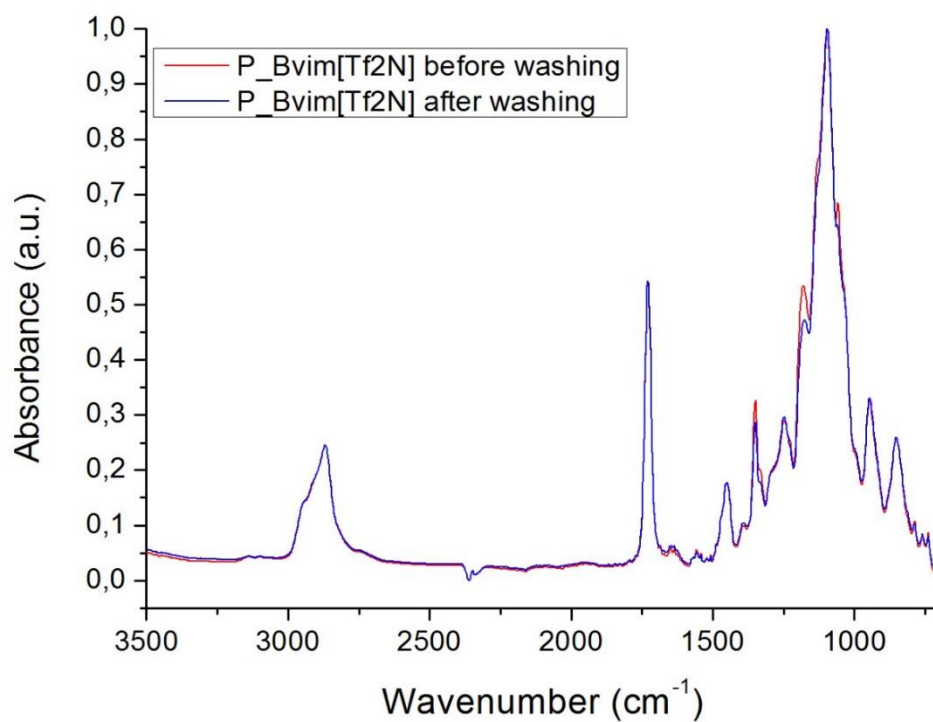
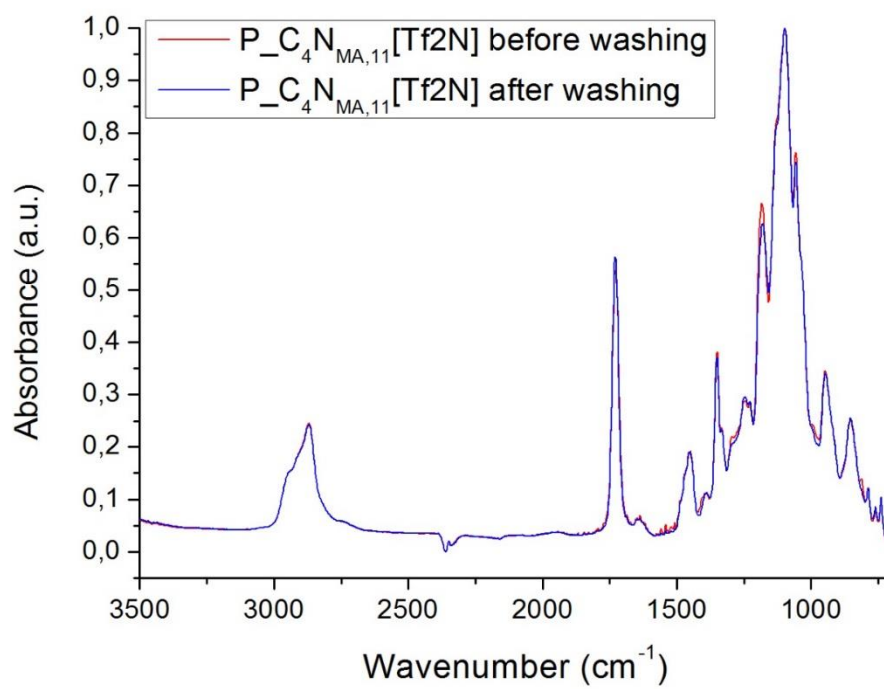


Figure C1 FTIR-ATR spectra of neat ILs and neat PEGDA.

Appendix D





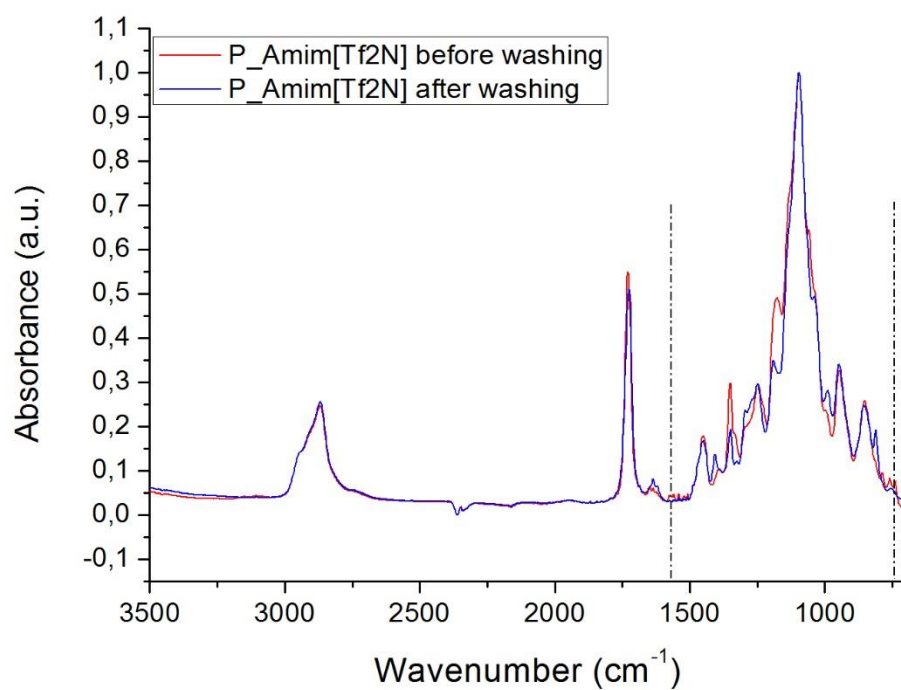
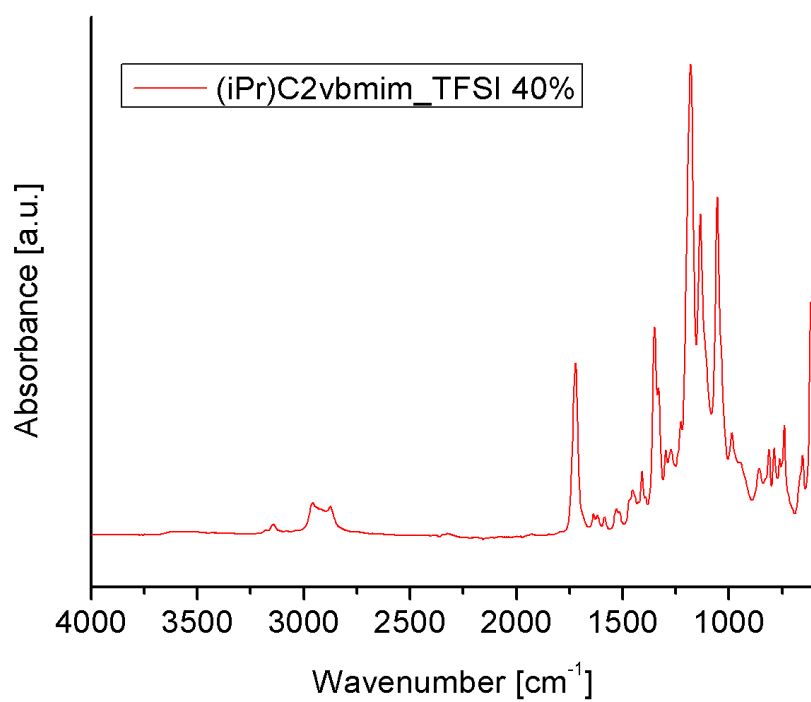
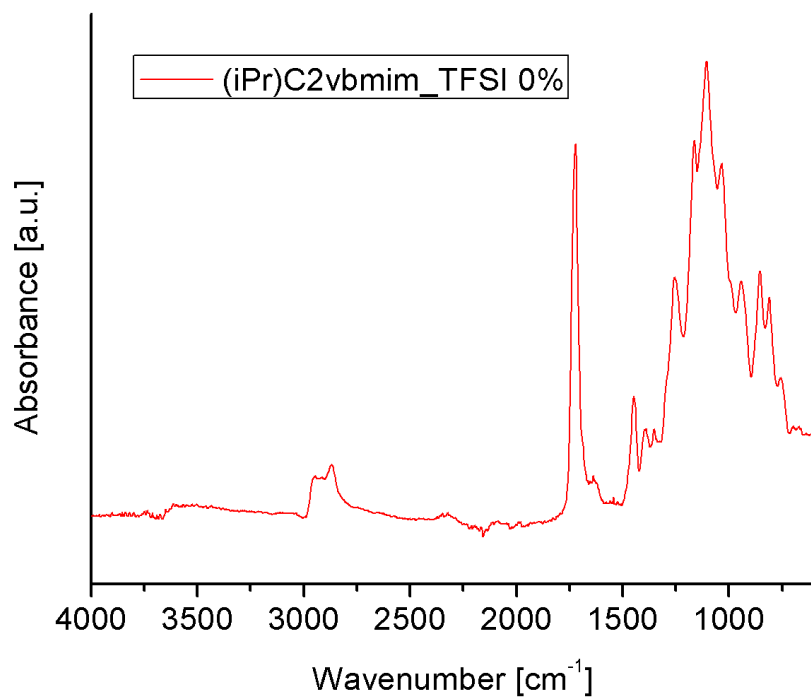
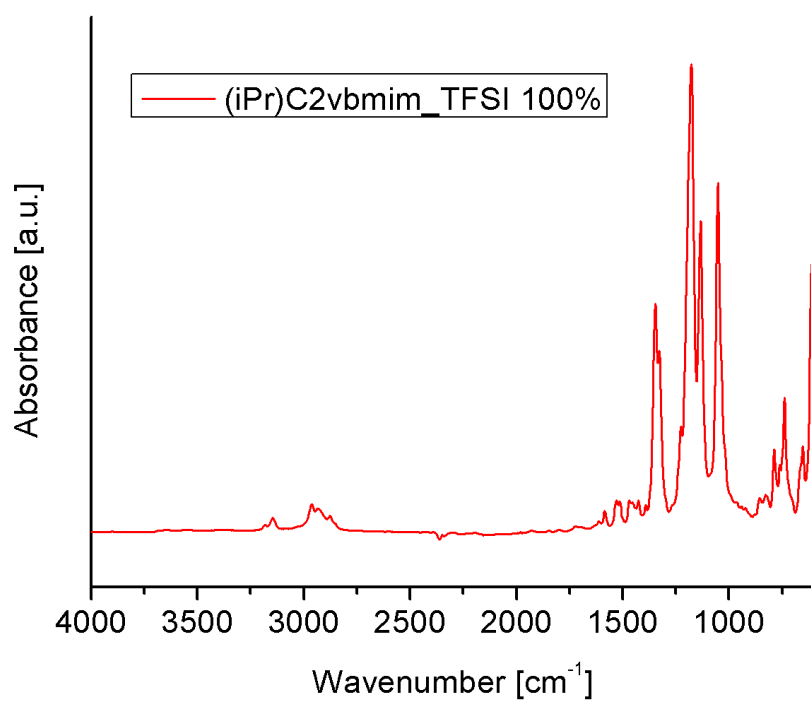
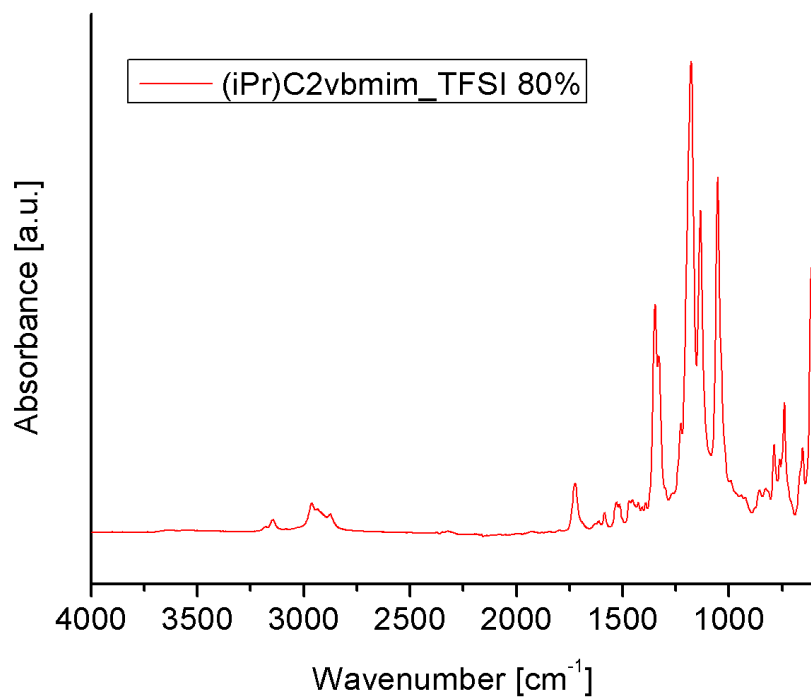


Figure D1 FTIR-ATR spectra of polymerized formulations before (red) and after (blue) solvent washing. The dashed bars indicate where the peaks of the ILs disappears after solvent washing.

Appendix E





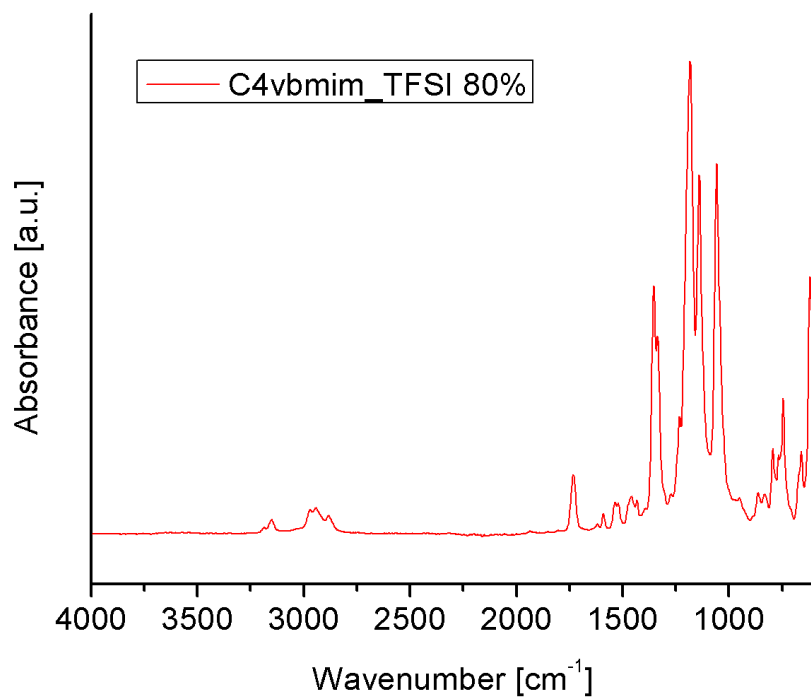


Figure E1 FTIR spectra from 600 cm⁻¹ to 4000 cm⁻¹ of samples containing mixtures of PEGDA and (iPr)C2vbmim_TFSI in ratios of 100/0, 60/40, 20/80 and 0/100 mol% respectively. The last graph shows the spectrum of the sample containing PEGDA and C4vbmim_TFSI 20/80 mol%.

Appendix F

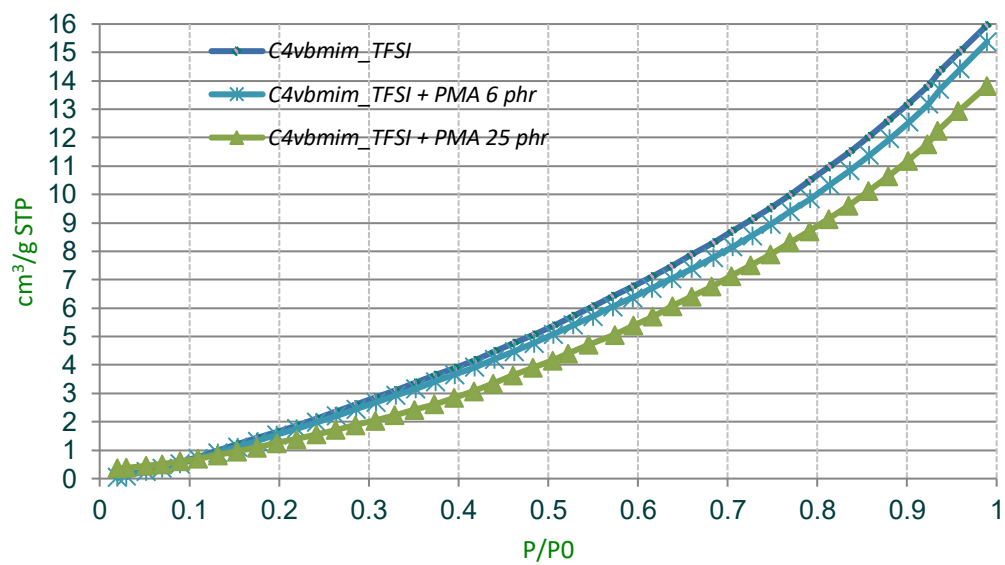


Figure F1. Nitrogen absorption isotherms of membranes containing C4vbmim_TFSI + 0 %wt, 6 %wt and 25 %wt of PMA.

Appendix G

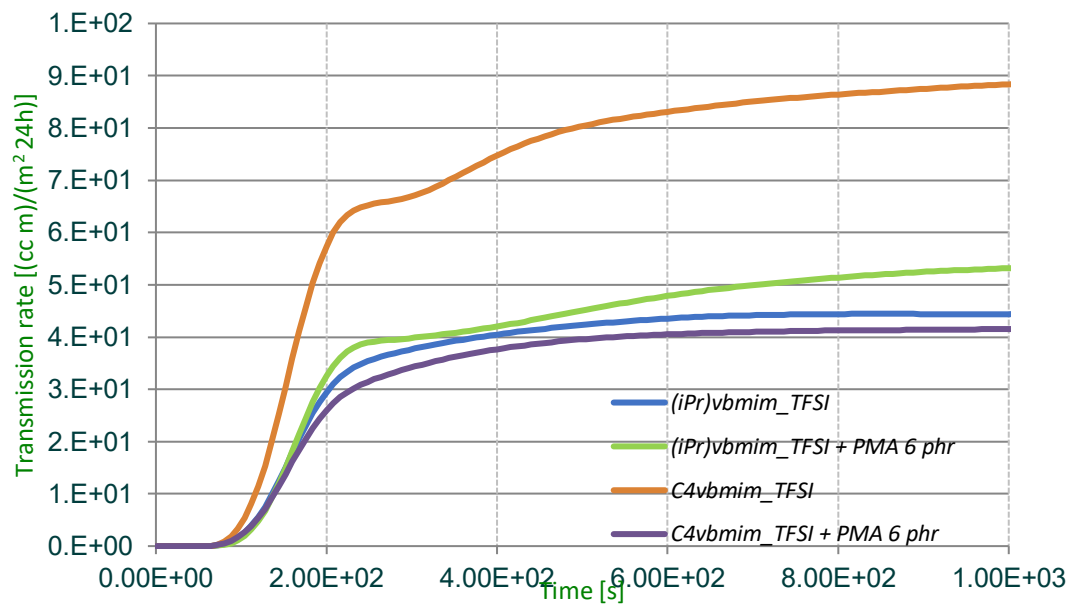


Figure G1. CO₂ transmission rate curves for membranes containing (iPr)C2vbmim_TFSI and C4vbmim_TFSI + 6 %wt of PMA.